# CONTENTS

## SCIENTIFIC AND TECHNICAL

## INDUSTRIAL

# DEVELOPMENT OF TECHNOLOGY AND EQUIPMENT FOR PRESS WELDING OF TUBULAR PARTS UNDER THE CONDITIONS OF PRODUCTION FOR THE PURPOSE OF SAVING RESOURCES AND INCREASE IN THE REALIABILITY OF HIGH-LOADED PRODUCTS

**S.I. Kuchuk-Yatsenko, V.S. Kachynskyi** and **M.P. Koval**

E.O. Paton Electric Welding Institute of the NAS of Ukraine
11 Kazymyr Malevych Str., 03150, Kyiv, Ukraine. E-mail: office@paton.kiev.ua

Replacement of outdated technologies in the production of tubular parts is an urgent task. The paper presents the materials of carried out investigations on press welding of high-loaded steel tubular parts with a diameter of up to 120 mm and wall thickness of up to 6 mm, development of control system, metallographic and mechanical examinations on determination of the properties of welded joints. The main technological advantages of press welding of high-loaded products are shown. 7 Ref., 3 Tables, 6 Figures.

Recently, the volumes of works on manufacture of brass parts with a diameter from 40 to 120 mm at the enterprises of the industry of Ukraine have considerably increased. To solve the problems before the industry of Ukraine, it is proposed to replace outdated existing technologies of works on application of expensive brass and precision presses of 350 t used in the production of tubular parts, with the new technology using welded steel tubular billets. This will significantly save resources by replacing brass, which has a much higher cost, with cheaper steel billets, increase the efficiency and improve working conditions, reduce electric power consumption and shorten production costs.

The welding method is used in industry mainly for joining parts of a tubular cross-section with a wall thickness of up to 4 mm and a diameter of up to 100 mm, which are used in the automotive industry. In this case shielding gases are used [1–4] and also PMIAB process without the use of shielding gas is possible [5, 6].

At the beginning of the investigations, the problems of testing the design and technology of manufacturing welded steel tubular parts were solved, which require solving the whole range of issues regarding the operation of high-loaded tubular parts. Theoretical and experimental investigations were carried out,

directed on solving basic questions of manufacturing welded steel parts. The technology was developed, which provides mass production of steel tubular parts at factories of the branch.

As the basis of the technological system an industrial computer began to be used, operating under the OS WINDOWS10 and the specially developed software. The software was developed taking into account the gained experience and the latest achievements in the field of computer technology regarding the accumulation and processing of information. In the construction of the control system and registration of welding parameters, generally available elements and devices were used, which greatly simplifies the adjustment of technological parameters of the system and welding process control.

The system for control of the welding machine for PMIAB process is based on the processes of scanning the system sensors, processing of the received data and generating data files and a derived file of the daily report, in which the following parameters are fixed:

● welding time by heating stages T1, T2 T3, T4, T5, T6;

● current of welding arc by heating stages I2, I3, I4, I5;

● voltage of welding arc at the three stages of heating parts U2, U3, U4 (U1 is the voltage of the

S.I. Kuchuk-Yatsenko — https://orcid.ord/0000-0002-1166-0253, V.S. Kachynskyi — https://orcid.ord/0000-0001-9695-6434,
M.P. Koval — https://orcid.ord/0000-0003-2066-3365

excitation stage and the beginning of constant arc movement (arc acceleration) under the action of the magnetic field at the edges of parts is not taken into account, because before the constant movement, the arc takes values from short-circuit to open-circuit mode of the welding arc power source);

● total amount of energy spent on heating parts $E_a$;

● upsetting rate $V_{ups}$ (hereinafter referred to as the initial speed of coming of the moving part of the welding machine with the stationary part together, i.e. it was experimentally established that this is the average speed of counter-movement per 1.5 mm of arc gap before the contact of welded parts);

● upsetting area $S_{ups}$ (value of total deformation of the parts);

● upsetting pressure $P_{ups}$ (maximum value of pressure drop in the hydraulic system of the welding machine during realization of upsetting);

The deviation of these parameters beyond the tolerances depends on many reasons. Therefore, it is necessary to develop the algorithms of:

● control of the two-level system, which provide correcting the welding mode in order to stabilize the process and, accordingly, the required weld butt quality;

● weld butt quality evaluation;

● evaluation of the technical condition of welding machines and conditions of their operation;

● formation of recommendations with correcting the parameters of the technological process.

The existing quality testing, during which the obtained data are compared with the reference ones, is a logical function: the quality indices are in the tolerance while simultaneously all the controlled parameters are in the tolerance. At such testing, the following indices are not considered:

● significance of the impact of each of the parameters on the quality index;

● uncertainty of the limit of tolerances of the process parameters for different products;

● possible increase in the influence of totality of a certain combination of deviations on welding quality.

An algorithm for welding quality testing was developed based on the analysis of process parameters at three stages of its realization.

1. Heating of tubular parts. Period of temperature field formation at the ends of welded parts.

2. Forcing. Stage of providing shielding environment in the arc gap.

3. Upsetting. Formation of joint in the solid phase.

The conclusion about the quality of a produced welded joint with a certain degree of probability is made on the basis of logical rules, compiled based on the results of investigations of technological features of the PMIAB process.

To control the welding process, the following parameters are used:

● welding time by the stages (T1–T6); current value at the stages of heating (12–15);

● voltage values at the stages of arc existence (U2–U4); upsetting rates and values ($V_{ups}$ and $L_{ups}$); pressure in the hydraulic system during upsetting $P_{ups}$; energy spent on heating parts $E_a$.

The development of the scheme of control of the machine K-872 for PMIAB welding was performed by replacing outdated equipment and upgrading and improving the software of the control module. To provide realization of the quality control algorithm, the control cabinet was modernized and the control system executive devices were partially replaced. A modern PC was applied, adapted for using in the industrial conditions.

The registration of the welding process parameters in the upgraded machine K-872 took place according to the scheme shown in Figure 1.

The correspondence of the computer evaluation of quality testing with the real state of affairs is the provision of the abovementioned system with real initial data. In the case of PMIAB, such data are current and voltage of the welding arc, mutual arrangement of the welded pipes and pressure in the hydraulic system during upsetting.

Obtaining data from the sensors of the registration system is as follows. The input of the normalizing in-
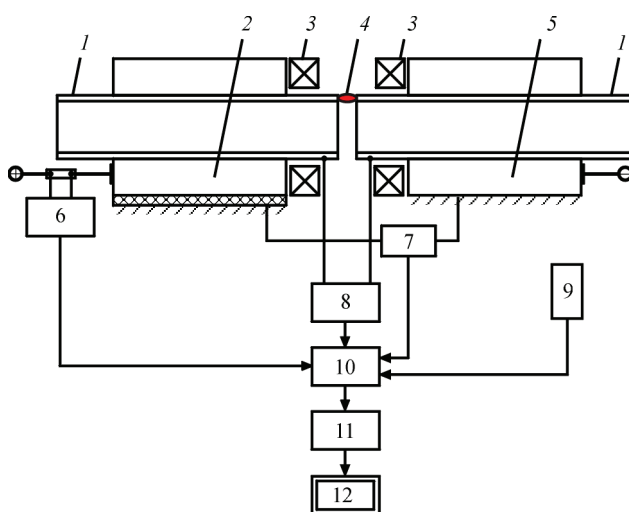


**Figure 1.** Block diagram of the model of quality testing of welded joints: *1* — welded pipes; *2* — moving clamping device; *3* — elements of magnetic system; *4* — electric arc column, moving along the edges of welded pipes; *5* — fixed clamping device; *6* — current sensor with instrumental signal amplifier; *7* — sensor for position of moving part of the welding machine; *8* — sensor for voltage drop on the welding arc; *9* — sensor of measurement of absolute pressure of hydraulic system built in a rod cavity of the cylinder, upsetting of welding machine; *10* — normalizing instrumental amplifier (with low pass filter $F_{cut-off}$ = 100 Hz); *11* — receiving analogue-to-digital converter (ADC), *12* — personal computer

**Table 1.** Chemical composition of welded steels, wt.%

| Steel | C | Si | Mn | P | S | Cu | Ni | Cr | Mo | Al |
|-------|------|------|------|-------|-------|------|------|------|------|------|
| 20 | 0.19 | 0.30 | 0.50 | 0.005 | 0.004 | 0.16 | 0.12 | 0.08 | 0.05 | 0.01 |
| 35 | 0.39 | 0.32 | 0.68 | 0.004 | 0.024 | 0.08 | 0.03 | 0.04 | 0.05 | 0.01 |

**Table 2.** Results of carried out tests on tear and impact toughness of base metal of pipe and welded joint

| Steels | Size of pipes, mm | $\sigma_t$, MPa | | $KCV$, +20 °C, J/cm$^2$ | |
|--------|-------------------|-------------|--------------|------------|--------------|
| | | Base metal | Welded joint | Base metal | Welded joint |
| 20 + 35 | 102×6.0 | $\frac{508–525}{516.5}$ | $\frac{510–524}{517.5}$ | $\frac{67–84}{75–5}$ | $\frac{78–81}{79–5}$ |
| 20 + 35 | 42×3.5 | $\frac{508–525}{516.5}$ | $\frac{516–527}{522.5}$ | $\frac{67–84}{75.5}$ | $\frac{88–85}{86}$ |

put amplifier 8 is connected directly to the terminals, which are located on the clamping devices. In the amplifier, the voltage drop of the welding arc, which occurs at the beginning of the process and is in the range of 20–30 V of direct current, is normalized to the output voltage of 2–3 V. For the further processing and analysis, the derived signal of welding voltage drop from the output of the amplifier *8* is sent to the input of the analogue-to-digital converter (ADC). During the start of the software operation, ADC is set up in such a way that the sampling frequency of the analogue inputs is 10 sampling points per one reading of the data from the ADC output. A more accurate data transfer to the control program is achieved.

The software of the control complex was finalized by changing the functional parameters of the existing software modules. This allowed expanding the time and parametric limits of operation of the executive devices when performing the adjustment of the parameters of the PMIAB process. The software performs the database formation, which, in turn, allows analyzing the data obtained during welding for the entire operation of the

equipment, which greatly simplifies the search for optimal parameters of the welding mode [7].

The course of the heating process during welding is influenced by different factors, which makes it necessary to test the quality of welded joints. The process of joints formation is influenced by the following factors:

• condition of end surfaces (surface temperature, presence of microroughnesses, oxide films and other contamination);

• temperature distribution at the ends of parts;

• value and nature of plastic deformation of the ends during upsetting.

The experimental welds were produced, research and industrial technology was developed and examinations of the specimens of welded joints of tubular parts with a diameter of 102×6 mm of grade steel 35 + steel 20 were performed (Figure 2).

The chemical composition of welding steels is given in Table 1. Mechanical properties of welded joints of tubular parts are given in Table 2. Comparative indices of electric power consumption during welding of one pipe butt during manual arc welding (MAW) and PMIAB are given in Table 3.

Figure 3 shows the specimens of the base and welded joint metal after the tests on impact toughness.

At the place of joining the parts, defects are not observed (Figure 4), decarbonized metal band at the joint boundary is absent. The boundaries conjugation of the metals of steel 20 and steel 35 along the welded joint line is observed (Figure 4).

**Table 3.** Comparative indices of electric power consumption during welding of a one pipe butt during MAW and PMIAB welding

| Size of pipe, mm | Welding method | Electric power consumption per 1 butt, kW/h |
|------------------|----------------|---------------------------------------------|
| 102×6.0 mm | MAW | 0.98 |
| | PMIAB | 0.042 |



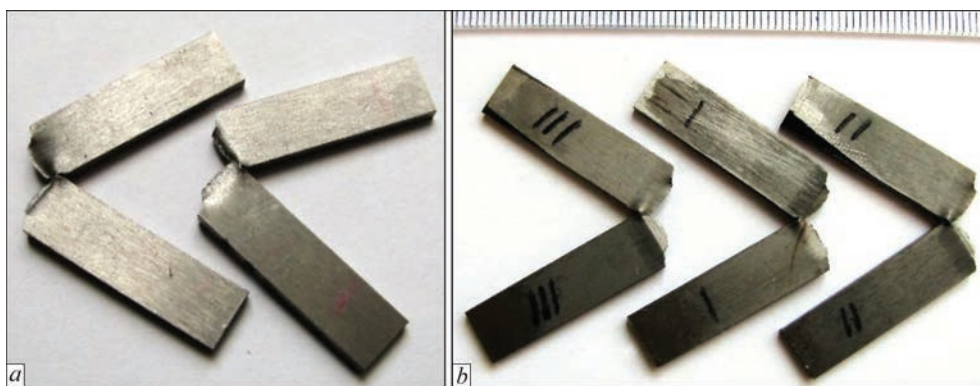**Figure 2.** Welded joint of tubular parts of 102×6 mm

**Figure 3.** Appearance of fractured specimens: *a* — base metal; *b* — welded joint

The metal structure of steel 20 near the joint line is ferritic-pearlitic. The amount of ferrite significantly prevails. Ferrite is precipitated along the former austenite grains (polygonal). The main mass is a lamellar ferrite with an ordered and disordered second phase (Figures 5, 6). The grain ball in the area of overheating (coarse grain) near the joint line corresponds to No.6 according to GOST 5639–82. The further distance from the joint line, the grain is refined to Nos 8, 9 according to the GOST scale.

In the region of a complete recrystallization, the structure is fine-grained, the grain size number is 10, and the structure is ferritic-pearlitic.

The structure of the base metal is ferritic-pearlitic, the grain size number is 8 according to GOST 5639–82. The width of HAZ regions:

● area of coarse grain (area of overheating) — 2300 μm;

● area of fine grain (area of complete recrystallization) — 2000 μm;

● area of partial recrystallization — 1500 μm;

● width of HAZ — 5000 μm.

The metal structure of steel 35 near the joint line is pearlitic-ferritic. The amount of pearlite significantly prevails (Figures 5, 6). In the area of overheating in the HAZ structure pearlitic grains are present, bor-dered by a ferritic grid along the boundaries of the former austenite grains. The amount of ferrite is very small (Figure 6). The grain size number at the area of overheating in the joint line corresponds to 5 (GOST 5639–82). The further distance from the joint line, the grain is refined to number 8.

The area of fine grain differs by a refined structure (ferritic-pearlitic), the grain size number is 10.

Defects in HAZ and the base metal were not detected. Width of HAZ regions are:
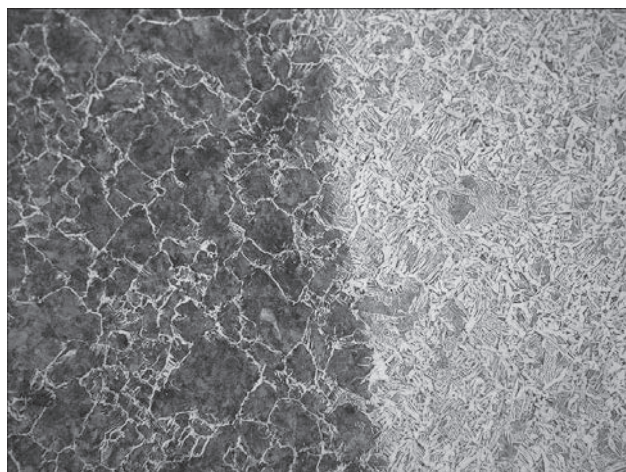


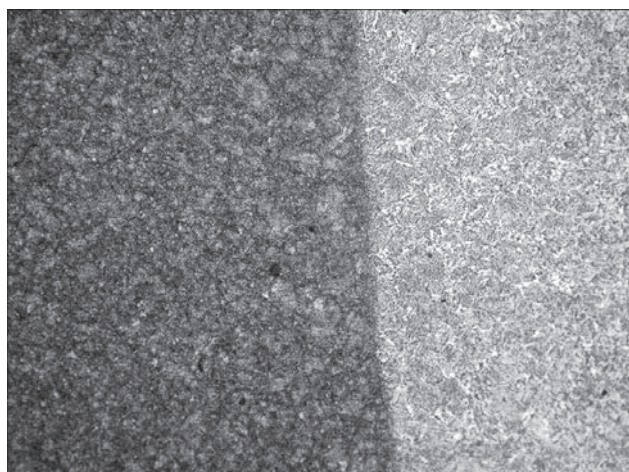**Figure 5.** Microstructure (×100) of metal of joint steel 35 + steel 20



**Figure 4.** General appearance of joint steel 35 + steel 20 (×25)



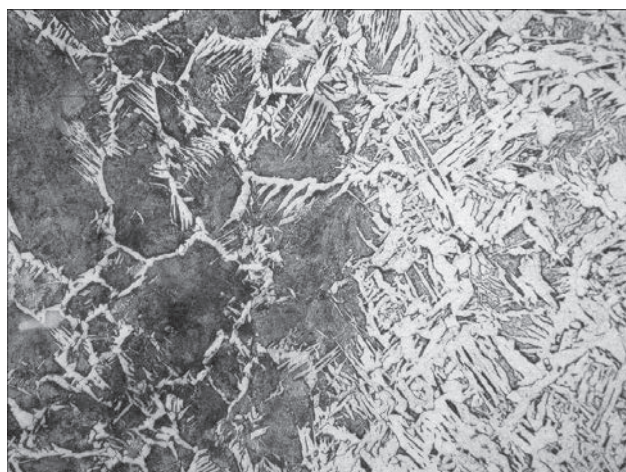**Figure 6.** Microstructure (×400) of metal of joint steel 35 + steel 20

● area of coarse grain (overheating area) — 1500 μm;

● area of fine grain (area of complete recrystallization) — 2400 μm;

● area of partial recrystallization — 2000 μm;

● width of HAZ — 6000 μm.

The results of measuring hardness in the direction of BM steel 20 — HAZ — JL – HAZ — BM steel 35, at a load of 100 g with a step of 100; 200; 500 μm.

Step 500 — BM — 1760, steel 20: HAZ — 1560, 1510, 1570; step 200 – 1760, 1760, 1690, 1690, 1690, 1810, 1810, 1720, 1640, 1640, 1760, 1870, 1850, 1870, 1870, 1870, 1870, 1870, 1930, 1930; step 100 — 2130, 1930, 1930; step 50 – 1930.

JL — 2060, 1930, 1930, 1930.

Steel 35. HAZ: step 100 — 2060, 2280, 2300; step 200 — 2280, 2260, 2450, 2360, 2600, 2540, 2240, 2160,2130, 1990, 1990, 2130, 2130, 2130, 2130, 1910, 1890, 1810, 1810; step 500 — 1930, 1930, 1990, 2060.

Step 500 — BM — 1920, 1810.

As is seen from the given Table, to weld one butt, in PMIAB it is used almost 22 times less electric power than in MAW. This saving is achieved by reducing the welding time of a one butt joint. In addition, arc welding consumes a lot of electric power to melt a larger pool of liquid metal.

The main technical advantages of the developed experimentally industrial technology of welding high-loaded tubular parts are:

● relatively short welding time;

● high efficiency, especially in mass production;

● low energy and materials consumption;

● concentrated heating of ends of welded parts;

● minimum tolerances for flashing and upsetting;

● absence of strict requirements to roughness of side and welded surfaces;

● absence of problems with tolerances of preliminary preparation;

● high ductile properties of welded joints;

● relatively small spattering of metal;

● absence of metal spattering on the inner surface of welded pipes;

● ability to control and register the basic technological parameters during the welding process.

**Conclusions**

1. The optimal conditions were determined, which allow moving the arc steadily in a narrow gap to achieve a relatively uniform heating of welded ends of the tubular parts.

2. A control method was developed that allows moving the arc over the entire welded cross-sectional area of the pipes and forming a uniformly distributed melt on it.

3. The basic conditions for the formation of a welded joint of high-loaded tubular parts were determined.

4. The research and industrial technology of PMI-AB of high-loaded tubular parts with a diameter of up to 120 mm and a wall thickness of up to 6 mm was developed and tested.

1. Hagan, D., Riley, N. (1979) MIAB welding. Pt 2. Fabrication the fiesta rear axle. *Metal Construction*, **12**, 625, 627–629.

2. Ganovski, F.J. (1974) The magnetarc welding process. *Weld. Met. Fab.*, **5**, 206–213

3. *Kenji* Takagi, Hirokazu Otsuka, Fumiho Abakida et al. (1987) *Establishment of optimum welding conditions of magnetically impelled arc butt welding and application to field operation*, IIW, III-880–1987.

4. Edson, D.A. (1982) *Magnetically impelled arc butt welding of thick wall tubes*, IIW, III-726–82, July 1982.

5. Kuchuk-Yatsenko, S.I., Kachinsky, V.S., Ignatenko, V.Yu., et al. (2010) Magnetically-impelled arc butt welding of pipes of steel X70. *The Paton Welding J.* **7**, 29–31.

6. Kachynskyi, V.S., Kuchuk-Yatsenko, S.I., Koval, M.P. (2020) Press magnetically-impelled arc welding of high-strength steel tubular parts of hydraulic cylinders. *Ibid.*, **1**, 43–48.

7. Koval, M.P., Kuchuk-Yatsenko, S.I., Kachynskyi, V.S. (2020) System of control, registration of parameters and monitoring in the process of press welding of pipes using magnetically-impelled arc. *Ibid*., **6**, 36–40

# INFLUENCE OF PULSED ELECTROMAGNETIC FIELD TREATMENT ON STRESS-STRAIN STATE OF CIRCUMFERENTIAL WELDED JOINTS OF ALUMINIUM AMg6 ALLOY

**L.M. Lobanov**[1], **M.O. Pashchin**[1], **O.L. Mikhodui**[1], **O.V. Cherkashin**[1],
**O.M. Timoshenko**[1], **I.P. Kondratenko**[2] and **T.G. Solomiichuk**[1]

[1]E.O. Paton Electric Welding Institute of the NAS of Ukraine
11 Kazymyr Malevych Str., 03150, Kyiv, Ukraine. E-mail: office@paton.kiev.ua
[2]Institute of Electrodynamics of the NAS of Ukraine
56 Peremohy Prosp., 03057, Kyiv, Ukraine

At present a growing interest in pulsed electromagnetic field treatment technologies is observed to improve the mechanical properties of metals, alloys and welded joints. Based on the pulsed electromagnetic field treatment, effective methods can be developed to optimize the stress-strain state of aluminium alloy products in order to extend their residual life for the use in aircraft and rocket, shipbuilding and other industries. The aim of the work is to study the influence of pulsed electromagnetic field treatment on the stress-strain state of circumferential welded joints of aluminium AMg6 alloy. An original experimental procedure was developed to study the kinetics of the electrodynamic pressure force during treatment of metallic materials with a pulsed electromagnetic field. It is shown that as a result of treatment with a pulsed electromagnetic field in the same conditions, the value of P increased with the use of the screen, which is predetermined by the increase in the active additional volume of the electric conductive medium. It was established that the use of the screen during treatment by a pulsed electromagnetic field helps to reduce the level of residual tensile welding stresses and improve the accuracy of circumferential welded joints. 8 Ref., 3 Tables, 8 Figures.

*K e y w o r d s : pulsed electromagnetic treatment, aluminium alloy, circumferential welded joints, stress-strain state, residual welded joints, additional screen*

The development of modern industry need the study of advanced energy-saving technologies to improve the service properties of metal structures. In this regard the development of methods for treatment of metal materials and welds is promising, which is based on the effect of a pulsed electromagnetic field (PEMF). These are electrodynamic treatment (EDT) and direct pulsed electromagnetic field treatment (PEMFT). The advantages of EDT are given in [1], and its disadvantages, unlike PEMFT, include the need for contact interaction with the surface of the treated metal.

At present, an increased interest in PEMFT technologies is observed in various fields of metal treatment [2], such as forming, reduction, welding, calibration, etc. In [3] the calculations and designs of inductor systems for straightening buckling of automobile body structures at PEMFT are considered.

Based on the results [2, 3], it should be noted that PEMF is an effective instrument for influencing the shaping and mechanical properties of metals and alloys [4], as well as welded joints [5]. On the basis of PEMFT, effective technologies can be developed to control the stress-strain state of thin-sheet metal materials, which include aluminium alloys used in the aircraft and rocket, shipbuilding industries, which is relevant for modern production.

The aim of this work is to study the effect of PEMF on the residual stress state of welded joints of nonferromagnetic materials on the example of aluminium AMg6 alloy.

**Procedure, equipment and specimens for investigations.** As is known, electric current pulse (ECP) passing through the conductors of an inductor in an approximate electric conductive medium excite eddy currents. As is proved in [6], regardless of how the inductor is located relative to the plane of the electric conductive medium, the circuits of the induced current are located parallel to the plane of the surface (medium). As a result of interaction of induced currents with a pulsed magnetic field, that excited these

L.M. Lobanov — https://orcid.org/0000-0001-9296-2335, M.O. Pashchin — https://orcid.org/0000-0002-2201-5137,
O.L. Mikhodui — https://orcid.org/0000-0001-6660-7540, O.V. Cherkashin — https://orcid.org/0000-0002-7596-7780,
O.M. Timoshenko — https://orcid.org/0000-0001-9163-1067, I.P. Kondratenko — https://orcid.org/0000-0003-1914-1383,
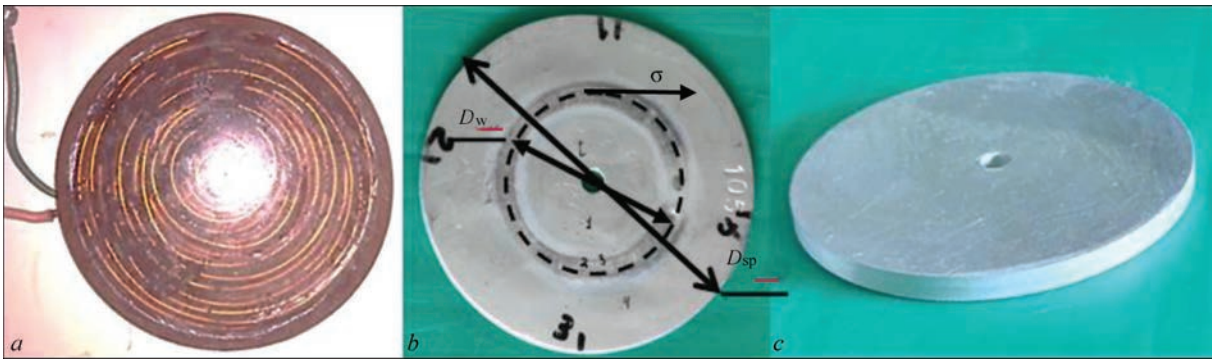T.G. Solomiichuk — https://orcid.org/0000-0002-3038-8291

**Figure 1.** Appearance: *a* — flat multiturn inductor; *b* — specimen of circumferential welded joint of AMg6 alloy with a thickness δ = 1.0 mm, where $D_{sp}$ = 90 mm and $D_w$ = 45 mm are, respectively, the diameters of the specimen and the weld; σ is the normal component of residual stresses; *c* — screen conducting current with 90 mm diameter and 5 mm thickness

**Table 1.** Characteristics of flat inductor for PEMFT

| Inductance* $L$, µH at the frequency *f*; kHz 1.0 | Outer diameter $d_{ind}$, mm | Inner diameter $d_{ind}$, mm | Height $h_{ind}$, mm | Material of winding | Diameter of winding, mm | Number of turns, *n* |
|---|---|---|---|---|---|---|
| 121 | 95 | 5 | 14 | Wire, copper of M1 grade | 1.0 | 50 |

*The values of inductance are determined at the value of air gap of 0.1 mm between the inductor and the specimen of AMg6 alloy with a thickness δ = 5 mm.

**Table 2.** Modes of TIG surfacing of circumferential «idle» beads on the specimenns of AMg6 alloy for PEMFT

| Thickness δ, mm | Arc stickout, mm | Argon consumption, l/min | Diameter of W-electrode, mm | Welding speed $v_w$, m/h | Welding current $I_w$, A |
|---|---|---|---|---|---|
| 1.0 | 1.5 | 10 | 1.6 | 13.4 | 39 |

currents, an electrodynamic force arises that has three spatial components, but only one normal component of the electrodynamic force reveals to be much higher than tangential components. This force exerts an active load on the area with a pressure of force $P$ and, as a consequence, changes the stress state of the treated material. Provided that the density $j$ of the induced



**Figure 2.** Appearance of hardware complex for registration of time distributions of ECP — $I$ and $P$ at PEMFT of metal materials: *1* — device for processing and visualization of measurement results; *2* — device for fixing the inductor for PEMFT and registration of values of the force $P$; *3* — digital device for registration of values of ECP amplitude and duration; *4* — power source for PEMFT

electric current reaches the value $j \geq 1$ kA/mm² in the treated metal, the conditions are created to realize the electroplastic effect (EPE) [4]. This contributes to the intensification of plastic deformation of the material and, as a consequence, a controlled change in its stress state. The EPE mechanism operates according to the theory of electron-dislocation interaction, in which at $j \geq 1$ kA/mm² in the material conditions for the interaction of conduction electrons with dislocations are created, resulting in the breakthrough of the last structural barriers, their reproduction and advancement.

To generate PEMF, a flat multiturn inductor was used (Figure 1, *a*), and to realize charged and discharged cycles of PEMF, the power source is used based on a capacitor system with a total capacity $C = 5140$ µF, a charging voltage of up to 800 V and a stored energy $E_s \sim 1.6$ kJ. The characteristics of the inductor are presented in Table 1.

To evaluate the efficiency of PEMFT, plane specimens in the form of a disc with a thickness and diameter of relatively δ = 1.0 and $D_{sp}$ = 90 mm of aluminium AMg6 alloy were used. The circumferential welded joints were simulated by automatic TIG surfacing in the Ar atmosphere on the surface of the discs of the «idle» beads on the mode (Table 2) along the circle line with a diameter $D_w$ = 45 mm. The method of elec-
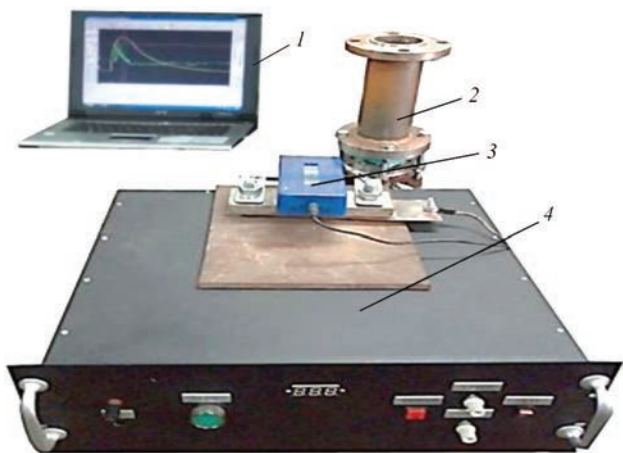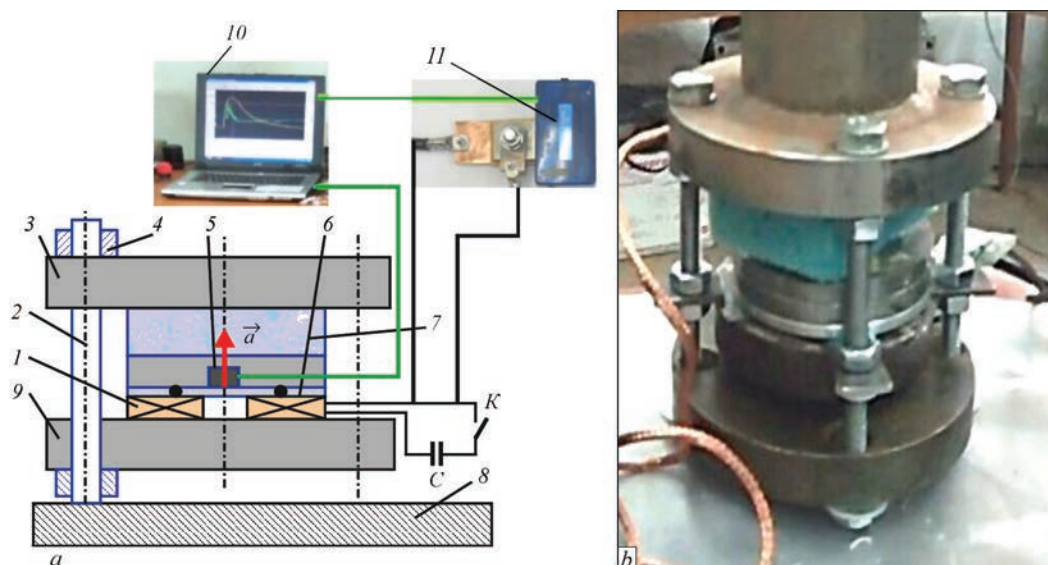
**Figure 3.** Device for registration of time distributions of ECP and $P$ included in the hardware complex for PEMFT (Figure 2): $a$ — structural design where $1$ — inductor; $2$ — pin; $3$ — upper plate; $4$ — pressing nut; $5$ — acceleration sensor; $6$ — specimen-simulator of welded joint; $7$ — pressure damper; $8$ — base support; $9$ — lower plate; $10$ — system for registration and processing of received data; $11$ — digital device for data processing; $C$ — power source; $K$ — key for starting discharge cycle; $a$ — acceleration vector; $b$ — appearance of the device

tron speckle interferometry [1] was used to evaluate the normal component σ (Figure 1, $b$) of the residual stressed state of welded joints and vertical movements of the disc edges before and after PEMFT. During treatment, an electric conductive screen in the form of a disc of AMg6 alloy with a diameter and thickness of 90 and 5.0 mm, respectively was used (Figure 1, $c$).

The parameters of ECP were studied using a measuring digital device on the base of an noninductive shunt, designed to record the amplitude value of unipolar ECP. In addition to the value of the current amplitude, the device measured the pulse duration and the number of ECPs from the beginning of operation. The time distribution of the force $P$ was recorded using Kistler 8042 acceleration sensor [7]. The appearance of the hardware complex for registration of time distributions of ECP — $I$ and $P$ is shown in Figure 2.

The structural design and appearance of the device $2$ (Figure 2) are shown in Figure 3. The scheme of registration of PEMF parameters works as follows. Closing the discharge circuit with the key $K$ starts the transient process of the discharge capacitive accumulator on the active-inductive load. The parameters of the power source and its electrical circuit provide an aperiodic type of a transient process with unipolar current pulses, the parameters of which are registered by the digital device $11$. The discharge current excites PEMF during passing through the inductor $1$. In the specimen of metal $6$, which is located above the inductor at the interaction with PEMF, eddy currents are induced, the result of which interaction with PEMF is the formation of electrodynamic force $P$, which causes repulsion of the specimen of a finite mass $m$ from

the inductor (which is rigidly fixed) with acceleration $a$. The time distribution $a$ is registered by the acceleration sensor $5$, which is fixed on the specimen. On the top of the «sensor-specimen» assembly, pressure damper $7$ made of sparse elastic material is installed, which almost does not hinder the free acceleration of the assembly. The measuring system is fixed by clamping nuts $4$ and studs $2$ between the upper $3$ and lower $9$ plates, which are mounted on the base support $8$. The force $P$ is calculated by hardware as a result of multiplying mass by acceleration. The conditions for fixing the specimens, which provided their acceleration, were set by the power circuit, shown in Figure 3, $a$.

The registration of the time distributions of ECP — $I$ and $P$ after a single discharge of the capacitor was performed at a charging voltage $U = 200–800$ V under the conditions of acceleration of the specimens with a thickness δ = 1.0 mm without a screen conducting current (Figure 1, $c$) and with its application — δ = 1 + 5 mm.

After registration of $I(t)$ and $P(t)$, PEMFT of the specimens was performed, the scheme of which (with the use of the screen) is shown in Figure 4. To provide the conditions of treatment, the damper and acceleration sensor were removed. With the use of fixing elements $5$ and $6$, a rigid fixation of the specimen $4$ and the screen $9$ between the lower $7$ and upper $2$ plates was provided, which are placed on the base support $8$. During the discharge of the capacitor a repulsive force $P$ arised, which exerted pressure on the specimen.

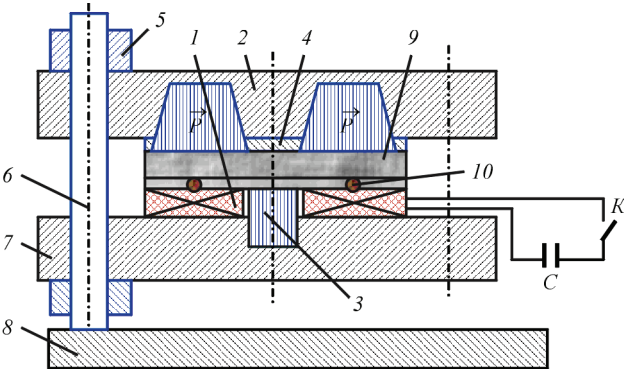PEMFT of the specimens with a thickness δ = 1.0 mm and assembly of the specimen δ = 1.0 mm

**Figure 4.** Structural design of PEMFT of metal materials: *1* — inductor; *2* — upper plate; *3* —axis for mounting inductor; *4* — specimen of welded joint of AMg6 alloy δ = 1.0 mm; *5* — clamping nut; *6* — pin; *7* — lower plate; *8* — base support; *9* — current-conductive screen (Figure 1, *c*); *10* — specimen-simulator of welded joint; *P* — diagram of the distribution of electrodynamic force on the specimen surface; *C* — source of PEMF; *K* — key for starting discharge cycle



**Figure 5.** Time distributions of electrodynamic pressure force *P* and current force *I* at PEMFT of specimens of AMg6 alloy δ = 1.0 mm without a screen at the charge voltage *U* = 800 V, where $t_1$ and $t_p$ are respectively periods of action of *P* and *I*

with a current-conductive screen δ = 5.0 mm (Σδ = = 6 mm) was performed. The treatment was performed by a series of eight ECPs on the mode with increasing the values of *U* in the following sequence: $U_1$ = 200 V, $U_2$ = 400 V, $U_3$ = 600 V, $U_4$–$U_8$ = 800 V. ECPs at $U_1$–$U_3$ contributed to the gradual reaching the nominal mode, and ECPs at $U_4$–$U_8$ — generation of PEMF for specimens treatment. The choice of the number of ECPs at a voltage of 800 V is based on the data of [4].

**Results of experiments and their discussion.** The time distributions of the oscillograms *I*(*t*) and the force *P*(*t*) at PEMFT of the disc δ = 1.0 mm without the screen are shown in Figure 5. It should be noted that the pressure *P*, which determines the change in the stress state of the specimens, acts during the period of the first half-wave of the force. The subsequent damped oscillations of *P*, which is a consequence of the contact of the specimens with the damper *7* (Figure 3) and which are reflected in Figure 5, were not taken into account when estimating the amplitude values of the force. This is associated with the fact that damped oscillations occur only during the registration of the values of *P* and are excluded under the conditions of rigid fixation of the specimens (Figure 4),

under which PEMFT was performed in order to affect the stress-strain state of welded joints. When the possibility of movement of the specimen under the conditions of its fixing is excluded, the action of the force *P* initiates relaxation of stresses in the metal.

The amplitude-frequency characteristics of the pressure force *P* and the current force *I* are given in Table 3, according to which in the investigated range of treatment modes the time period $t_I$ of the action of ECP provided the duration of the current pulse, which corresponds to the frequency at which the depth of current penetration into the AMg6 alloy reached a value higher than 10 mm. Therefore, during treatment of the specimens with a thickness δ = 1.0–6.0 mm with the pulses of such duration, PEMF is revealed on the back side of the specimen. The attenuation of the induced current occurs according to the solution of the nonstationary problem for distribution of electromagnetic field vectors [8]. In any case, at the selected parameters of the inductor, the thickness of the specimen treated by the pulsed electromagnetic field will have little effect on running the transient process of the discharge of the capacitor. The electromagnetic force *P* will grow with increasing thickness, as it is determined as an integral value in a certain volume, which is confirmed by the data in Table 3 and the dependence *P* = *f*(*I*) at the variation δ, which are shown in Figure 6. At the growth of δ to 6.0 mm as a result

**Table 3.** Amplitude-frequency characteristics of *P* and *I* at PEMFT of specimens of AMg6 alloy at different values of *U* and δ

| Number | Characteristics of PEMFT of specimens | *U*, V | Δ, mm | *P*, kN | $t_p$, ms | *I*, kA | $t_I$, ms |
|--------|---------------------------------------|--------|-------|---------|-----------|---------|-----------|
| 1 | Without the screen | 200 | 1.0 | 0.234 | 0.3 | 0.733 | 8.8 |
| 2 | | 400 | | 0.812 | 0.28 | 1.427 | 10.8 |
| 3 | | 600 | | 3.694 | 0.48 | 2.199 | 11.9 |
| 4 | | 800 | | 4.871 | 0.48 | 2.864 | 12.6 |
| 5 | With the screen | 200 | 1.0 + 5.0 | 1.267 | 1.36 | 0.82 | 7.7 |
| 6 | | 400 | | 3.589 | 1.2 | 1.593 | 9.4 |
| 7 | | 600 | | 6.690 | 1.2 | 2.316 | 10.0 |
| 8 | | 800 | | 10.999 | 1.0 | 2.952 | 10.58 |

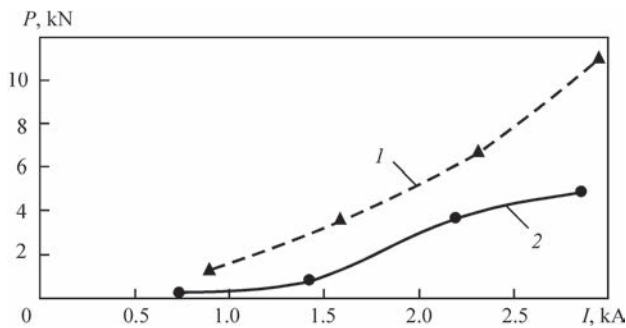**Figure 6.** Influence of amplitude values of ECP — *I* on the pressure force *P* at PEMFT of specimens of circumferential welded joints δ = 1.0 mm of AMg6 alloy: *1* — PEMFT without the screen; *2* — PEMFT with the screen

of applying the screen (curve *2*), the values of *P* are increased twice as compared to PEMFT of specimens without the screen δ = 1,0 mm (curve *1*). The decrease in the pressure force *P* with a decreasing thickness δ of the disc is predetermined by the surface effect, i.e. nonuniform distribution of the density of induced currents in depth and reduction of the active volume of the electric-conductive medium, which is the electromagnetic load of the inductor. Therefore, for efficient treatment of thin specimens, it is necessary to reduce the duration of the current pulse. This path, obviously, requires a change in the parameters of the discharged circuits, which is not appropriate. The paper proposes the simplest and the most effective way in the form of installing additional layers of a related material, in which the equivalent thickness will be optimal in terms of achieving the highest value of the force *P* of the electromagnetic pressure.

The effectiveness of PEMFT effect on the residual distortion of the specimens treated under the above-mentioned conditions is confirmed by the data shown in Figure 7, *a–c*. The values of vertical movements of the disc edges *f* (Figure 7, *a*) were recorded according to the procedure [1] at the points Nos *1–4* (Figure 7, *c*) with a fixed angular distance $l_\alpha$ of 90° between the adjacent points. Performance of PEMFT without the screen (Figure 7, *d*, curve *2*) and with its use (curve *3*) allows reducing the value of edges movements *f* of the discs, respectively, to two and eight times as compared to the specimens that were not subjected to PEMFT.

Figure 8 shows the results of the PEMFT effect on the normal component σ of the residual stresses in the center of the weld zone (WZ) and in the zone around the weld (AWZ) at a distance of 10 mm from the weld line. Taking into account the bending of the discs (Figure 7), the consequence of which is the imbalance of the residual stress diagrams, as an estimate of the PEMFT effect on the stress state, the peak values of σ in WZ and AWZ in the specimens in the initial state and under the set treatment conditions were determined. It can be seen that in general PEMFT has
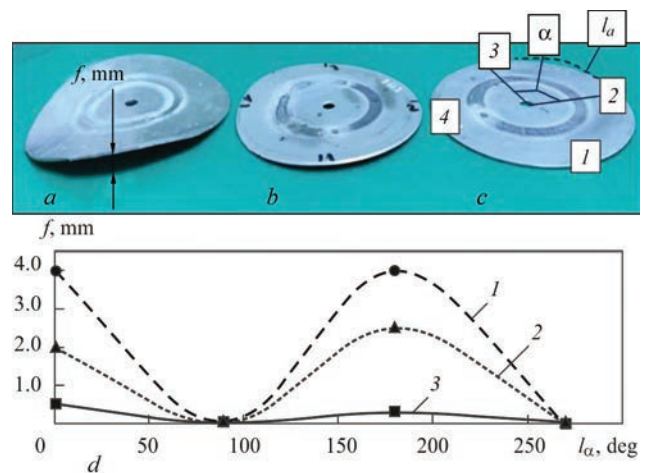


**Figure 7.** Residual distortions of specimens of circumferential welded joints of AMg6 alloy: *a* — appearance (A) of the disc without treatment, where *f* is the movement of the edges of the disc; *b* — A after PEMFT without the screen; *c* — A after PEMFT with the screen, where *1–4* is the number of the point of measurement of displacements, α and $l_\alpha$ are respectively the angle and angular distance between the points *2–3*; *d* — vertical displacements f of edges of the disc, where the curve *1* — without PEMFT; *2* — after PEMFT without the screen; *3* — after PEMFT with the screen

a positive effect on the residual stress state of circumferential welded joints of AMg6 alloy with a thickness δ = 1 mm.

Although the initial (before PEMFT) values of σ during treatment without a screen (Figure 8, *a*) and with a screen (Figure 8, *b*) differ, which is related to low rigidity of the discs, it can be seen that the use of the screen has a positive effect on relaxation of stresses at PEMFT. This is confirmed by the comparison between the diagrams *a*, *b* and *c*, *d*. Thus, treatment without and with the use of the screen led to a decrease in the initial values of σ in the active zone of tension (WZ) by 36 and 56 %, respectively, and reactive compression (AWZ) by 50 and 80 %. The obtained results are explained by the influence of the field on the intergranular boundaries and local heating
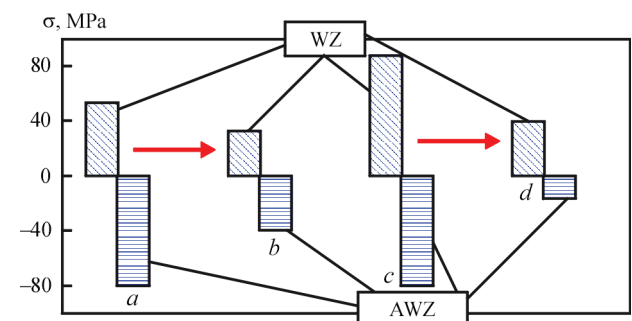


**Figure 8.** Influence of PEMFT on the normal component σ of residual stresses in welds (W) and in the zone around the weld (AWZ) of circumferential welded joints of the specimens of AMg6 alloy with a thickness δ = 1 mm: *a* — peak values of specimens in the initial state; *b* — σ after PEMFT without the screen; *c* — σ of specimens in the initial state; *d* — σ after PEMFT with the screen

of the grains [3], but require a more detailed study of the evolution of the fine structure of nonferromagnetic materials under the action of PEMF.

Taking into account the abovementioned, it should be noted that PEMFT can be an effective mean of improving the accuracy of manufacturing elements of thin-sheet welded structures of aluminium alloys, and also the control of their residual stress states. The advantages of PEMFT over the general heat treatment include its much lower energy consumption and the absence in the need for special equipment. It is known that the local heat treatment (LHT) of aluminium alloys is not effective because of a high thermal conductivity of the latter, and the use of PEMFT, which is characterized mainly by nonthermal mechanism of action, is more effective.

For application of PEMFT in the industrial production, in particular in aircraft and «white» shipbuilding, it is advisable to determine several branches that allow increasing the efficiency of treatment:

● optimization of electrophysical parameters of PEMFT, which will provide the maximum efficiency of the influence of field components on the stress-strain state and structure of nonferromagnetic materials;

● development and manufacture of inductor systems of increased strength and thermal stability;

● development and manufacture of energy-efficient pulsed power sources with optimal characteristics of charging and discharging cycles;

● development of PEMFT technologies for regulation of stress-strain states of welded, surfaced and sprayed structures of conductive materials.

## Conclusions

1. On the basis of using the acceleration sensor, the experimental procedure of studying kinetics of electrodynamic pressure force on the specimens of circumferential welded joints during their treatment by a pulsed magnetic field was developed (PEMFT).

2. It was established that a decrease in the pressure force of the pulsed electromagnetic field with decreasing thickness of specimens of circumferential welded joints of AMg6 alloy is predetermined by a nonuniform distribution of density of induced currents and a decrease in the active volume of the electric-conductive medium, which is electromagnetic load of the inductor.

3. A method was proposed to increase the efficiency of PEMFT by forming additional layers of a related material by installing a screen that conducts a current at which the equivalent thickness will be optimal to achieve the highest value of the electromagnetic pressure.

4. It was established that realization of PEMFT without a screen that conducts current and with its use allows reducing the value of vertical movements of specimens of circumferential welded joints by respectively two and eight times as compared to the specimens that were subjected to treatment.

5. It was found that PEMFT without and with the use of the screen leads to a decrease in the initial tensile welding stresses by 36 and 56 %, respectively, and compression stresses by 50 and 80 %, which is explained by the effect of the field on intergranular boundaries and local grain heating and requires additional investigations.

6. The directions of increasing the PEMFT efficiency for its faster use in industrial production were formulated, in particular: optimization of electrophysical parameters of PEMFT, development of advanced induction systems, pulsed power sources and technologies of regulation of welded, surfaced and sprayed structures by stress-strain states.

1. Lobanov, L.M., Pashchin, M.O., Cherkashyn, O.V. et al. (2019) Prospects for application of electromagnetic fields in welding and related processes. *The Paton Welding J.*, **8**, 29–36.

2. Batygin, Yu.V., Lavinsky, V.I., Khimenko, L.T. (2003) *Pulsed magnetic fields for advanced technologies*. Vol. 1. 2nd Ed. Ed. by Yu.V. Batygin. Kharkov, MOST-Tornado [in Russian].

3. Turenko, A.N., Batygin, Yu.V., Gnatov, A.V. (2009) *Pulsed magnetic fields for advanced technologies*. Vol. 3: Theory and experiment of attraction of thin-walled metals by pulsed magnetic fields: Monography. Kharkov, KhNADU [in Russian].

4. Strizhalo, V.A., Novogrudsky, L.S., Vorobiov, E.V. (2008) *Strength of materials at cryogenic temperatures taking into account electromagnetic fields*. Kiev, IPS [in Russian].

5. Lobanov, L.M., Kondratenko, I.P., Pashchin, N.A. et al. (2016) Comparison of influence of pulsed effects of magnetic and electric fields on stressed state of welded joints of aluminium alloy AMg6. *The Paton Welding J.*, **10**, 8–13.

6. Vasetsky, Yu.M., Dzyuba, K.K. (2017) Analytical calculation method of quasi-stationary 3D electromagnetic field of current passed on contour of arbitrary configuration near conductive body. *Tekhnichna Elektrodynamika*, **5**, 7–17 [in Russian]. DOI: https://doi.org/10.15407/techned2017.05.007.

7. *Kistler Instrumente* AG. *Quartz Accelerometer 8042* (Passport).

8. Rashchepkin, A.P., Kondratenko, I.P., Karlov, O.M., Kryshchuk, R.S. (2019) Electromagnetic field of inductor with E core for magnetic-pulsed treatment of materials. *Tekhnichna Elektrodynamika*, **6**, 5–12 [in Ukrainian]. DOI: https://doi.org/10.15407/techned2019.06.005.

# INFLUENCE OF TECHNOLOGICAL PARAMETERS
# OF SLM-PROCESS ON POROSITY OF METAL PRODUCTS

**S.V. Adjamskyi**[1,2], **G.A. Kononenko**[2,3] and **R.V. Podolskyi**[3,4]
[1]Oles Honchar Dnipro National University
72 Gagarin Prosp., 49000, Dnipro, Ukraine. E-mail: dsit@dnu.edu.ua
[2]LLC «Additive Laser Technology of Ukraine»
144 Rybin'ska Str., 49000 Dnipro, Ukraine. E-mail: info@alt-print.com
[3]Z.I. Nekrasov Institute of Iron and Steel of the NAS of Ukraine
1 Academician Starodubov Sq., 49050, Dnipro, Ukraine. E-mail: office.isi@nas.gov.ua
[4]National Metallurgical Academy of Ukraine
4 Gagarin Prosp., 49000, Dnipro, Ukraine. E-mail: kaf.tom@metal.nmetau.edu.ua

Selective laser melting is one of the modern methods of manufacturing parts and assemblies of complex geometry, which are difficult or impossible to reproduce in the conditions of traditional manufacturing. The problem of this manufacturing is that a product quality depends on many factors, which can be divided into such main groups as equipment, material, process, part and finishing. The influence of the specific energy density of scanning the heat-temperature Inconel 718 alloy in the 3D printer Alfa-150 (ALT Ukraine) of the Ukrainian production was investigated. The influence of SLM-technology parameters on the quality of final products is shown and the analysis of the influence of technology factors on the quality of finished products is performed. As a result of metallographic examinations, it was found that the distance between the passes of the laser, at which the estimated overlap of a single track is 25 %, the conditions of deep penetration are created and at the root of the track as a result of collapsing holes (so-called keyhole), large elongated pores are formed. At the estimated overlap of a single track of 17 %, a small number of tiny rounded pores is formed. At the calculated overlap of 0–8 %, a structure with a minimum number of pores is formed. When the distance between the passes of the laser exceeds the width of a single track at a given combination of power and laser scanning speed, the cases of partial fusion of adjacent tracks are observed, pores with sharp edges are formed, which are stress concentrators — the most dangerous in terms of a product reliability. Thus, a rational overlap of tracks during selective laser melting was established, which ranges from 0 to 8 % of the width of a single track at specific process parameters. 21 Ref., 2 Tables, 4 Figures.

*K e y w o r d s :  selective laser melting, technological factors, quality system, Inconel 718, specific energy density*

The modern method of additive manufacturing, called selective laser melting (SLM), allows manufacturing 3D-products in layers [1]. Preparation for printing begins with 3D-modeling of the object built in the CAD system in the STL format[*]. As a result, we receive the element split on the voxel structure [2] with a certain set of parameters suitable for printing. At digital processing the model is divided into layers from 20 to 100 µm thickness and vectors of a laser beam movement are formed.

The manufacturing process begins with applying a layer of metal powder required for printing one layer on a metal substrate, which is attached to the support structure and moves in the vertical direction along the $Z$ axis. The printing process takes place inside the chamber with inert gas (usually argon or nitrogen is used), which maintains a strictly controlled atmosphere. Also, this allows printing using powder of aluminium and titanium alloys, because oxygen does not

get into the chamber, which allows avoiding oxidation of the used material. Each 2D-layer of the object is sintered together, copying the shape of a digital STL drawing. The metal powder melts under the influence of a laser beam directed along the $X$ and $Y$ axes by two surfaces that reflect the beam at a high speed. The power of the laser emitter is usually in the range of 200–1000 W.

With the help of SLM process, samples with a complex geometry can be manufactured that are impossible or difficult to fabricate by other traditional methods of manufacturing. [3].

While realizing SLM technology, metal powders in the layer melt quickly [4] and solidify in the melt pool (cooling rates range from $10^3$ to $10^8$ K/s) with a short-term nonequilibrium phase transition and a highly dispersed microstructure is formed [5, 6]. This leads to some significant differences in mechanical properties between products manufactured by the

S.V. Adjamskyi — https://orsid.org/0000-0002-6095-8646, G.A. Kononenko — https://orsid.org/0000-0001-7446-4105,
R.V. Podolskyi — https://orsid.org/0000-0001-7446-4105

methods of casting, forging and SLM [7, 8]. The microstructure during the conventional manufacturing process, such as casting and deformation, has coarser grains with a high liquation because of a low cooling rate during solidification and significant defects of shrinkage origin caused by a large volume of crystallizing melt. In addition, in cast and wrought alloys, the management of the microstructure is complicated, whereas it is easier to be controlled during the SLM process by changing manufacturing parameters [9].

The melt pool of one track has an arc configuration. Such a shape is a consequence of the energy distribution of the laser beam according to Gauss. The shape and overlap of the melt pools is seen in the microstructure of the material, manufactured by selective laser melting. Small dendritic and cellular structures with the size of structural elements having some micrometers are revealed within each track.

However, the surface of these samples as compared to the processes of precision forging and machining operation shows a large surface roughness (Ra), which is about 10–20 μm. In some fields, such as medicine, the high value of Ra can demonstrate good biological properties. For example, the implant Ti–6Al–4V manufactured by SLM process with a high value of Ra can be preferred for the growth of a bone. In a dental prothesis made of the Co–Cr alloy manufactured by the SLM method with a high value of Ra, the adhesion between the metal and ceramic may increase. Worldwide, the values of Ra range from 6 to 11 μm and tend to decrease.

Thus, SLM technology allows providing a high quality of products (accuracy and uniqueness of geometry, high complex of mechanical properties, high density, homogeneity of microstructure and chemical composition) and a wide range of the used materials allows it to find application in such fields as medical, dental, machine-building, automobile and aerospace industries.

The need for a systematic approach to quality management of products is explained by the diversity and interrelation of external and internal factors influencing the quality, and also by the continuity of its formation and provision. The quality of products manufactured applying SLM-technology depends on many factors, which can be divided into such main groups as equipment, material, process, part and finishing.

The quality of final products is significantly affected by the parameters of the SLM process. The main among them include laser power, speed and trajectory of laser beam scanning [10–15], distance between the scanning tracks and thickness of the layer of powder material.

The quality of a product, including the final density of the metal and the surface roughness, first of all, depends on the characteristics of the melt pool (shape and size), which are largely controlled by changes in the specific energy density of the laser beam, which is essentially a measure of energy, which is supplied in the process of printing [15, 16]. The control of the specific energy density can be achieved by changing the relevant controlled parameters. Laser power $P$ (W), scanning speed $V$ (mm/s), distance between the tracks (melt pool overlap), $d$ (mm) and layer thickness $t$ (mm) are the most important parameters and are related to specific energy density of the laser as:

$$E = P/(Vdt).$$

Rational modes of the process should stably provide a positive result. The level of power and speed of the laser beam scanning at a certain thickness of the powder layer for a certain material and equipment should provide the formation of a stable track.

In essence, the distance between the laser passes regulates the amount of overlap of adjacent tracks. The effect of the distance between the laser passes is often investigated without taking into account the size of the tracks [17]. Such results have a narrow scope of application and do not have a general nature, as far as depending on the power and speed of scanning the laser beam, the geometric parameters of the melt pool change. An approach for estimating track overlap is also known. However, there is no single opinion on the rational value of the overlap of adjacent tracks. Usually scientists are of the opinion that this value is in the range of 30–50 % [18, 19]. Others believe that the distance between the laser passes should be close to the track width to provide a minimal porosity [20].

Aim of the work is to determine the rational modes of SLM-process when using metal powder of high-temperature Inconel 718 alloy in the equipment «ALT-Ukraine» at a working layer thickness of 50 μm.

**Material and procedure of investigations.** The material for the manufacture of samples was the powder of Inconel 718 alloy of the H.C. Starck AMPER-PRINT 0181.074 manufacturer with a particles size of 45 + 15 μm.

The source material was examined using a scanning electron microscope REM-106 (Figure 1, *a*) to determine the shape and size of the particle. Figure 1, *b* shows the results of the analysis.

Samples with a size of 10×10×5 mm of high-temperature nickel Inconel 718 alloy at a layer thickness of 50 μm were manufactured, the actual chemical composition of the finished product is presented in Table 1. The control of the chemical composition was performed using the precision analyzer «EX-
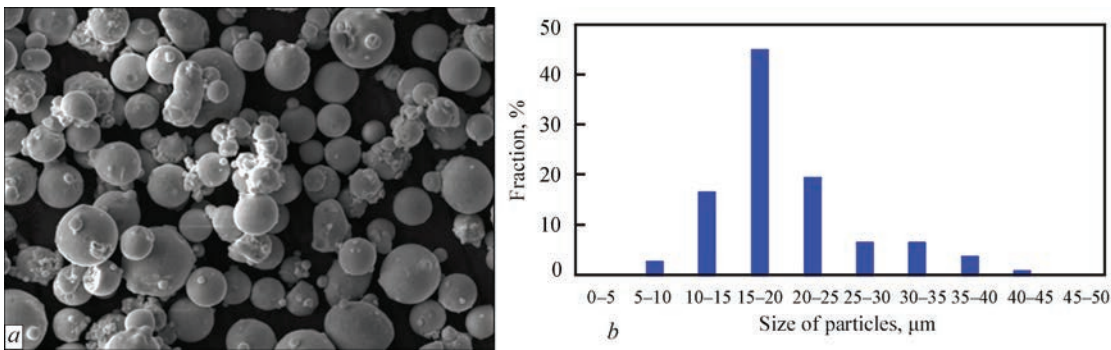
**Figure 1.** Particles of source material INCONEL 718 at a magnification of 500 (*a*) and results of grain-size analysis (*b*)

**Table 1.** Actual chemical composition of Inconel 718 alloy

| Chemical element | Ni | Cr | Mo | Nb | Mn | Co | Cu | Al | Ti | Si | C | Fe |
|---|---|---|---|---|---|---|---|---|---|---|---|---|
| Content, wt.% | 52.5 | 19.5 | 3 | 5.1 | 0.7 | 0.2 | 0.6 | 0.8 | 0.2 | 0.2 | 0.08 | Balance |

PERT 4L». The samples were grown in argon, in the «ALFA-150» installation of «LLC Additive Laser Technology of Ukraine» production. As a strategy for building a solid body, a zigzag (end of the previous track next to the beginning of the next track) printing process with a 67° rotation of the next layer relative to the previous one was used (Figure 2). The study of the microstructure was performed using an optical microscope AXIOVERT 200M MAT. Metallographic examinations of the microstructure of the metal were performed after $CuSO_4 + HCl$ etching in a plane parallel to the direction of growing the sample (*X–Z*).
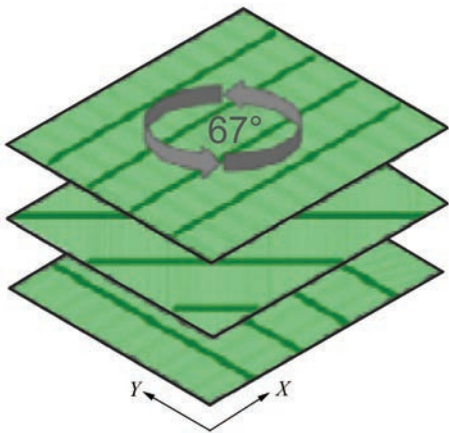
In the process of sample manufacturing, the parameters of the process of tracks overlapping between



**Figure 2.** Scheme of scanning for reproduction of solid body
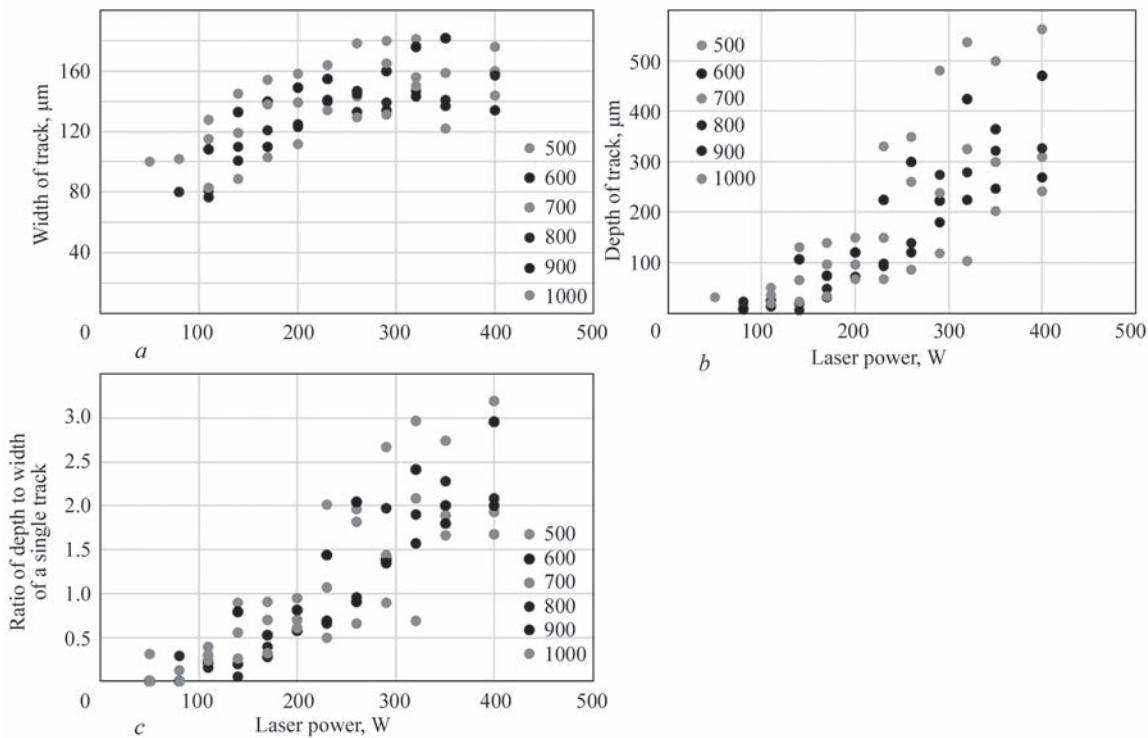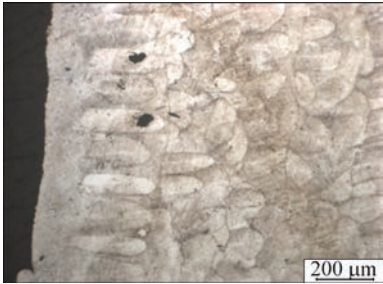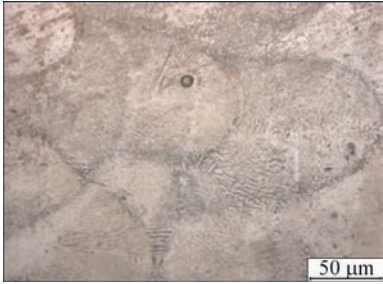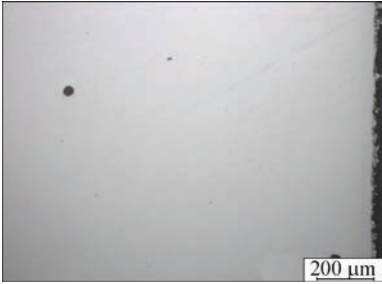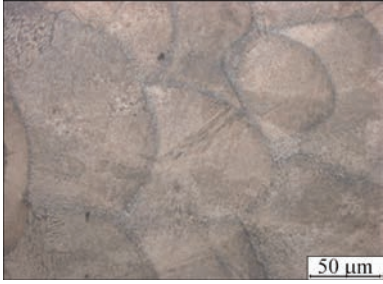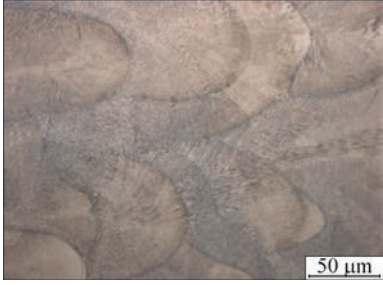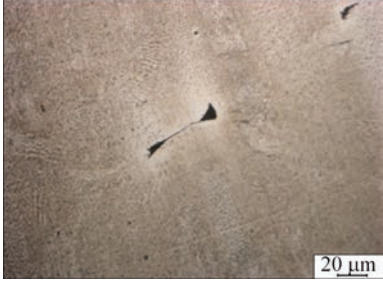


**Figure 3.** Geometric parameters of single tracks at different level of laser power (50–400 W) and scanning speed (500–1000 mm/s): *a* — width of a single track; *b* — depth of a single track; *c* — ratio of depth to width of a single track

**Table 2.** Microstructure of investigated samples depending on distance between laser beam scanning

| Distance between the tracks, mm (calculated overlap, %) | Microstructure of investigated sample (etched by $CuSO_4$ + HCl) | Microstructure of investigated sample in the polished state | Porosity of samples, % |
|---|---|---|---|
| 0.09 (25) |  200 µm |  100 µm | 1.75 |
| 0.10 (17) |  50 µm |  200 µm | 0.48 |
| 0.11 (8) |  50 µm |  200 µm | 0.02 |
| 0.12 (0) |  50 µm |  200 µm | 0.02 |
| 0.13 (–8) |  20 µm |  200 µm | 0.87 |

the boundaries of the melt pools produced by the SLM process were changed.

In the calculation, the Microsoft Office software, Excel module was used.

**Results of investigations**. On the example of high-temperature Inconel 718 alloy, investigations of the influence of power and printing speed on the geometric dimensions of the melt pool of a single track were carried out [21].

According to the results of the experiment, the modes were established, that provide the formation of the melt pool of optimal geometry: the depth of the melting zone should exceed the thickness of the layer by about one and a half to two times, the ratio of the depth to the track width should be from 1.0 to 1.5.

As is seen from Figure 3, at an increase of power by more than 200–230 W the width of a single track ceases its monotonical growth (Figure 3, *a*), at the same time the depth of a track at an increase of power by more than 200–230 W for lower scanning speeds begins to increase sharply (Figure 3, *b*). This, in turn, results in a change in the ratio of the depth of a single track to its width (Figure 3, *c*), i.e. the process goes beyond the rational modes of the working window.

If the scanning pitch is too small, although the continuity of the material between adjacent tracks will be increased and the pore formation will be smaller, the secondary remelting increases the tendency before the formation of a coarse-grained structure. If the scanning pitch is too large, the overlap between two tracks will be insufficient and there will be no connection between the adjacent tracks. This generates a large number of pores, thereby reducing the density (Figure 4). However, an increase in the interval between the passes of the beam increases the remelting area, thereby increasing the utilization factor of the laser and the speed of production.

For further investigations of the influence of the value of a track overlap, one of the modes was chosen, which according to the results of previous investigations was defined as rational: $P = 180$ W, $V = 800$ mm/s. The width of the pool of a single track at such process parameters is 120 μm. Within the frame of the experiment the samples of 10×10×5 mm were produced, for which the distance between the passes of the laser beam was changed from 90 to 130 μm, which should provide an overlap from 25 to 0 % and the absence of overlap is possible if the distance between the tracks exceeds the track width.

As a result of metallographic examinations, it was established (Table 2) that at an overlap of 25 % the conditions of deep penetration are created, and as a result of collapsing a hole (so-called keyhole), large extended pores in a track root are formed.
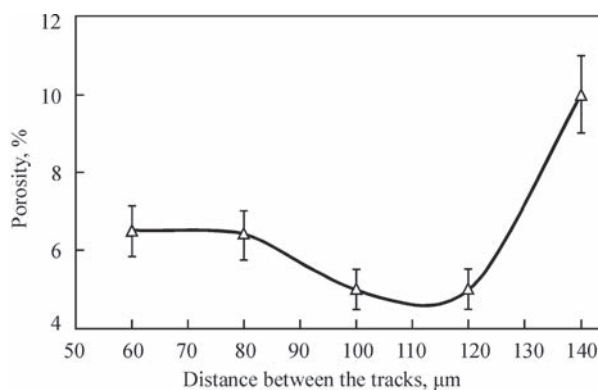


**Figure 4.** Influence of distance between the tracks on the porosity of Inconel 625 alloy [21]

At an overlap of 17 % a small number of tiny rounded pores is formed, the formation of which is probably associated with the capture of gas by the melt metal during crystallization, at an overlap of 0–8 % a structure with a minimum number of pores is formed. When the distance between the tracks exceeds the width of a single track at a given combination of power and laser scanning speed, the cases of a partial fusion of adjacent tracks are observed, the pores with sharp edges are formed, which are stress concentrators and the most dangerous in terms of product reliability. Thus, the optimal overlap of the tracks in selective laser melting was established, which ranges from 0 to 8 % of the width of a single track for specific process parameters.

## Conclusions

The influence of SLM-technology parameters on the quality of final products is shown and the analysis of the influence of technology factors on the quality of finished products was performed.

The rational interval of values of tracks overlap at selective laser melting was established, which amounts from 0 to 8 % of the width of a single track at specific parameters of the process, that provides the minimum porosity of volumetric samples.

1. Kruth, J.-P., Leu, M.-C., Nakagawa, T. (1998) Progress in additive manufacturing and rapid prototyping. *CIRP Ann.-Manuf. Technol.*, 47(**2**), 525–540.
2. Adzhamskij, S.V., Kononenko, A.A., Podolskij, R.V. (2020) Simulation of effect of residual stresses and parameters of SLM technology on formation of boundary product areas from high-temperature nickel alloy Inconel 718. In: *Proc. of Int. Sci.- and Techn. Conf. on Information Technologies in Metallurgy and Machine Building (Ukraine, Dnipro, 17–19 March)*, 4–6. DOI: 10.34185/1991–7848.itmm.2020.01.00.
3. Mahoney, M.W. (1989) Superplastic properties of alloy 718. Ed. by E.A. Loria). *Superalloy 718 Metallurgy and applications*. TMS, 391–405.
4. Adzhamskij, S.V., Kononenko, A.A., Podolskij, R.V. (2020) 2D modeling of nonstationary temperature field of unit track from high-temperature nickel alloy Inconel 718. In: *Proc. of All-Ukrainian Sci.-Method. Conf. on Problems of Mathemat-*

*ical Modeling*, **1**, 42–45 [in Ukrainian]. https://www.dstu.dp.ua/uni/downloads/material_konf_traven_%202020.pdf

5. Shifeng, W., Shuai, L., Qingsong, W. et al. (2014) Effect of molten pool boundaries on the mechanical properties of selective laser melting parts. *J. Mater. Process. Technol.*, 214(**11**), 2660–2667, DOI: https://doi.org/10.1016/j.jmatprotec.2014.06.002

6. Loh, L.-E., Chua, C.-K., Yeong, W.-Y. et al. (2015) Numerical investigation and an effective modelling on the selective laser melting (SLM) process with aluminium alloy 6061. *Int. J. Heat Mass Transf.*, **80**, Jan., 288–300, DOI: https://doi.org/10.1016/j.ijheatmasstransfer.2014.09.014

7. Jia, Q., Gu, D. (2014) Selective laser melting additive manufacturing of Inconel 718 superalloy parts: Densification, microstructure and properties. *J. Alloys Compd.*, **585**, Feb., 713–721. DOI: https://doi.org/10.1016/j.jallcom.2013.09.171.

8. Campanelli, S. L., Contuzzi, N., Angelastro, A.et al. (2010) Capabilities and performances of the selective laser melting process. *New Trends in Technologies: Devices, Computer, Communication and Industrial Systems*, Nov., 233–252.

9. Williams, C.B., Mistree F., Rosen D. W. (2005) Towards the design of a layer-based additive manufacturing process for the realization of metal parts of designed mesostructured. In: *Proc. 16th Solid Free. Fabr. Symp.*, 217–230.

10. Adzhamskij, S.V., Kononenko, A.A., Podolskij, R.V. (2020) SLM technologies in parts and assemblies of aerospace purpose. *In: Proc. of 11th All-Ukrainian Conf. of Young Scientists-2020*, **1**, 6–9 [in Russian].

11. Adzhamskij, S.V., Kononenko, A.A., Podolskij, R.V. (2020) Study of modes of SLM process on quality in field of product contour. In: *Proc. of Int. Conf. on University's Science 2020*, **1**, 157–158. http://eir.pstu.edu/bitstream/handle/123456789/17421/%D0 %A3_%D0 %BA%D0 %B0 %D1 %8F%20 %D0 %BD%D0 %B0 %D1 %83 %D0 %BA%D0 %B0_2020_%D0 %A2_1.pdf

12. Adzhamskij, S.V., Kononenko, A.A., Podolskij, R.V. (2020) Development of technology of product manufacturing for aerospace engineering by selective laser melting method. In: *Proc. of 12th Int. Sci.-Techn. Conf. on New Materials and Technologies in Mechanical Engineering*. https://foundry.kpi.ua/wp-content/uploads/2020/06/conferenziya_2020.pdf#page=29

13. Adzhamskii, S.V., Kononenko, A.A. (2019) Investigation of deep penetration conditions when making samples from high-temperature alloy Inconel 718 by the method of selective laser melting. *The Paton Welding J.*, **6**, 54–58.

14. Adzhamskij, S.V. (2019) Realization of SLM technology for producing of samples from high-temperature nickel alloy Inconel 718, used in aerospace engineering. *Aviats.-Kosmich. Tekhnika i Tekhnologiya*, **2**, 154 [in Russian]. doi: 10.32620/aktt.2019.2.09

15. Dilip, J.J.S, Zhang, S., Teng, C. et al. (2017) Influence of processing parameters on the evolution of melt pool, porosity, and microstructures in Ti–6Al–4V alloy parts fabricated by selective laser melting. *Progress in Additive Manufacturing*, **2**, 157–167.

16. Gu, H., Gong, H., Pal, D. et al (2013) Influences of energy density on porosity and microstructure of selective laser melted 17–4PH stainless steel. *Google Scholar*.

17. Kasperovich, G., Haubrich, J., Gussone, J., Requena, G. (2016) Correlation between porosity and processing parameters in Ti–6Al–4V produced by selective laser melting. *Materials & Design*, **105**, May, 160–170 DOI: https://doi.org/10.1016/j.matdes.2016.05.070

18. Pupoa, Y., Delgadoa, J., Serenóa, L., Ciuranaa, J. (2013) Scanning space analysis in selective laser melting for Co–CrMo powder. *Procedia Engineering*, **63**, 370–378. DOI:10.1016/j.proeng.2013.08.228.

19. Zhichao, Dong, Yabo, Liu, Weibin, Wen et al. (2019) Effect of hatch spacing on melt pool and as-built quality during selective laser melting of stainless steel: Modeling and experimental approaches. *Materials*, 12(**1**), 50. DOI: 10.3390/ma12010050

20. Yadroitsev, I. et. al. (2007) Strategy of manufacturing components with designed internal structure by selective laser melting of metallic powder. *Applied Surface Sci.*, 254(**4**), 980–983. DOI: https://doi.org/10.1016/j.apsusc.2007.08.046.

21. Adzhamsky, S.V., Kononenko, G.A. (2020) Regulanities of influence of SLM process parameters on the formation of single layer from the high-temperature nickel alloy Inconel 718. *The Paton Welding J.*, **1**, 32–38.

# DEVELOPMENT OF TECHNOLOGIES AND MATERIALS FOR ELECTROSPARK COATING WITH THE AIM OF INCREASING THE SERVICE LIFE AND RELIABILITY OF PARTS OF TECHNOLOGICAL AND POWER EQUIPMENT AND TOOLS

**M.S. Storozhenko, O.P. Umansky, V.E. Sheludko, Yu.V. Gubin** and **T.V. Kurinna**

Frantsevich Institute for Problems of Materials Science of the NAS of Ukraine
3 Krzhyzhanovsky Str., 03150, Kyiv, Ukraine. E-mail:storozhenko@ukr.net

It was established that the technology of electrospark alloying is a promising method of strengthening and restoration of parts of technological and power equipment: shafts of pumps and electric motors, impellers, pump casings, centrifuges, etc. To increase the efficiency of the proposed technology, a number of electrode materials were created, such as $FeNiSi–Cr_3C_5$, $WC–TiC–Mo_2C–Co–Cr$ and WC–TiC–Co–Cr–Ni–Al, TiC–(Fe–Cr–Si–Al), NiCrBCuC–WC, $FeNiCrBSiC–TiB_2$ and $FeNiCrBSiC–CrB_2$, which were tested at industrial enterprises of Ukraine. It was revealed that application of the developed electrodes provides a simultaneous increase in the manufacturability of the process of electrospark alloying with an extension of the life of parts of technological equipment by 2.0–2.5 times. 10 Ref., 4 Figures.

*K e y w o r d s : electrospark hardening, coating, wear resistance, self-fluxing alloy, titanium diboride*

Wearing of friction unit parts is one of the main reasons of reduction of operating life of machines and mechanisms. Up to 85 % of defects and damage of machines and production equipment are caused by intensive wear of the surface layer of parts, which is the most exposed to the environment and contact loads at friction [1]. Premature failure of machines and mechanisms as a result of wear can lead to major man-made disasters in a number of cases. For instance, erosion-corrosion wear of technological equipment of the main pipelines and enterprises of petroleum-processing industry results in large-scale leakages of petroleum products that pose a threat to human life and health [2]. Therefore, increase of the reliability and fatigue life of parts of machines and mechanisms is an urgent scientific task, whose solution is inextricably linked with increase of wear resistance of working surfaces of critical parts of machines and mechanisms.

Project P8.1 «Development of technologies and materials for electrospark coating deposition with the aim of increasing the service life and reliability of parts of technological and power equipment and tools» that was fulfilled during 2016–2020 within the target integrated research program «Reliability and fatigue life of materials, structures, equipment and constructions» (Resurs-2) of the NAS of Ukraine, aimed at extending the operating life of parts of production equipment and tools by restoration/improvement of wear resistance of their working surfaces by the method of electrospark alloying (ESA). The method has the following main advantages: possibility of local application of coatings from any current-conducting materials; high strength of adhesion of the alloyed layer with the base material; simplicity of conducting the process; its low power consumption and low equipment cost. The disadvantages of this method are its relatively low productivity, which can be increased by applying new electrode materials and modern technological equipment.

Pure metals (Mo, Cr), metal alloys (Fe–Cr, Fe–C, Ni–Cr, Ni–Mo), graphite (EG-2, EG-4) and hard alloys (WC–Co and WC–TiC–Co) are traditionally used for ESA [3]. When using electrodes from pure metals and metal alloys, it is not possible to produce coatings with the required high service properties. Therefore, electrospark coatings from hard alloys based on tungsten carbide are the most widely used for wear-resistant coating deposition in the industrial enterprises. They, however, do not always meet the requirements of manufacturability of ESA coatings in view of their high erosion resistance and low mass-transfer coefficient, respectively, and because of tungsten deficit it becomes necessary to develop tungsten-free ESA coatings. Therefore, at present development of the technology of electrospark coating deposition is related to development of tungsten-free composite electrode materials of «refractory compound–metal alloy system» [4].

Frantsevich Institute for Problems of Material Science (IPMS) developed a number of electrode
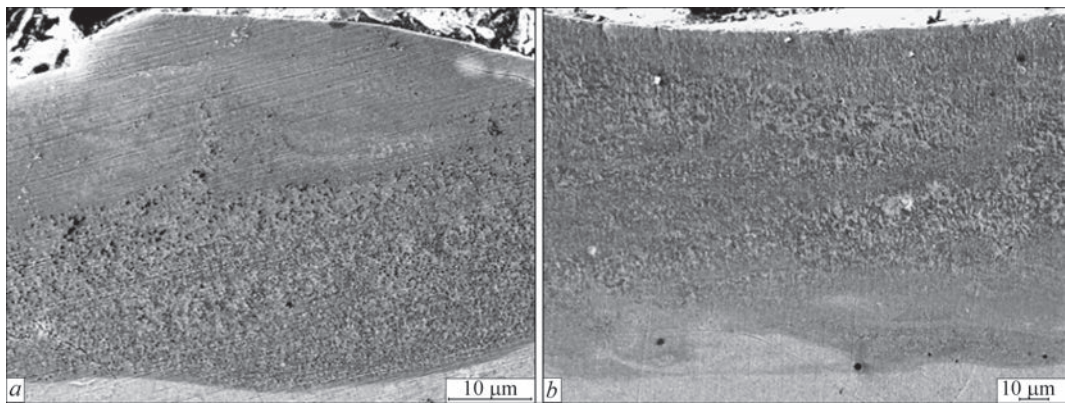
**Figure 1.** Structure of ESA coatings from developed FTB20 (*a*) and FCB20 (*b*) electrodes

composite materials based on carbides/borides of titanium, molybdenum, chromium and tungsten and batch-produced self-fluxing alloys: FeNiSi–Cr$_3$C$_2$, WC–TiC–Mo$_2$C–Co–Cr and WC–TiC–Co–Cr–Ni–Al, TiC–(Fe–Cr–Si–Al), NiCrBCuC–WC, FeNiCrSiC–TiB$_2$ and Fe–NiCrBSiC–CrB$_2$ [5–10]. Within the framework of project P8.1 investigations of mass transfer kinetics at electrospark alloying of steel 45 were conducted to reveal the optimum compositions of the developed electrodes from the view point of ensuring the adaptability-to-manufacture of the processes of electrospark strengthening/restoration of working surfaces of parts. Features of formation of the structure and relief of the surface of ESA coatings from the developed electrode materials were studied, depending on the ratio of the refractory and metal components of the electrodes, and their wear resistance was determined under the conditions of dry sliding friction and abrasive wear.

It was established, in particular, that ESA coatings based on batch-produced self-fluxing FeNiCrBSiC alloy with additives of 20 % TiB$_2$ (FTB20) and 20 % CrB$_2$ (FCB20) are formed by melting the electrode metal component with simultaneous breaking and fragmentation of inclusions of borides and carboborides of chromium with subsequent precipitation of

electrode particles and their transfer to the surface of the cathode (steel), where they are welded to the surface as a result of micrometallurgical processes. Here, there is no mixing of the material of the electrode and the steel substrate. Nanostructured ESA coatings form on the steel surface as a result of refinement of titanium/chromium borides and carboborides from 20–30 μm to dimensions smaller than 1 μm (Figure 1). Surface of ESA coatings from FeNiCrBSiC–20 % TiB$_2$ and FeNiCrBSiC–20 % CrB$_2$ has a uniform relief over the entire surface of the samples. Under the conditions unlubricated sliding friction, ESA-coatings from developed electrode materials FTB20 and FCB20 have 2–3 times higher wear resistance, compared to coatings from batch-produced WC–6 % Co electrodes (Figure 2) [10].

Results of the work were used to develop TUU 25.9-05416930-049-014:2019 specification «FeNiCrSiC–TiB$_2$ electrodes for electrospark strengthening of parts for tribotechnical applications». Experimental production trials at UC «Kyiv Metropoliten» showed that deposition of electrospark coatings from the developed electrospark material FTB20 on working surfaces of gear–shaft L-20877A of LT-2 type escalator provides 2.0–2.5 times extension of its operating life (150–160 thou km) (Test report of 12.04.2019).
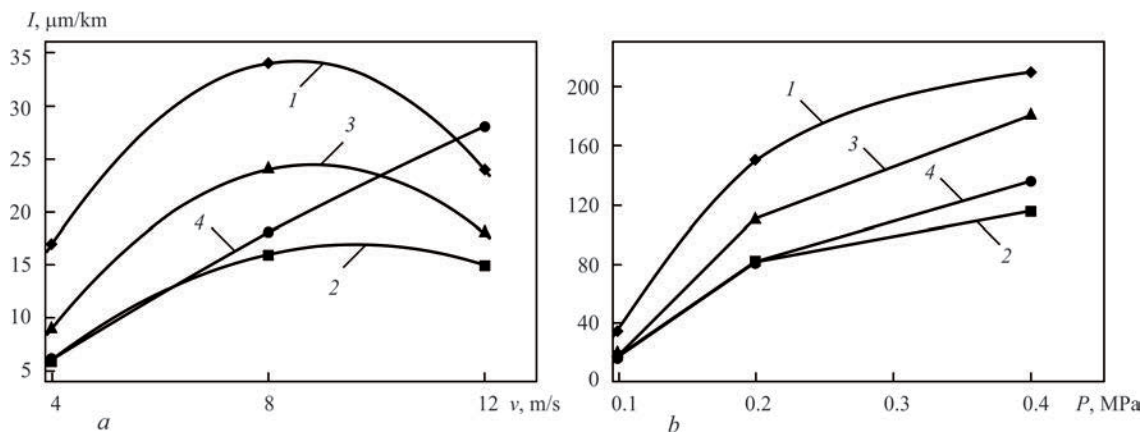


**Figure 2.** Dependence of wearing intensity of ESA coatings: FeNiCrBSiC (*1*), FRB20 (*2*), FCB20 (*3*) and WC–6 % Co (*4*) on speed (*a*) and load (*b*)
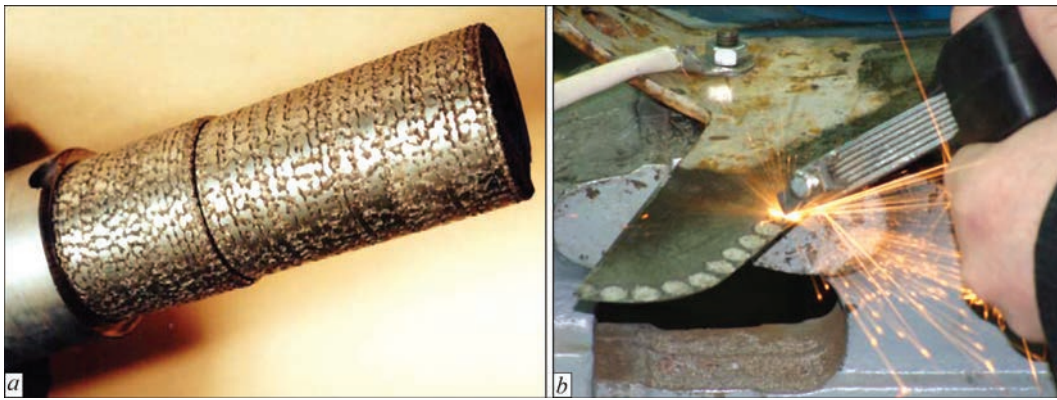
**Figure 3.** Part strengthening by ESA method with application of the developed electrodes: journal of electric motor rotor from half-coupling side (*a*) and plough share (*b*)

Experimental production trials at «TRIZ» enterprise showed that deposition of ESA-coatings from the developed FKhTB20 composite material on working surfaces of end seals of TsBS-30.50.01.200 grade for STsL-20-24 fuel pumps by electrodes from FTB20 composite material of FeNiCrBSiC–TiB system (ALIER52 unit: pulse duration of 170 μs; amplitude value of pulse current of 200 A; pulse energy of 0.6 J) ensures 2.0–2.5 times extension of seal assembly operating life.

Process of electrospark hardening and restoration of parts of technological equipment and tools using developed electrode materials NiBCuSi–WC, FeNi-Si–$Cr_3C_5$, WC–TiC–$Mo_2$C–Co–Cr and WC–TiC–Co–Cr–Ni–Al, TiC–(Fe–Cr–Si–Al) was applied in the enterprises of «TRIZ» (Sumy) and JSC «SPC Elektromash» (Sumy). Analysis of damaged parts in these enterprises showed that the most widely spread kinds of wear include cavities on the surface of blades of centrifugal compressor impellers, corrosive-abrasive wear of bearing journals of the rotor shaft of TsNS-180 pump and electric motor rotors. Parts of these units are made from high-strength steels, their working surfaces are strengthened by different kinds of chemicothermal treatment. However, these parts operate under the conditions of dry friction at specific loads of up to 20 MPa that leads to their intensive wear. Electrospark hardening of large-sized parts (electric motors, impellers, casing pumps, centrifuges) using the developed electrodes allowed increasing their wear resistance and operating life 2.0–2.5 times. In particular, electrospark treatment of shaft working surfaces (Figure 3, *a*) by FeNiSi–$Cr_3$C electrodes in EIL-8A unit allowed increasing the maximum thickness of ESA coatings compared to application of WC–6 % Co (VK6) electrodes from 0.2 to 1.6 mm. NiBCuSi-WC electrode material was used at SPE «Elektromash» (Sumy) for local hardening and restoration in «Elitron-22A» and «Elitron-52A» units the plough shares (Figure 3, *b*) and seats of industrial fans with considerable local damage and wear of the surface.

In addition, «TRIZ» enterprise developed a number of technological processes for strengthening compressor parts using graphite as ESA electrode. Sealing assembly is one of the most critical components ensuring the compressor unit tightness, its safe and no-failure operation. Two thirds of all the compressor failures are the result of violation of the seal performance. Therefore, a technology was developed within the framework of project P8.1 for strengthening the heat-treated collars from 38Kh2MYuA steel by electrospark treatment by graphite, after their fitting on
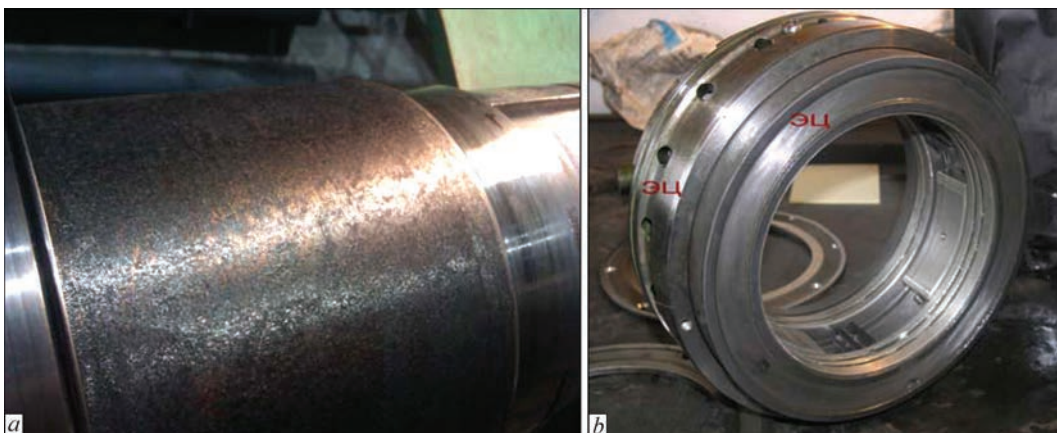


**Figure 4.** Appearance of the protective collar of the seal assembly after ESA (*a*) and floating seal ring of a centrifugal compressor (*b*)

the shaft. Contact end surfaces of floating ring seals and respective parts of the casing and cover (Figure 4) were hardened in a similar way. The process of electrospark treatment was conducted in «Elitron-22A» unit at discharge energy of 0.5 J; the depth of the strengthened layer was 30–50 μm, microhardness was *HV* 900–1100. After that, alloying of the contact surfaces by silver at discharge energy of 0.05 J was conducted, in order to lower the roughness and coefficient of friction.

EILV-8 unit was used to make a mock-up of a mechanized unit (EILV-8M) for strengthening the rotation parts. In keeping with the recommendations of the staff of IPMS «TRIZ» enterprise manufactured the fixture for mechanization of ESA process of small-sized cylindrical parts (parts of fuel pumps, compressor impellers and shaft journals of electric motor rotor), that resulted in a significant increase of productivity.

Thus, application of the proposed under the project technological solutions and developed electrodes allows increasing the adaptability-to-manufacture of the process of electrospark alloying, lowering the labour consumption and increasing the operating life of parts of power and technological equipment by 2.0–2.5 times. Developed electrospark coatings have passed trials at industrial enterprises of Ukraine (OJSC «TRIZ» (Sumy), SPE «Elektromash» (Sumy), CE Kyiv Metropoliten) that is confirmed by positive reports of experimental-production trials.

1. Holmberg, K., Matthews, A. (2009) *Coatings tribology: Properties, mechanisms, techniques and application in surface engineering.* Switzerland, Elsevier.
2. Wu, X. (2004) Erosion-corrosion of various oil-refining materials in naphthenic acid. *Wear*, **256**, 133–144.
3. Verkhoturov, A.D., Podchernyaeva, I.A., Pryadko, L.F., Egorov, F.F. (1988) *Electrode materials for electrospark alloying.* Moscow, Nauka [in Russian].
4. Bovkun, G.A., Tkachenko, Yu.G., Yurchenko, D.Z. (1983) Tungsten-free electrode materials for electrospark alloying of metallic surfaces. *Elektrofiz. Obrabotka Materialov*, **5**, 27–29 [in Russian].
5. Tarelnik, V.B., Paustovsky, A.V., Tkachenko, Yu.G. et al. (2016) Electrode materials, composite and multilayer electrospark coatings from alloys of Ni–Cr, WC–Co systems and metals. *Poroshk. Metallurgiya*, **9–10**, 100–115 [in Russian].
6. Paustovsky, A.V., Tkachenko, Yu.G., Khristov, V.G. et al. (2016) Materials for the electrospark strengthening and reconditioning of worn metal surfaces. *Surface Engineering and Applied Electrochemistry*, **1,** 14–22.
7. Tarelnik, V.B., Paustovsky, A.V., Tkachenko, Yu.G. (2017) Electrospark coatings on steel base and contact surface for optimization of service characteristics of whitemetal sliding bearings. *Electron. Obrabotka Materialov*, **1**, 37–46 [in Russian].
8. Tarelnik, V.B., Paustovsky, A.V., Tkachenko, Yu.G. et al. (2017) Electrospark alloying of steel surfaces by graphite: Technology, properties, application. *Ibid.*, **4**, 1–10 [in Russian].
9. Tkachenko, Yu.G., Yurchenko, D.Z., Timofeeva, I.I., Britun, V.F. (2018) Effect of composition of electrodes from alloys of TiC–(FeCr–Al–Si) system on formation, phase composition and properties of wear- and heat-resistant electrospark coatings on steel. *Poroshk. Metallurgiya*, **7–8**, 119–129 [in Russian].
10. Umansky, O.P., Storozhenko, M.S., Tarelnik, V.B. et al. (2020) Peculiarities of formation of electrospark coatings of $NiFeCrBSiC–MeB_2$ on steel. *Ibid.*, **1–2**, 86–95 [in Ukrainian].

INDIA ESSEN WELDING & CUTTING
9th International Trade Fair
Joining - Cutting - Surfacing
25–27 March, 2021
Bombay Convention & Exhibition Centre
Goregaon (East), Mumbai, India

# INFLUENCE OF AMPLITUDE AND FREQUENCY OF OSCILLATIONS OF ELECTRODE WIRE IN ARC SURFACING ON FORMATION AND STRUCTURE OF THE DEPOSITED METAL AND PENETRATION OF BASE METAL

**A.A. Babinets, I.O. Ryabtsev, I.P. Lentyugov, I.I. Ryabtsev, T.V. Kaida** and **I.I. Bogaichuk**

E.O. Paton Electric Welding Institute of the NAS of Ukraine
11 Kazymyr Malevych Str., 03150, Kyiv, Ukraine. E-mail: office@paton.kiev.ua

The influence of amplitude and frequency of oscillations of electrode wire during arc surfacing on formation of deposited beads, nature of base metal penetration, as well as structural and chemical heterogeneity in the zone of the joint of deposited and base metals were studied. It was established that an increase in the frequency of oscillations of electrode wire, at the same amplitude of oscillations and rate of deposition, leads to an improvement in formation of the deposited metal and mixing of the layers in the deposited metal; formation of a more dispersed structure; narrowing of the transition zone; more uniform distribution of alloying elements; more uniform penetration and «smoothing» of the fusion boundary of the deposited and base metal. The mentioned regularities almost do not change with an increase in the amplitude of oscillations. It was established that the best formation of the deposited metal occurs at the maximum frequency $N = 45$ min$^{-1}$ and amplitude of oscillations of the electrode wire $A = 25$ mm and deposition rate $V_d = 7$ m/h. 8 Ref., 2 Tables, 10 Figures.

*K e y w o r d s :  arc surfacing, electrode wire oscillation, amplitude and frequency of oscillations, base metal penetration, deposited metal formation, deposited metal structure, structure heterogeneity*

Large penetration of base metal is one of the disadvantages of arc surfacing. In order to reduce base metal penetration and obtain wide and relatively low beads, it is proposed to perform arc surfacing with oscillations of electrode wire or strip [1–6]. In these works, the conclusions on the positive impact of oscillations of electrode wire or strip on the extent and nature of base metal penetration were evaluated, mainly, on transverse sections of the deposited beads, and the impact of electrode wire oscillation on structural heterogeneity of the deposited metal was not studied, either.

However, considering the fact of direct impact of the arc on base metal during transverse oscillations of electrode wire and its displacement in the longitudinal direction, it is to be anticipated that the nature of penetration in the longitudinal and transverse sections of the deposited beads can change. This fact should be taken into account at development of the technologies of deposition of parts, operating not only under the conditions of different kinds of wear, but also cyclic loading, as nonuniform penetration can lead to lowering of their wear resistance, as well as fatigue life at cyclic mechanical and thermal loads [7, 8].

Analysis shows that in this case, if we ignore the electric parameters of the surfacing mode, the main effect on base metal penetration, formation and structure of the deposited beads is produced by amplitude and frequency of oscillations of electrode wire or strip, as well as the deposition rate. These three characteristics are interconnected, and at the change of one of them, the others should be adjusted, in order to obtain sound deposited beads.

Thus, the objective of the experiments was studying the impact of the frequency and amplitude of oscillations of electrode wire at arc surfacing, as well as the deposition rate on base metal formation, depth and nature of base metal penetration, its fraction in the deposited metal and on the deposited metal structure. Investigations were conducted on longitudinal and transverse sections of the deposited beads.

Flux-cored wire of PP-Np-30Kh20MN type of 2.6 mm diameter was used as the model material. Surfacing was performed using AN-26P flux. Surfacing modes were as follows: current of 280–320 A; voltage of 30–32 V; deposition rate of 7 and 10 m/h; oscillation frequency, $N$ of 18; 28; 32 and 45 min$^{-1}$; os-

A.A. Babinets — https://orsid.org/0000-0003-4432-8879, I.O. Ryabtsev — https://orsid.org/0000-0001-7180-7782,
I.P. Lentyugov — https://orsid.org/0000-0001-8474-6819, I.I. Ryabtsev — https://orsid.org/0000-0001-7550-1887
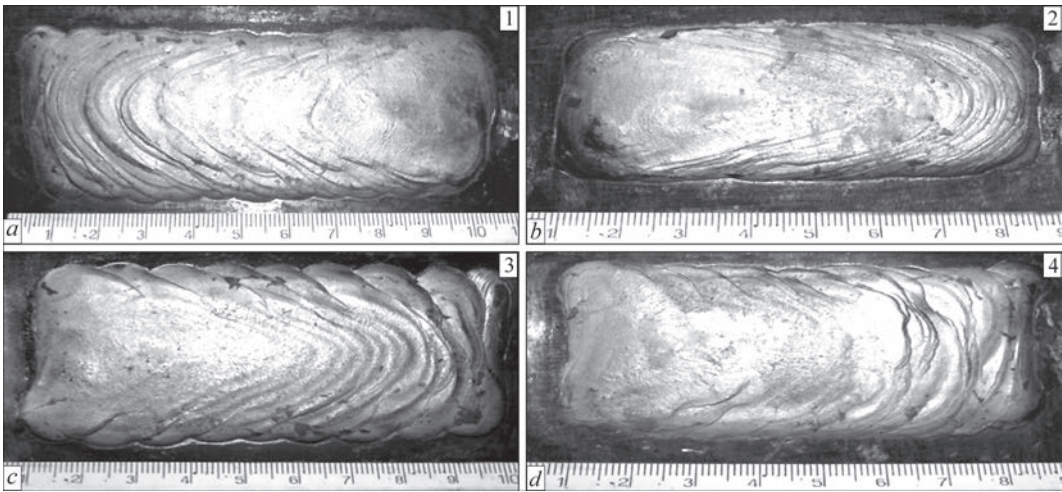
**Figure 1.** Appearance of beads, deposited at rate $V_d$ = 7 m/h; $a$ — sample 1: $A$ = 25 mm; $N$ = 28 min$^{-1}$; $b$ — sample 2: $A$ = 25 mm; $N$ = 45 min$^{-1}$; $c$ — sample 3: $A$ = 40 mm; $N$ = 18 min$^{-1}$; $d$ — sample 4: $A$ = 40 mm; $N$ = 32 min$^{-1}$ (for sample numbers see Table 1)
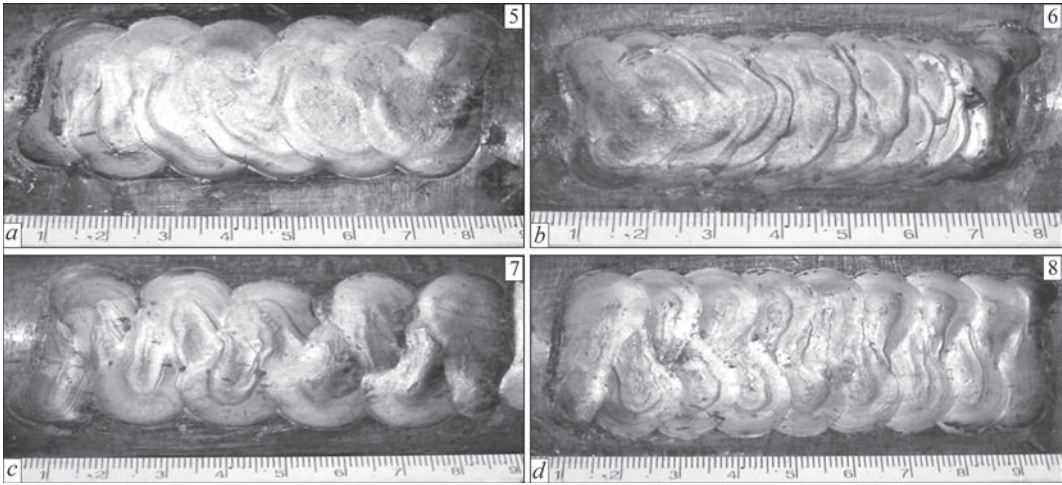


**Figure 2.** Appearance of beads, deposited at rate $V_d$ = 10 m/h; $a$ — sample 5; $A$ = 25 mm; $N$ = 28 min$^{-1}$; $b$ — sample 6: $A$ = 25 mm; $N$ = 45 min$^{-1}$; $c$ — sample 7: $A$ = 40 mm; $N$ = 18 min$^{-1}$; $d$ — sample 8: $A$ = 40 mm; $N$ = 32 min$^{-1}$ (for sample numbers see Table 1)

cillation amplitude, $A$ — 25 and 40 mm. Altogether, 8 samples were deposited for investigations.

The beginning and crater part were cut off the deposited beads (Figures 1, 2). Longitudinal and transverse macrosections were cut out of the remaining material, in order to determine the size of the beads, base metal penetration and its proportion in the deposited metal $\gamma_O$ (PBM) (Table 1), as well as for studying the macro- and microstructure of the deposited beads.

$$\gamma_0 = \frac{F_b}{F_b + F_d} \cdot 100\,\%,$$

where $F_b$ and $F_d$ are the cross-sectional areas of the base and deposited metals, respectively.

**Table 1.** Influence of deposition mode on geometrical parameters of the beads

| Sample number | Oscillation | | Deposition rate, m/h | Bead dimensions, mm | | | PBM, % |
|---|---|---|---|---|---|---|---|
| | Amplitude $A$, mm | Frequency $N$, min$^{-1}$ | | Width | Height | Penetration depth | |
| 1 | 25 | 28 | 7 | 38.8 | 3.4 | 1.7 | 39 |
| 2* | 25 | 45 | 7 | 36.4 | 2.95 | 1.6 | 37 |
| 3 | 40 | 18 | 7 | 46.8 | 2.05 | 1.8 | 54 |
| 4 | 40 | 32 | 7 | 47.0 | 1.8 | 1.5 | 50 |
| 5 | 25 | 28 | 10 | 37.5 | 1.9 | 1.8 | 55 |
| 6 | 25 | 45 | 10 | 35.8 | 2.7 | 1.5 | 52 |
| 7 | 40 | 18 | 10 | 42.6 | 2.1 | 1.5 | 50 |
| 8 | 40 | 32 | 10 | 44.7 | 1.5 | 1.4 | 49 |

*Sample, deposited in the mode providing the optimum result.

**Figure 3.** Transverse (*a, b, e, f*) and longitudinal (*c, d, g, h*) macrosections of samples, deposited at the rate of 7 m/h: *a, c* — sample 1: $A = 25$ mm; $N = 28$ min$^{-1}$; *b, d* — sample 2: $A = 25$ mm; $N = 45$ min$^{-1}$; *e, g* — sample 3: $A = 40$ mm; $N = 18$ min$^{-1}$; *f, h* — sample 4: $A = 40$ mm; $N = 32$ min$^{-1}$ (for sample numbers see Table 1)
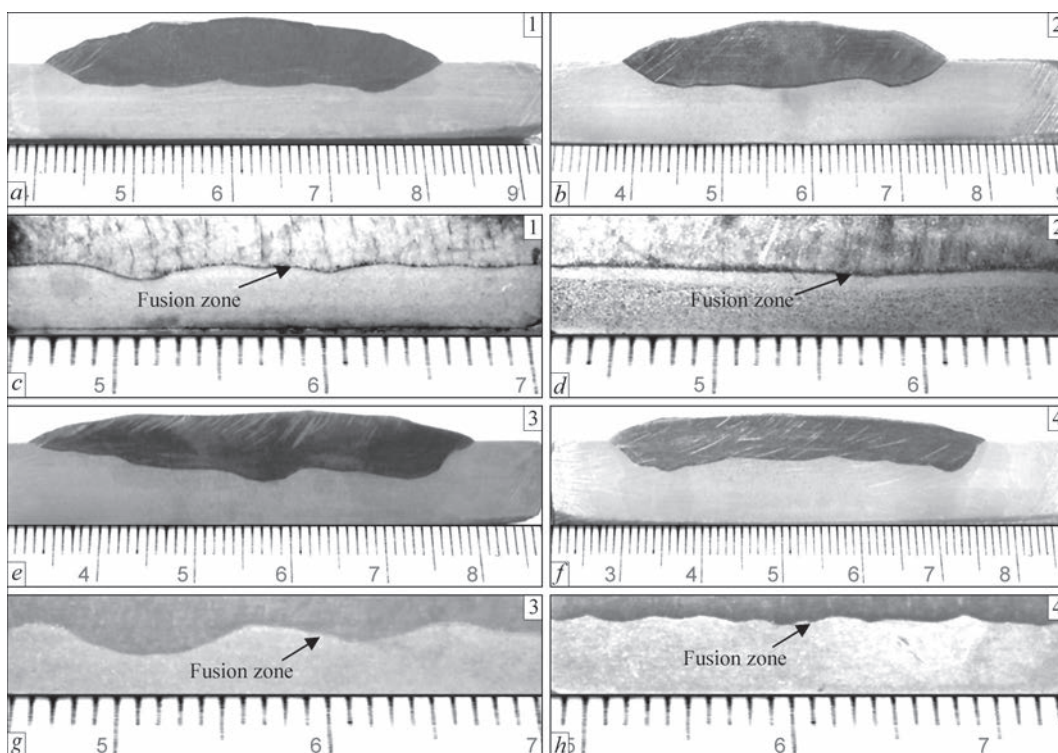
Minimum PBM on the level of 37–39 % was found in samples Nos 1 and 2, penetration depth was 1.6–1.7 mm. Smaller penetration value of 1.4–1.5 mm was noted in samples Nos 7 and 8. However, PBM in these samples is on the level of 49–50 % (Table 1).

Based on aggregate assessment of the deposited bead dimensions, penetration depth and PBM, the following mode was determined to be optimum: deposition rate of 7 m/h; amplitude of electrode wire oscillations $A = 25$ mm, its oscillation frequency $N = 45$ min$^{-1}$ (Table 1, sample 2).

Figure 3, *a, b, e, f* shows the photo of macrosections, cut out across, and Figure 3, *c, d, g, h* — those cut out along the longitudinal axis of the beads, deposited at the rate of 7 m/h. Accordingly, Figure 4, *a, b, e, f* shows the photo of macrosections, cut out across, and Figure 4, *c, d, g, h* — along the longitudinal axis of the beads, deposited at the rate of 10 m/h.

If we analyze the longitudinal macrosections, then at deposition rate of 7 m/h increase of the frequency of electrode wire oscillations promotes producing a more uniform penetration and smoother fusion boundary of the deposited and base metals (Figure 3, *d, h*). Here, the most even fusion boundary is achieved at oscillation amplitude of 25 mm and maximum frequency of 45 min$^{-1}$ (Figure 3, *d*; Table 1, sample 2).

Transverse macrosections of the beads, deposited at the rate of 7 m/h with different oscillation parameters, differ only slightly one from another. It is worth

noting just the macrosection in Figure 3, *f* (sample 4), which is characterized by minimum penetration of 1.5 mm.

At increase of deposition rate up to 10 m/h, a uniform penetration along the deposited beads could not be achieved at any of the frequencies and amplitudes of electrode wire (Figure 4, *c, d, g, h*). Here, at deposition at a higher rate (10 m/h), increase of oscillation frequency of electrode wire also promotes achieving a more uniform penetration and greater «smoothness» of the fusion line (Figure 4, *d, h*). This influence, however, is weaker than at the deposition rate of 7 m/h.

Similar to the rate of 7 m/h, nonuniform penetration is observed also in microsections, cut out across the beads, deposited at the rate of 10 m/h (Figure 4, *b, e, f*, samples 6, 7, 8).

Deposited metal of sample 1 ($V_d = 7$ m/h; $A = 25$ mm; $N = 28$ min$^{-1}$) has a dendritic microstructure (Figure 5, *a*). Cellular solidification prevails in the subsurface layers of the deposited metal, with average cell size of 60–80 μm. Hardness of the matrix base is equal to $HV1 = 5420$–6060 MPa (martensite, residual austenite, carbides). Precipitation of chains of globular-shaped particles occurs along the crystallite boundaries (Figure 5, *b*).

Solidification of deposited metal of sample 2 ($V_d = 7$ m/h; $A = 25$ mm; $n = 45$ min$^{-1}$) is dendritic-cellular with prevalence of the cellular type (Figure 5, *c*), with average cell size of 30–40 μm. Solidification
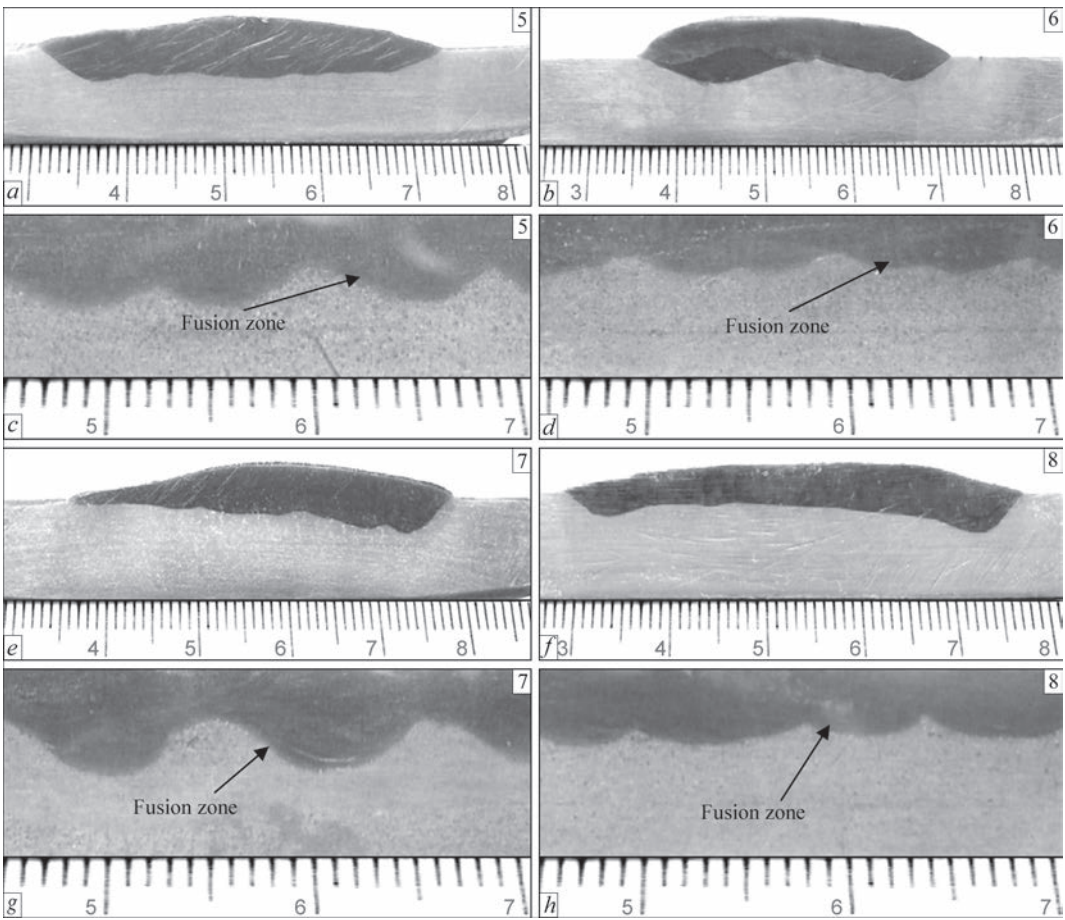
**Figure 4.** Transverse (*a*, *b*, *e*, *f*) and longitudinal (*c*, *d*, *g*, *h*) macrosections of samples, deposited at the rate of 10 m/h: *a*, *c* — sample 5: $A = 25$ mm; $N = 28$ min$^{-1}$; *b*, *d* — sample 6: $A = 25$ mm; $N = 45$ min$^{-1}$; *e*, *g* — sample 7: $A = 40$ mm; $N = 18$ min$^{-1}$; *f*, *h* — sample 8: $A = 40$ mm; $N = 32$ min$^{-1}$ (for sample numbers see Table 1)



**Figure 5.** Microstructure of deposited metal of samples 1 (*a*, *b*) and 2 (*c*, *d*): *a*, *c* — fusion zone, ×20; *b*, *d* — deposited metal, ×100. Electrolytic etching in chromic acid. $U_{o.-c} = 20$ V; $t = 3$–5 s (for sample numbers see Table 1)

**Figure 6.** Microstructure of deposited metal of samples 3 (*a*, *b*) and 4 (*c*, *d*): *a*, *c* — fusion zone, ×20; *b*, *d* — deposited metal, ×100. Electrolytic etching in chromic acid. $U_{o-c}$ = 20 V; $t$ = 3–5 s (for sample numbers see Table 1)

becomes dendritic at the line of fusion with the base metal. The width of crystallites in this region is equal to 70–90 μm. Hardness of the matrix base is $HV$1–4880–5480 MPa. Within the crystallites, similar to sample No.1, excess phase precipitates in the form of globular dispersed particles (Figure 5, *d*). HAZ width is equal to 3600 μm.

Microstructure of deposited metal of sample 3 ($V_d$ = 7 m/h; $A$ = 40 mm; $N$ = 18 min$^{-1}$) is dendritic-cellular with prevalence of the cellular one (Figure 6, *a*, *b*). Average diameter of the cells is 50–60 μm. Hardness of the matrix base is $HV$1–6060–6130 MPa. A martensite ridge is observed at the fusion line from the deposited metal side. In this zone, martensite forms large needles. Crystallite width at the fusion line is 70–80 μm. HAZ width is 2100 μm.

Deposited metal of sample 4 ($V_d$ = 7 m/h; $A$ = 40 mm; $N$ = 32 min$^{-1}$) also has dendritic-cellular structure with the cellular shape prevailing on the surface. Cell diameter is equal to 40–50 μm (Figure 6, *b*, *c*). The structure at the fusion line is dendritic, crystallite width in this region is 60–80 μm. Hardness inside the crystalline base in this sample is lower than that in sample 3 and is equal to $HV$1–5140–5420 MPa. HAZ width is 1800 μm.

Microstructural studies of sample 5 ($V_d$ = 10 m/h; $A$ = 25 mm; $N$ = 28 min$^{-1}$) showed that it has a den-dritic structure (Figure 7, *a*, *b*). Cellular solidification prevails in the subsurface layers of the deposited metal, with average cell diameter of 60–80 μm. Matrix base hardness is $HV$1–6860 MPa. Particles of a globular shape precipitate on the crystallite boundaries. Cell diameter in the upper part of the deposited metal is 15–20 μm; crystallite width $h_{cryst}$ is 15–25 μm, HAZ width is 1200 μm. Intermetallic or carbide precipitates are observed along the crystallites boundaries.

Microstructure of sample 6 ($V_d$ = 10 m/h; $A$ = 25 mm; $N$ = 45 min$^{-1}$) is shown in 7, *c*, *d*. It also has a dendritic structure, with cellular solidification in the subsurface layers. Cell diameter is 25–35 μm; crystallite width $h_{cryst}$ is 25–50 μm, HAZ width is 800–900 μm. Intermetallic or carbide precipitates are present along the boundaries of crystallites and cells. Microhardness is $HV$1–6810 MPa in the light layer and $HV$1–6340 MPa in the dark layer.

Microstructural studies of sample 7 ($V_d$ = 10 m/h; $A$ = 40 mm; $N$ = 18 min$^{-1}$) showed that it has a den-dritic-cellular structure (Figure 8, *a*, *b*). Cell diameter is 40–60 μm; crystallite width $h_{cryst}$ is 40–60 μm, HAZ width is 1000–1200 μm. Microhardness is $HV$1–6420 MPa. There are some precipitates along the crystallite and cell boundaries, but their number is much smaller than in samples 5 and 6, shown in Figure 7.
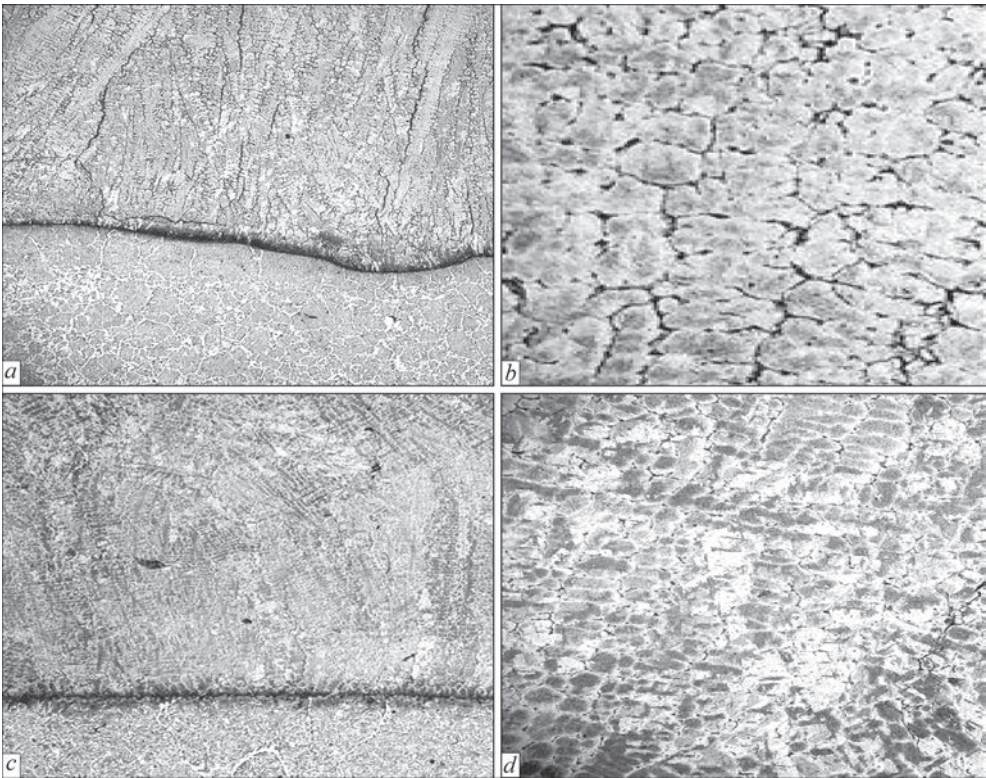
**Figure 7.** Microstructure of deposited metal of samples 5 (*a*, *b*) and 6 (*c*, *d*): *a*, *c* — fusion zone, ×20; *b*, *d* — deposited metal, ×100. Electrolytic etching in chromic acid. $U_{o.-c} = 20$ V; $t = 3–5$ s (for sample numbers see Table 1)
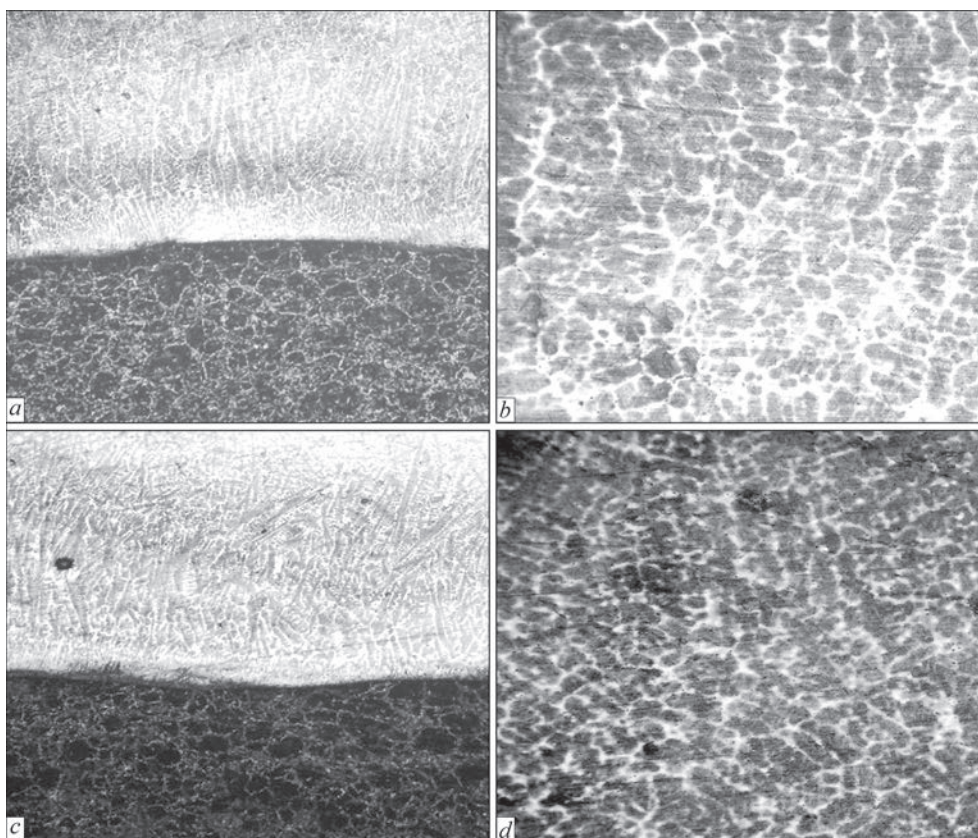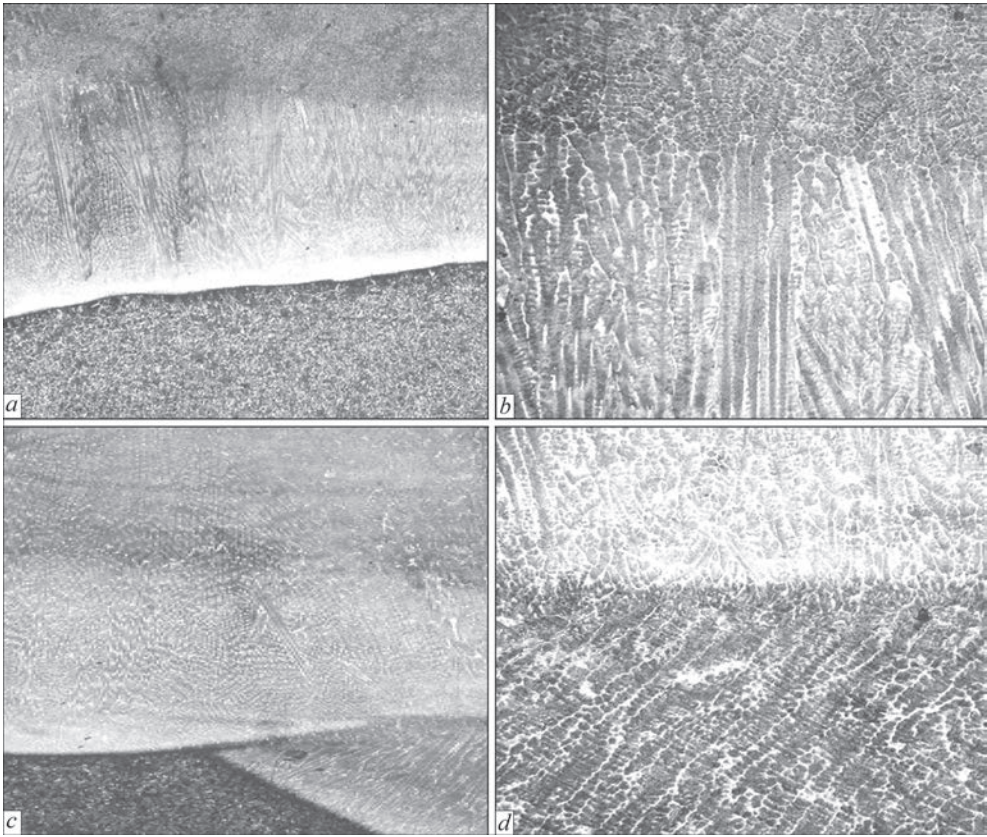


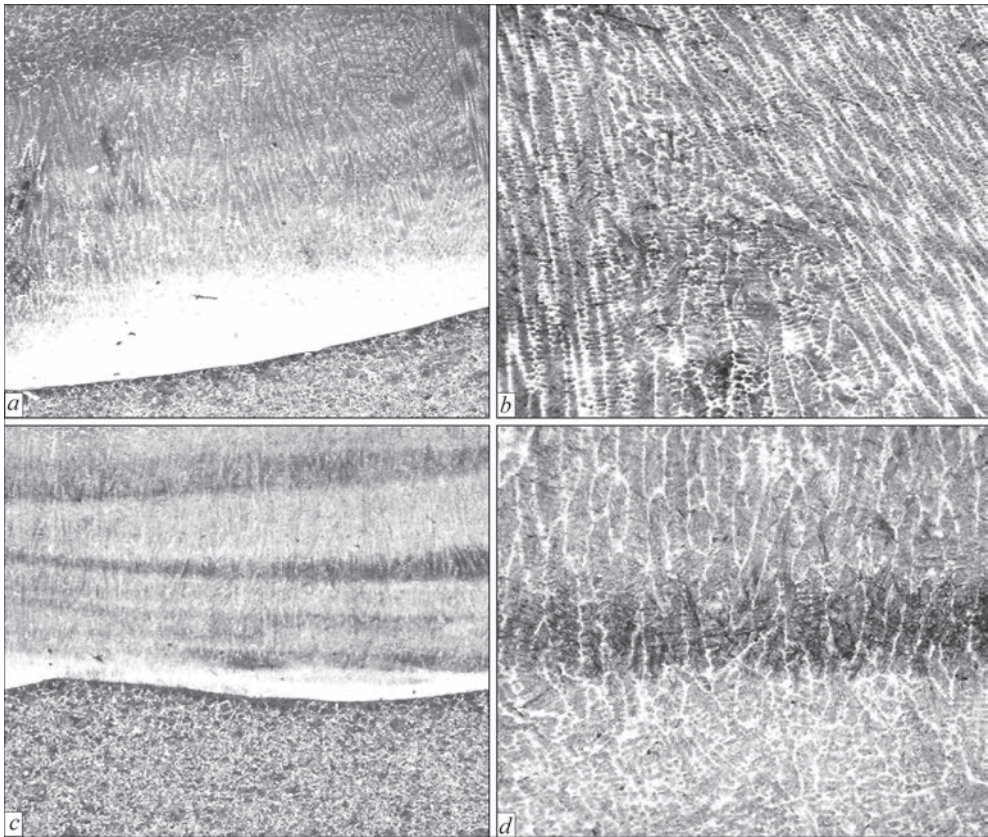**Figure 8.** Microstructure of deposited metal of samples 7 (*a*, *b*) and 8 (*c*, *d*): *a*, *c* — fusion zone, ×20; *b*, *d* — deposited metal, ×100. Electrolytic etching in chromic acid. $U_{o.-c} = 20$ V; $t = 3–5$ s (for sample numbers see Table 1)
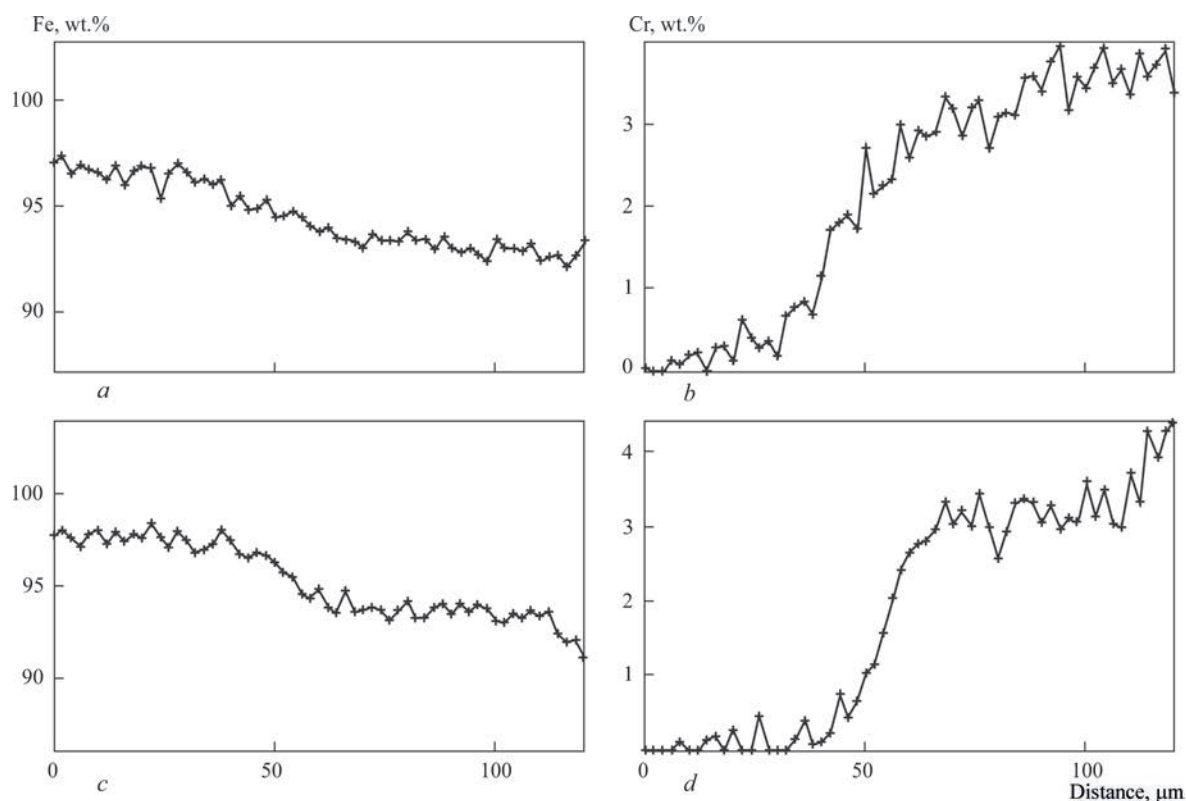
**Figure 9.** Fe (*a, c*) and Cr (*b, d*) distribution in the transition zone of sample 1 (*a, b*) and sample 2 (*c, d*)

Microstructure of deposited metal of sample 8 ($V_d$ = 10 m/h; $A$ = 40 mm; $N$ = 32 min$^{-1}$) is dendritic-cellular (Figure 8, *c, d*). Cell diameter is 15–30 μm, crystallite width $h_{cryst}$ is 30–40 μm, HAZ width is 600–800 μm. Chemical heterogeneity was detected over the entire surface of the deposited metal. There are precipitates along the boundaries of crystallites and cells. Microhardness in the light layer is $HV$1–6060–6130 MPa; in the heterogeneous region $HV$1–4840 MPa.

Methods of X-ray microanalysis, X-ray structure and metallographic analyses were used to study the chemical and structural heterogeneity of the deposited metal. Recording of linear distribution of alloying elements was performed at the distance of 600–700 μm

from the deposited layer surface. Figure 9, *a–d* gives the curves of Fe and Cr distribution in the transition zone of samples 1 and 2 as an example.

Comparative analysis showed that the length of the transition zone becomes smaller at increase of oscillation frequency. So, at oscillation frequency of 28 min$^{-1}$ the width of the transition zone is close to 35–40 μm, and at the frequency of 45 min$^{-1}$ it is 20–25 μm (Table 2, samples 1 and 2). Similar results were obtained at analysis of the deposited bead microstructure in samples 1–8 (see above).

The fusion zone has a smooth concentration transition, and chemical microheterogeneity of the deposited metal is relatively small and is equal for chromium to $Cr_{max}/Cr_{min}$ = 1.20–1.46; for molybdenum — to

**Table 2.** Influence of surfacing mode with wire oscillations on the microstructure and microheterogeneity of the deposited metal of samples 1–8 (see Table 1)

| Sample number | Surfacing modes | | | Parameters of microstructure state | | | Cr and Mo chemical heterogeneity | | | |
|---|---|---|---|---|---|---|---|---|---|---|
| | $V_d$, m/h | $A$, mm | $N$, min$^{-1}$ | $D_{cell}$, μm | Width of transition zone, μm | Microhardness $HV$1, MPa | $Cr_{max}/Cr_{min}$ | | $Mo_{max}/Mo_{min}$ | |
| 1 | 7 | 25 | 28 | 60–80/90–120 | 35–40 | 5420–6060 | 4.5/3.4 | 1.32 | 0.32/0.25 | 1.28 |
| 2* | 7 | 25 | 45 | 30–40/70–90 | 20–25 | 5420–5480 | 4.8/3.9 | 1.23 | 0.40/0.33 | 1.21 |
| 3 | 7 | 40 | 18 | 50–60/70–80 | 30–35 | 6060–6130 | 3.4/2.3 | 1.47 | 0.42/0.32 | 1.31 |
| 4 | 7 | 40 | 32 | 40–50/60–80 | 15–20 | 5140–5400 | 3.1/2.2 | 1.41 | 0.35/0.28 | 1.25 |
| 5 | 10 | 25 | 28 | 25–35/25–50 | 35–40 | 6800 | 4.2/3.1 | 1.35 | 0.41/0.30 | 1.36 |
| 6 | 10 | 25 | 45 | 15–20/15–25 | 20–25 | 6700–6800 | 4.6/3.2 | 1.44 | 0.38/0.30 | 1.26 |
| 7 | 10 | 40 | 18 | 40–60/40–60 | 30–35 | 6400–6300 | 3.8/2.9 | 1.31 | 0.42/0.34 | 1.23 |
| 8 | 10 | 40 | 32 | 15–30/30–40 | 15–20 | 6340–6810 | 3.5/2.4 | 1.46 | 0.34/0.28 | 1.21 |

*Sample deposited in the optimum mode.
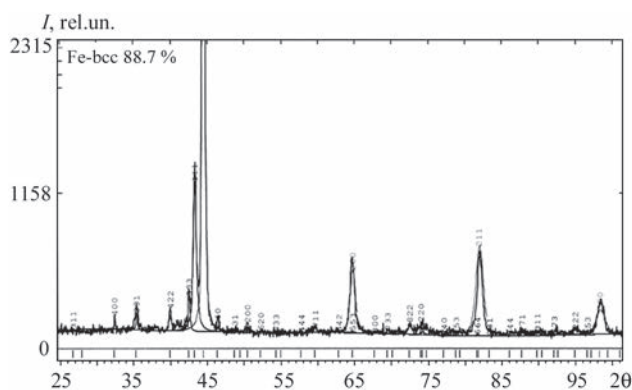
**Figure 10.** Phase composition of deposited metal of sample 2: Fe-bcc — 88.39 %; Fe-fcc — 8.11 %; $Fe_3Mo_3C$ — 3.00 %; $Cr_2C_3$ — balance

$Mo_{max}/Mo_{min}$ = 1.21–1.31. Increase of the frequency of electrode wire oscillations promotes producing a dispersed structure, more uniform distribution of alloying elements, «smoother» line of fusion of the deposited and base metal, as well as better mixing of the layers in the deposited metal. Hardness of the matrix base is 5140–6060 MPa. Carbides of $Cr_7C_3$, $Fe_3C$ type and intermetallics of $Mo_5Cr_6Fe_{18}$ type were found in the deposited samples (Figure 10).

Approximately the same pattern is observed at increase of deposition rate to 10 m/h (Table 2, samples 5–8). In this case, increase of oscillation frequency reduces the width of the transition zone, chemical heterogeneity of the deposited metal is $Cr_{max}/Cr_{min}$ = 1.31–1.46 for chromium; and $Mo_{max}/Mo_{min}$ = 1.21–1.36 for molybdenum. Hardness of the matrix base in this case is somewhat higher and equal to 6340–6810 MPa.

**Conclusions**

1. Increase of the frequency of electrode wire oscillations at the same amplitude and deposition rate leads to:

● improvement of deposited metal formation;

● improvement of mixing of the layers in the deposited metal; formation of a more dispersed structure;

● narrowing of the transition zone;

● more uniform distribution of alloying elements;

● more uniform nature of penetration and «smoothing» of the line of fusion of the deposited and base metal.

Here, it should be noted that these regularities practically do not change at increase of oscillation amplitude.

2. It was established that the best formation of the deposited metal, the smoothest and most uniform penetration are observed at electrode wire oscillation frequency $N = 45$ min$^{-1}$, electrode wire oscillation amplitude $A = 25$ mm and deposition rate $V_d = 7$ m/h.

1. Danilchenko, B.V., Shimanovsky, V.P., Voronchuk, A.P., Terpilo, V.N. (1989) Hard-facing of rapidly wearing parts by self-shielded flux-cored strips. *Avtomatich. Svarka*, **5**, 38–41 [in Russian].

2. Zhudra, A.P., Voronchuk, A.P., Fomakin, A.A., Veliky, S.I. (2009) New equipment for hard-facing of charging device bells and cups. *The Paton Welding J.*, **9**, 44–46.

3. Zhudra, A.P., Krivchikov, S.Yu., Petrov, V.V. (2010) Technology for wide-layer hard-facing of crankshafts. *Ibid.*, **2**, 32–35.

4. Gulakov, S.V., Burlaka, V.V. (2010) Mechanism of electrode oscillation for formation of deposited beads of complex shape. Vestnik Priazov. GTU. *Tekhnicheskie Nauki*, **20**, 181–186 [in Russian].

5. Spiridonov, N.V., Kudina, A.V., Kurash, V.V. (2013) Electric arc shielded-gas hard-facing of metal surfaces with oscillating electrode. *Nauka i Tekhnika*, **4**, 3–8 [in Russian].

6. Goloborodko, Zh.G., Dragan, S.V., Simutenkov, I.V. (2013) Automatic submerged-arc surfacing of structural steels with transverse high-frequency movements of electrode. *The Paton Welding J.*, **6**, 34–37.

7. Babinets, A.A., Ryabtsev, I.A., Kondratiev, I.A. et al. (2014) Investigation of thermal resistance of deposited metal designed for restoration of mill rolls. *Ibid.*, **5**, 16–20.

8. Ryabtsev, I.A., Babinets, A.A. (2015) Fatigue life of multi-layer deposited specimens. *Svarochn. Proizvodstvo*, **4**, 15–19 [in Russian].

# DEVELOPMENT OF NEW ELECTRODE MATERIALS, METHODS OF RESTORATION AND PROTECTION OF THIN-WALLED PARTS OF EQUIPMENT, WHICH ARE OPERATED UNDER THE CONDITIONS OF ABRASIVE AND GAS-ABRASIVE WEAR

**M.M. Student, A.A. Voytovych, Ya.Ya. Sirak** and **V.M. Gvozdetskyi**

G.V. Karpenko Physical-Mechanical Institute of the NAS of Ukraine
5 Naukova Str., 79060, Lviv, Ukraine. E-mail: pminasu@ipm.lviv.ua

A wide range of parts and equipment of chemical, oil, agricultural, machine-building, transport, energy and other industries are operated under abrasive wear conditions. In Ukraine, electric arc surfacing with flux-cored wires of the Fe–Cr–B–C system is widely used to protect against abrasive wear and restore worn surfaces by surfacing. Such flux-cored wires have a low cost and the deposited metal has a satisfactory wear resistance. However, the main disadvantage of the layers deposited by such flux-cored wires, are dendrites of the first and second order with acicular morphology. Sharp peaks of the solid phase act as stress concentrators, from which after impact the cracking of the deposited metal begins, followed by its chipping. It is known that the formation of rounded reinforcing phases reduces the concentration of stresses in the deposited layer and, as a consequence, increases wear resistance. This paper proposes the dispersion of structural components in the deposited metal by surfacing under the action of mechanical vibration on the deposited metal, which is especially rational to use for manufacture by surfacing of bimetallic wear plates, and for large-sized parts it is proposed to perform a dispersion of structural components in the deposited metal with modifying charge flux-cored wires of Fe–Cr–B–C system by adding PAM-4 powder of aluminium-magnesium master alloy to it. 5 Ref., 2 Tables, 5 Figures.

*Keywords: surfacing, bimetallic sheets, wear resistance, boride inclusions*

**Materials and procedures of investigations.** To form the deposited metal, flux-cored wires (FCW) with a diameter of 3.2 mm were used. Their sheath is made of a low-carbon steel 08kp (rimmed), filled with a powder charge based on ferroalloys. For the investigations FCWs were selected, having a ferritic or austenitic matrix in the deposited metal. The chemical composition of FCWs (Table 1) contains a high amount of chromium, boron, which has a positive effect on wear resistance of the deposited metal, as far as in the structure solid boride inclusions are precipitated.

The addition of PAM-4 powder of aluminium-magnesium master alloy to the charge of FCWs during surfacing forms a dispersed magnesium oxide in the welding pool, which affects the dispersion of the structural components, as well as strengthening of the deposited layer.

**Procedures of investigations.** The metal deposited by FCW was formed using suspension head ABS (power source is generator PSO 500). For protection against atmospheric influence, the flux OSTs 45 was used. The formation of deposited metal from FCWs was performed on a metal substrate of steel St3sp with the size of 150×300 mm in two layers. Vibration treatment [1–5] of the molten metal pool in the zone of electric arc burning was carried out under the following modes: oscillation frequency is 100 Hz, amplitude is 0, 70, 300 μm at a horizontal vibration. Microstructure of the deposited layers was studied on a transverse microsection using an electron microscope EVO 40 XVP. Hardness measurements were performed in a PMT-3 microhardness tester with a batch weight of 200 g. The wear resistance of deposited layers was investigated under different wear

**Table 1.** Chemical composition of the charge of the used flux-cored wires, wt.%

| Grade of FCW | C | B | Cr | Ti | Mn | Al | Mg | Si | Fe |
|---|---|---|---|---|---|---|---|---|---|
| Kh10R3G2S (ferritic matrix) | 0.08 | 3.5 | 10.0 | – | 2.0 | – | – | 1.0 | Balance |
| 80Kh20R3T (austenitic matrix) | 0.8 | 3.0 | 20.0 | 1.0 | – | – | – | | |
| 80Kh20R3T + 1 % of PAM (austenitic matrix) | 0.8 | 3.0 | 20.0 | 1.0 | – | 1.0 | 0.3 | | |

M.M. Student — https://orcid.org/0000-0002-5992-5898, Ya.Ya. Sirak — https://orcid.org/0000-0001-8748-8456
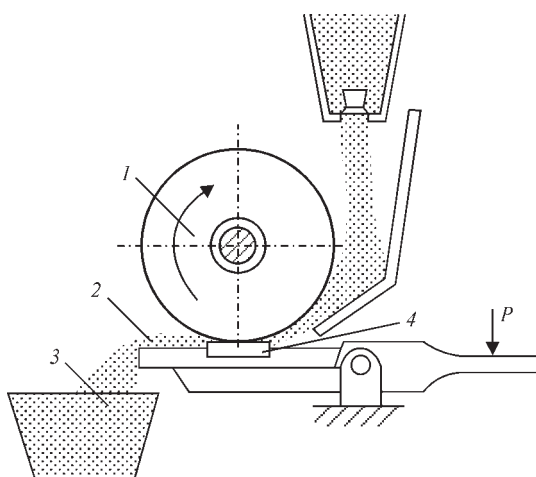
**Figure 1.** Scheme of installation for investigation of abrasive wear by an unfixed abrasive: *1* — rubber disc; *2* — sand; *3* — reservoir for collecting abrasive; *4* — specimen

conditions. Abrasive wear with an unfixed abrasive was evaluated according to GOST 23.208–79 (Figure 1). A dried high-silica sand with the particles size of 200–1000 μm was continuously supplied to the contact area of the rubber disc and the specimen. The speed of the disc rotation was 25 m/s, and the force of its pressing to the specimen was 2.4 kN.

To evaluate the wear of the fixed abrasive (Figure 2) an abrasive disc SM-2 on a ceramic bond was used. The linear friction speed was 0.4 m/s, the load in the area of a linear contact was 1.5 kN.

Impact wear (Figure 3) was evaluated at an impact force of 12 kJ applied by a ball with a diameter of 25 mm of steel ShKh 15, which fell on the test surface at a frequency of 40 s$^{-1}$. The duration of the experiment was 3600 s. The weight loss of the specimens was determined by electronic balance with the accuracy of $2 \cdot 10^{-4}$ g.

**Structure of deposited metal.** Phase analysis showed that the metal deposited by FCW Kh10R3G2S without vibration, consists of a ferritic matrix alloyed with chromium and boride inclusions (FeCr)B, (FeCr)$_2$B. It is known from the literature
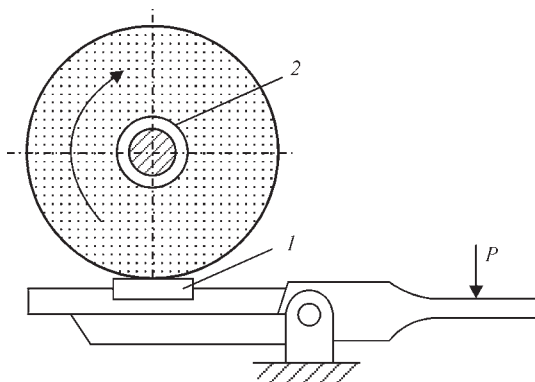


**Figure 2.** Scheme of installation for investigation of wear of specimens by a rigidly fixed abrasive: *1* — specimen; *2* — abrasive disc
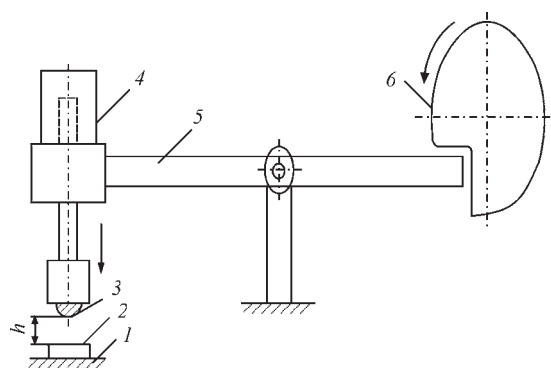


**Figure 3.** Scheme of installation for investigation of impact wear of specimens: *1* — base; *2* — specimen; *3* — indenter; *4* — batch weight; *5* — balance arm; *6* — eccentric; *h* — distance from the specimen is 10 mm

that the phase (FeCr)$_2$B contains a lower quantity of chromium and boron than the phase (FeCr)B and is characterized by a lower hardness, but a much higher ductility. Location of inclusions (FeCr)B, (FeCr)$_2$B in the structure of the deposited metal was identified by microspectral analysis on the sections. It was found that the inclusions of borides of the type (FeCr)B are larger and darker and borides of the type (FeCr)$_2$B are much smaller and lighter (Figure 4).

In the initial metal from FCW Kh10R3G2S the average size of boride inclusions (FeCr)B, (FeCr)$_2$B in the structure on the crest of the beads varied from 20 to 75 μm, and in the zone of their overlapping it varied from 50 to 150 μm. At a horizontal vibration with an amplitude of 300 μm, the average size of borides (FeCr)B, (FeCr)$_2$B decreased to 5–10 μm. The obtained results give grounds to assume that the horizontal vibration significantly disperses structural components of the metal deposited by FCW Kh10R3G2S. This was also checked on the structure of the metal deposited by FCW 80Kh20R3T at the amplitude of oscillations of the substrate of 70, 200 and 300 μm. It was found that also in this case the structural components of the deposited metal (boride inclusions) were significantly grounded with an increase in the oscillation amplitude during surfacing. In particular, boride inclusions (FeCr)B, (FeCr)$_2$B were maximum grounded by oscillations with an amplitude of 300 μm. The average size of the inclusions was 1–5 μm. Surfacing with the use of vibration of large-sized parts of a complex shape is significantly complicated or becomes impossible. In this case, it was proposed to influence the microstructure of the deposited metal by adding of up to 2 wt.% of PAM-4 powder to the charge of FCW 80Kh20R3T. Due to that, it creates the prerequisites for oxidation of magnesium located in the cavities of the FCW charge with the formation of dispersed particles of magnesium oxide, which become the centres of crystallization and growth of amount of grains from the melt of the deposited metal.
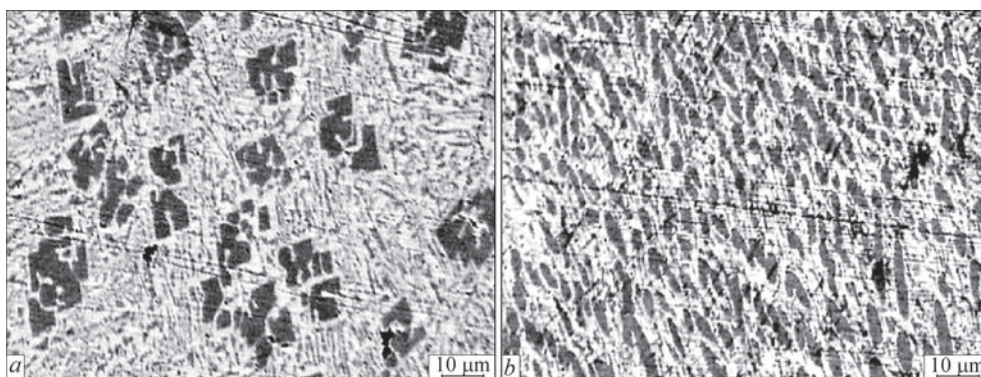
**Figure 4.** Microstructure on the crests of metal beads, deposited by FCW Kh10R3G2S: *a* — without the vibration; *b* — with the vibration of 300 μm amplitude

In the metal deposited by FCW 80Kh20R3T without adding PAM, acicular large (FeCr)B and small (FeCr)$_2$B borides are located on the background of the austenitic matrix. The microstructure of the metal deposited by FCW 80Kh20R3T of the base composition and with the addition of PAM powder to the charge was compared and it was found that magnesium alloying contributes to grinding of borides and their globalization.

Spectral and phase analyzes showed that with the addition of PAM powder to the FCW charge, in the microstructure of the deposited metal borides of the type (FeCr)$_2$B predominated. In the metal deposited by FCW 80Kh20R3T of the base composition, the size of borides was 30–120 μm, and in the metal deposited by FCW with the addition of PAM-4 powder their diameter decreased on the average by 8 times.

**Wear resistance of deposited layers.** It was established that the layers deposited under the conditions of mechanical vibration have an increased abrasive wear resistance. In particular, the abrasive wear resistance of the layer deposited by the fixed abrasive increased by 2.5 times, and by unfixed one by 2.3 times and under the conditions of a cyclic impact load by 2.8 times. An increase in wear resistance of the layers deposited under the conditions of mechanical vibration is predetermined by a significant reduction in the size of the dispersed reinforcing phases (borides) and a change in their phase composition. In particular, as the average size of boride inclusions decreased from 75 to 5 μm, its microhardness increased from *HV* 700 to *HV* 9300. As the content of the phase (FeCr)$_2$B in the deposited layer increased, the Young's modulus and resistance to brittle fracture increased, which also affected the improvement of wear resistance of the deposited layer (Table 2).

The application of oscillation during surfacing of the metal by FCW 80Kh20R3T, as well as for the metal deposited by FCW Kh10R3G2S, also leads to a significant decrease in the average size of boride inclusions and, as a consequence, its wear resistance

grows. In particular, with a decrease in the average size of boride inclusions from 70 to 5 μm under the conditions of wear by fixed and unfixed abrasive, the wear resistance of the deposited metal increases by 1.7 times, and during wear under the action of cyclic impact loads it grows twice.

Addition of 1 wt.% of PAM-4 to the charge of FCW 80Kh20R3T facilitates an increase in the wear resistance of the deposited metal by 1.6 times under the conditions of wear by fixed and unfixed abrasive; during wear under the action of cyclic impact loads, the wear resistance 1.8 times increased as compared to the metal deposited by FCW of the base composition. This improvement is predetermined by an increase in the hardness of the deposited layer both due to the dispersion of the reinforcing boride phase, as well as due to the additional precipitation of finely dispersed complex-alloyed nitrides in the structure of the deposited layer.

As an example of applying the process of surfacing by FCW, the works were carried out to restore the mill fan VM 100/1200 for the Burstyn TPP. In the system of dust preparation of boiler stations operating on solid fuel, the important components were mill fans. They perform pneumatic transportation of coal dust (with the fraction lower than 100 μm) at a temperature higher than 320 K from the cyclones to the dust feeders and further to the furnace of steam generators.

**Table 2.** Relative wear resistance of deposited metal with FCW Kh10R3G2S under the conditions of abrasive wear in relation to the deposited metal without the oscillation

| Surfacing conditions | Without vibration | Horizontal vibration | |
|---|---|---|---|
| Amplitude of mechanical oscillations, μm | – | 70 | 300 |
| Average size of borides, μm | 75 | 10 | 5 |
| By fixed abrasive | 1 | 1.4 | 2.5 |
| By unfixed abrasive | 1 | 1.5 | 2.3 |
| Under impact loads | 1 | 2.4 | 2.8 |
| Ratio of phases (FeCr)B/(FeCr)$_2$B | 4/1 | 2.5/4 | 1/5 |

**33**

**Figure 5.** Worn (*a*) and deposited (*b*) wheel blade of the mill fan, renovated wheels of the mill fan VM 100/1200 (*c*)

Therefore, during the operation of the described elements of boiler stations, an intense and nonuniform wear of their working blades, discs and walls of the chambers is observed. Nonuniform wear of the blades leads to a decrease in the power of fans and smoke extractors, unbalancing of rotors, contributes to the vibration of bearings, and, ultimately, destroys bearing units. The time of a continuous operation of smoke extractors in some cases is only 2–3 weeks.

Manufacture of a new mill wheel requires much more costs than surfacing of protective coatings. The main method to continue the operation of the mill wheel is its repair or replacement. Repair is offered to restore the geometric dimensions.

The main method of deposition a protective coating is semi-automatic surfacing. This surfacing allows applying the coating even in hard-to-reach places. For repair and strengthening of the mill fan VM 100/1200, FCW 80Kh20R3TMg was used, which was developed on the basis of FCW 80Kh20R3T with the addition of 1 wt.% of PAM-4 aluminium-magnesium master alloy to the charge (Figure 5).

Experimental and industrial inspection of the operation of mill fans, protected by a deposited layer of the wire PP-Np-80Kh20R3T, modified by the aluminium-magnesium master alloy, carried out at the Burshtyn TPP by the Institute of Physics and Mechanics jointly with the SE «Lviv Design Bureau» showed, that the service life of the strengthened impellers of the fans VM 100/1200 increased by 2.5 times.

## Conclusions

1. It was established that vibration of a part during its surfacing causes dispersion of the structure of the deposited metal, as a result of which the average size of separate boride inclusions decreases from 50–150 to 5–10 μm.

2. Mechanical vibration promotes redistribution of the phases during surfacing, as a result of which the microhardness of the deposited metal increases from *HV* 600 to *HV* 870 and is more uniformly distributed on the surface of the deposited metal. The deposited layers produced at a horizontal vibration showed an increased (2.3–2.5 times) abrasion wear resistance at the friction by a fixed and unfixed abrasive as compared to the layer deposited without the vibration.

3. It was established that vibration during surfacing layers increases (1.8 times) their stability at a cyclic impact load. The main factor influencing the impact wear of the deposited metal is its ability to plastically deform and, accordingly, to relax the stresses.

4. It was found that the addition of PAM-4 powder (up to 1 wt.%) to the FCW charge of the Fe–Cr–B–C base system promotes grinding of boride inclusions in the deposited metal (up to 7 times) and 1.6–1.8 times increase in the resistance to abrasive wear.

1. Kuskov, Y.M., Zhdanov, V.A., Ryabtsev, I.O. et al. (2020) Methods for increasing the corrosion resistance of coatings deposited under a flux layer from high-chromium powder wires. *Materials Sci.*, 55(**5**), 710–715.

2. Student, M., Vojtovych, A., Pokhmurska, H. et al. (2019) Mechanical characteristics and wear resistance of the cladding layers obtained by melting of cored wires with simultaneous vibration of substrate. *Strojnicky Casopis*, 69(**1**), 109–122.

3. Pokhmurs'ka, H.V., Student, M.M., Lanets', O.S., Voitovych, A.A. (2015) Influence of vibration in the course of surfacing of a protective layer on its microstructure and impact-abrasive wear. *Materials Sci.*, 51(**3**), 412–417.

4. Voitovych, A.A., Pokhmurs'ka, H.V., Student, M.M., Student, O.Z. (2016) Microstructure and abrasive-wear resistance of the vibration-deposited metal of core wires of the basic Fe–Cr–B system. *Ibid*, 52(**3**), 365–370.

5. Pokhmurs'ka, H.V., Student, M.M., Dzyubyk, A.R. et al. (2017) Corrosion resistance of the metal vibration deposited from flux-cored wires based on the Fe–Cr–B system. *Ibid.*, 52(**5**), 694–699.

# INFLUENCE OF ANTIMONY ON STRUCTURE AND MECHANICAL PROPERTIES OF PRE-EUTECTIC COPPER-PHOSPHORUS ALLOYS

**S.V. Maksymova, A.N. Pisarev, P.V. Kovalchuk** and **V.V. Voronov**

E.O. Paton Electric Welding Institute of the NAS of Ukraine
11 Kazymyr Malevych Str., 03150, Kyiv, Ukraine. E-mail: office@paton.kiev.ua

The results of investigations of pre-eutectic alloys of Cu–P–Sb system are presented. The melting temperature range was determined using high-temperature differential thermal analysis. It was found that antimony alloying of copper-phosphorus pre-eutectic alloy provides a decrease in the solidus and liquidus temperature. On the basis of experimental and literature data, the surfaces of liquidus and solidus of ternary alloys were constructed. Using micro-X-ray spectral analysis, the chemical composition and a number of structural components of Cu–6.29P–1.97Sb alloy were determined. The influence of antimony on technological and mechanical properties, as well as morphology of cast ternary pre-eutectic copper-phosphorus alloys is shown. 10 Ref., 2 Tables, 6 Figures.

*K e y w o r d s :  copper-phosphorus pre-eutectic alloys, antimony, temperature of solidus and liquidus, microstructure, ultimate tensile strength*

Copper-based alloys are widely used in modern mechanical engineering. They differ by chemical composition, physical and mechanical properties. Brazing is often applied for joining them that allows preserving the initial base metal structure and provides the specified mechanical characteristics. Alloys of copper-silver system are often used as brazing filler metals. They are characterized by an acceptable melting temperature range, sufficient ductility and strength [1]. The disadvantages of silver brazing filler metals include their high cost that increases the final price of the products. Economic inexpediency of application of such brazing filler metals often promotes wider ap-plication of less-expensive brazing filler metals based on copper-phosphorus system. At present brazing filler metals on copper-phosphorus base of eutectic and pre-eutectic composition are more promising substitutes of silver-containing brazing filler metals [1-4]. They have comparatively low melting temperature [5] and good physico-technological properties (Figure 1, *a*, *b*).

Phosphorus is a good deoxidizer for copper (residual oxygen content is close to zero). Formation of copper phosphides results in increase of binary alloy hardness. Phosphorus essentially reduces the melting temperature, improves the fluidity and wear resistance



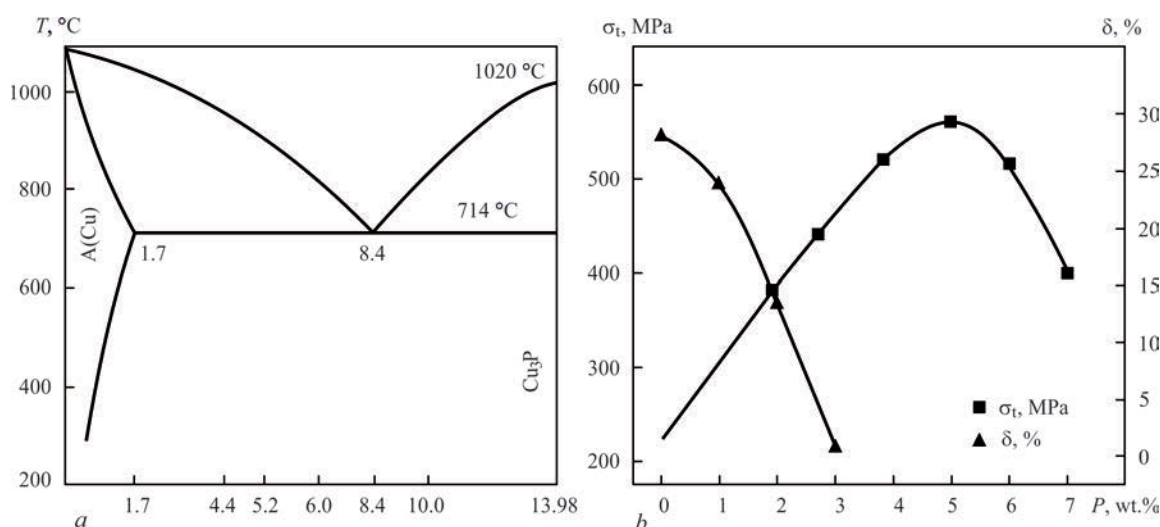**Figure 1.** Partial constitutional diagram of CuP system (*a*) and mechanical properties of binary alloys (*b*) [5, 6]

S.V. Maksymova — https://orsid.org/0000-0003-0158-5760, P.V. Kovalchuk — https://orsid.org/0000-0002-2313-5982,
V.V. Voronov – https://orsid.org/0000-0002-0410-1154

of the brazing filler metal. However, alloys of eutectic composition are extremely brittle (Figure 1, *b*). In order to preserve the high ductility properties and lower the melting temperature of brazing filler metals of copper-phosphorus system, containing 3–6 wt.% phosphorus, additional alloying by other elements, such as silver, zinc, tin and antimony is used [4].

The experience of the last decades showed that in most of the cases such brazing filler metals can be used for brazing the most nonferrous metals and alloys. Antimony is one of the elements reducing the melting temperature of alloys of copper-phosphorus system. It can be assumed that antimony, being in the same group of periodic table with phosphorus, can have a positive impact on melting temperature and phase composition of the filler metal of ternary Cu–P–Sb system.

This work presents the results of investigation of the influence of antimony as one of the depressants of copper-phosphorus filler metals, on the solidus and liquidus temperature, structure and mechanical properties of pre-eutectic alloys of copper-phosphorus system.

**Materials and methods of investigations.** Experimental brazing filler metals were melted in a graphite crucible in the laboratory resistance furnace. Phosphorus copper MF10 with 10.18 % wt.% phosphorus, copper M1, and antimony Sb00 were used as the charge. Phosphorus concentration was varied in the range from 3 to 6 %, that of antimony — from 2 to 6 %. After component melting, the alloy was soaked up to complete dissolution of the component elements. Cast billets were used for chemical analysis and conducting metallographic investigations of experimental filler metals.

Melting temperature of experimental alloys was determined, using a unit for high-temperature differential thermal analysis in a helium atmosphere.

Metallographic investigations were conducted using optical (Neophot 32) and scanning electron microscopy (TescanMira 3 LMU). Chemical element distribution was determined by the method of local X-ray microanalysis, using energy-dispersive spectrometer Oxford Instrument X-max 80 mm² with application of INCA program package. Locality of X-ray microscopic measurements did not exceed 1 μm, microstructure filming was conducted in back-scattered (BSE) electrons that allows studying the microsections without chemical etching.

Mechanical testing was conducted with application of experimental brazing filler metals in the cast state. Obtained ingots were used to make M12-6K samples to GOST1497–73.

**Investigation results and their analysis**. Binary Cu–P, Cu–Sb systems are already well studied, and the constitutional diagrams are given in publications [5]. These are diagrams of eutectic type. The eutectics form between solid solutions and chemical compounds. This leads to the assumption that the ternary system also has an eutectic component. Phosphorus and antimony have a considerable influence on the melting temperature of copper alloys. At the temperature of 200 °C up to 2 wt.% antimony dissolves in copper. Therefore, alloying of copper alloys by antimony in this concentration range should not cause formation of additional phases. Binary diagrams have steep liquidus lines near eutectic transformation points [5].

In phosphorus-antimony binary system no compounds of antimony with silver were found, but at cooling below 612 °C the saturated melt decomposes into the solid and gaseous phases [7]. In the solid state, phosphorus and antinomy do not impair the mechanical properties of copper [8, 9].

Known is the positive influence of antimony and phosphorus on surface tension of antimony and its melting temperature [9]. Addition of these elements
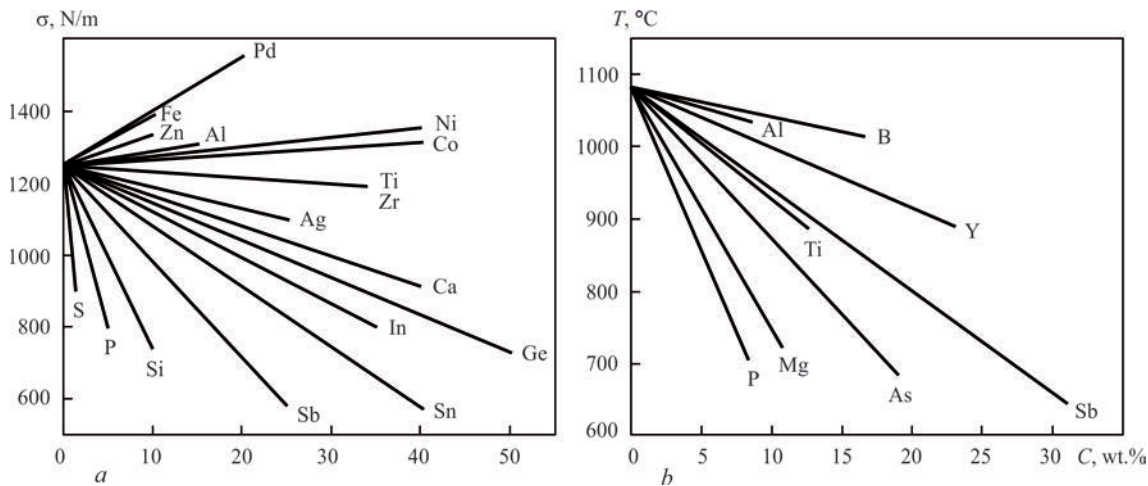


**Figure 2.** Influence of chemical elements of the composition C on surface tension (*a*) and copper melting temperature (*b*) [8, 9]

to copper reduces the surface tension (Figure 2, *a*) and lowers the melting temperature (Figure 2, *b*).

High-temperature differential thermal analysis of the studied alloys showed that when adding antimony to the pre-eutectic alloy of copper-phosphorus system, a lowering of solidus and liquidus temperature is observed (Table 1).

So, increase of the amount of antimony from 1.5 to 5.64 wt.% at phosphorus content > 5.0 wt.% leads to lowering of solidus temperature from 655 to 620 °C. Liquidus temperature here also decreases from 680 to 660 °C. In fact, increase of phosphorus and antimony content leads to a significant lowering of solidus temperature and certain lowering of liquidus temperature, compared to previous alloys.

Liquidus (Figure 3, *a*) and solidus (Figure 3, *b*) surfaces of experimental alloys were plotted, proceeding from the obtained results of high-temperature differential thermal analysis, published data of constitutional diagrams of binary alloys with application of mathematical methods of data processing.

**Table 1.** Physico-technological properties of experimental alloys of Cu–P system alloyed by antimony

| Alloy number | Element content, wt.% | | | Melting temperature, °C | | | Spreading area, mm² |
|---|---|---|---|---|---|---|---|
| | Cu | Sb | P | $T_S$ | $T_L$ | $\Delta T$ | |
| 1 | | 5.87 | 3.61 | 625 | 665 | 45 | 218.75 |
| 2 | | 4.96 | 4.37 | 620 | 690 | 70 | 364.6 |
| 3 | | 3.87 | 5.2 | 685 | 700 | 15 | 364.6 |
| 4 | | 4.97 | 3.31 | 650 | 715 | 65 | 218.75 |
| 5 | Base | 2.97 | 4.14 | 690 | 780 | 90 | 218.75 |
| 6 | | 3.70 | 3.0 | 640 | 710 | 70 | 291.6 |
| 7 | | 3.75 | 4.44 | 630 | 700 | 70 | 291.6 |
| 8 | | 1.50 | 5.05 | 655 | 680 | 25 | 364.6 |
| 9 | | 2.97 | 5.2 | 655 | 670 | 15 | 364.6 |
| 10 | | 5.64 | 6.78 | 620 | 660 | 40 | 372.4 |

These surfaces allow reducing the number of experiments at selection of specific chemical composition of the brazing filler metal, which the most completely corresponds to the specified requirements and specified temperature ranges of solidification. They correlate well with the results obtained using the regression models [10].
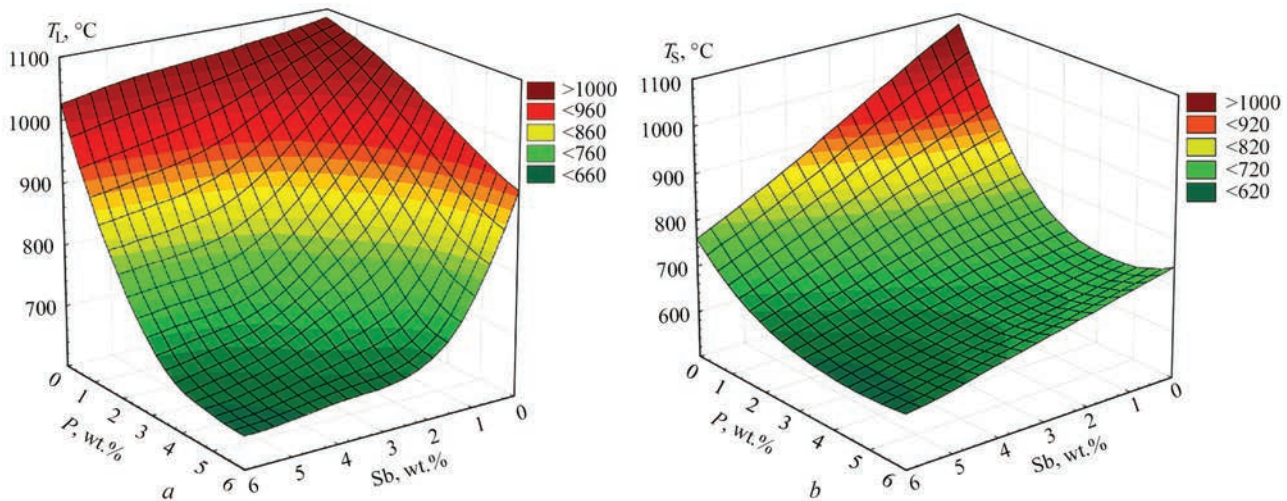


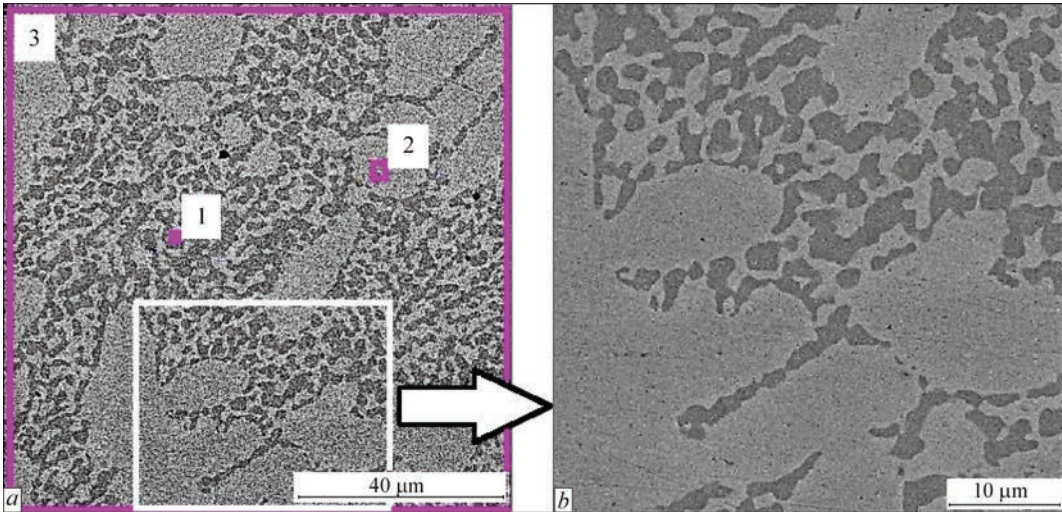**Figure 3.** Liquidus (*a*) and solidus (*b*) surfaces of alloys based on Cu–P–Sb system



**Figure 4.** Phases, in which chemical composition (*a*) and microstructure (*b*) of ternary alloy Cu–6.29P–1.97Sb were determined
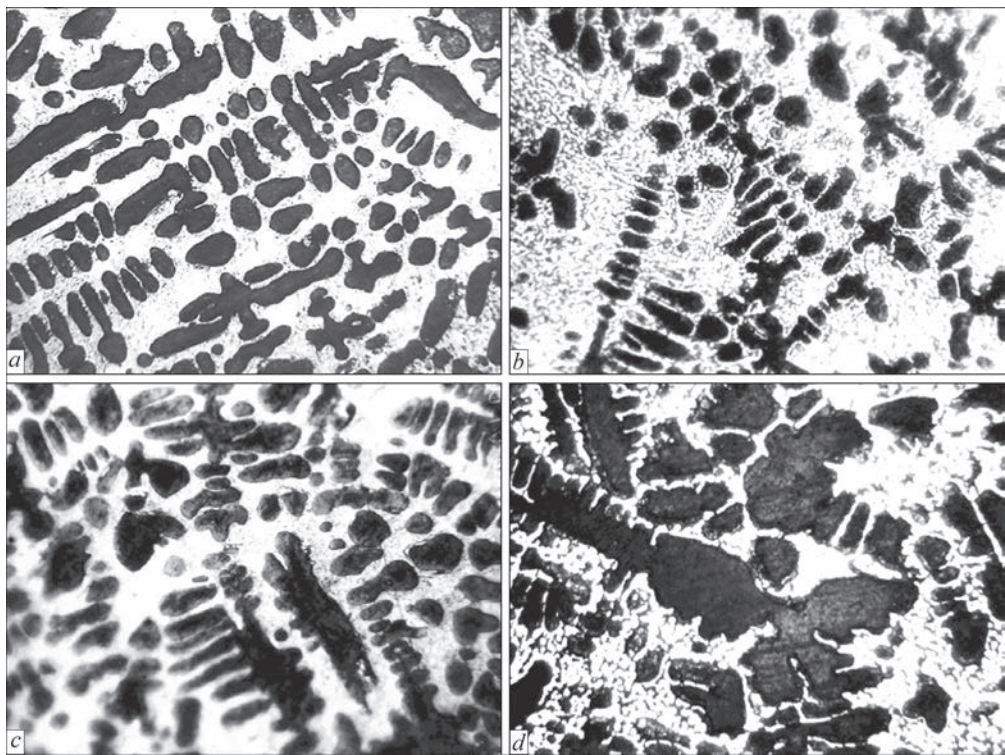
**Figure 5.** Microstructure of Cu–P–Sb alloy at different content of antimony: *a* — 0; *b* — 3; *c* — 4; *d* — 5 % and constant content of phosphorus of 5 w.% (×500, optical microscope)

Investigations of spreading over copper of copper-phosphorus filler metals alloyed with antimony, showed that simultaneous increase of phosphorus and antimony concentration leads to enlargement of the spreading area (see Table 1). A pre-eutectic alloy, containing more than 5 % antimony and more than 6 % phosphorus, is characterized by maximum spreading area.

Results of X-ray microanalysis showed that the microstructure of the cast alloys with 2 % antimony, is formed by the following phases: primary dendrites of α-solid solution of phosphorus and antimony in copper; copper phosphide ($Cu_3$, P) in the form of dark in-

clusions and rod-like eutectic, that consists of the solid solution and phosphide of copper (α-Cu + $Cu_3P$), which precipitates in interdendritic regions (Figure 4, Table 2).

Antimony concentration in copper phosphide exceeds its concentration in the solid solution (see Table 2).

Optical microscopy studies of the structure revealed that the alloys of copper-phosphorus system at a constant phosphorus content (5 %) retain the morphological features with increase of antimony concentration, but increase of the fraction of copper-based solid solution α-Cu and of the dendrite dimensions is observed, which is characteristic for pre-eutectic alloys (Figure 5).

Mechanical testing of brazing filler metals at room temperature showed that at 4 wt.% concentration of phosphorus maximum values of ultimate tensile strength ($\sigma_t$) of ternary Cu–P–Sb alloys with 3, 4 and 5 wt.% antimony are observed. It should be noted that further increase of the amount of antimony in the pre-eutectic copper-phosphorus alloy with up to 5 %



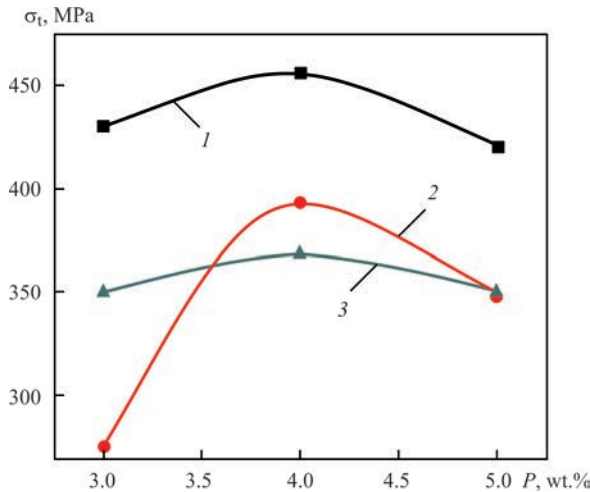**Figure 6.** Ultimate strength of experimental alloys of Cu–P–Sb system, depending on the degree of phosphorus and antimony alloying: *1* — Sb = 3; *2* — 4; *3* — 5 %

**Table 2.** Chemical composition of structural components of Cu–6.29P–1.97Sb, wt.% ternary alloy

| Spectrum number | P | Cu | Sb |
|---|---|---|---|
| 1 | 13.87 | 84.93 | 1.20 |
| 2 | 0.92 | 98.54 | 0.54 |
| 3 | 6.29 | 91.74 | 1.97 |

phosphorus, leads to lowering of ultimate strength (Figure 6).

Obtained investigation results show that acceptable strength characteristics are found in pre-eutectic copper-phosphorus alloys, where antimony concentration does not exceed 3 wt.%. In its turn, lowering of the content of phosphorus (≤ 3 wt.%) and antimony (≤ 2 wt.%) promotes considerable increase of brazing temperature and deterioration of filler metal spreading.

Brazing filler metals of Cu–P–Sb system have been successfully tested in brazing of a number of products and individual assemblies from copper and its alloys in electrical engineering industry, as well as dissimilar metals, in particular, copper alloy with 29NK precision alloy. These filler metals provide good service properties of brazed structures from corrosion-resistant copper-nickel alloys (German silver) that are used in marine shipbuilding.

## Conclusions

Pre-eutectic alloys of copper-phosphorus-antimony system were studied. High-temperature differential thermal analysis showed that increase in the amount of antimony from 1.5 to 5.64 wt.% at phosphorus content > 5.0 wt.% leads to lowering of the solidus and liquidus temperature from 655 to 620 °C, respectively. Liquidus and solidus temperatures of pre-eutectic alloys of Cu–P–Sb system were plotted, proceeding from the experimental and literature data.

Local X-ray microanalysis showed that the main structural components of pre-eutectic alloys of copper-phosphorus-antimony system are primary dendrites of copper-phosphorus-antimony solid solution. Rod-like eutectic formed by copper phosphide and copper-based solid solution precipitates in interdendritic regions.

At constant concentration of phosphorus of 4 wt.% maximum tensile strength is observed in cast copper alloys doped by antimony in the amount from 3 to 5 wt.%. At further increase of the amount of antimony, a decrease in strength is found in pre-eutectic copper-phosphorus alloy with up to 5 % phosphorus, so its concentration should be limited.

1. Petrunin, I.E. (2003) *Handbook on brazing*. Moscow, Mashinostroenie [in Russian].
2. Pashkov, I.N., Ilina, I.I., Shapiro, A.E. (2006) Properties and applications of Cu-based silver free brazing filler metals made by rapid solidification technique. In: *Proc. of the 3rd Int. Brazing and Soldering Conf. (San Antonio, Texas, USA)*, 157–166.
3. Pashkov, I., Pashkov, A. (2012) Change in phase morphology and composition during the spreading of liquid alloy, which is actively interacting with base metal surface. In: *Proc. of the 5th Int. Brazing and Soldering Conf. (Las Vegas, Nevada, USA)*, 240–243.
4. Boutilier, J., Brown, N., Klidas, N., Alexandrov, B.T., Shapiro, A.E. (2018) Strength of steel, copper, and brass lap joints brazed by silver-based and silver-free filler metals. In: *Proc. of the 7th Int. Brazing and Soldering Conf. (New Orleans, USA)*, 360–366.
5. Drits, M.E. (1979) *Binary and multicomponent systems based on copper* (Reference). Moscow, Nauka [in Russian].
6. Vozdvizhensky, V.N., Grachev, V.A., Spassky, V.V. (1984) *Casting alloys and their melting technology in mechanical engineering*. Moscow, Mashinostroenie [in Russian].
7. Lyakishev, N.P. (1999) *Constitutional diagrams of binary metal systems*. In: Refer. Book: 3 Vol., Vol. 3. Book. 1. Moscow, Mashinostroenie [in Russian].
8. Smiryagin, A.P., Smiryagina, N.A., Belova, A.V. (1974) *Industrial nonferrous metals and alloys*. Moscow, Metallurgiya [in Russian].
9. Suchkov, D.I. (1967) *Copper and its alloys*. Moscow, Metallurgiya [in Russian].
10. Pisarev, A.N., Doroshenko, L.K., Safronova, E.A. (1992) Copper fusibility angle of the copper-phosphorus-antimony system. In: *Physical chemistry and technology of phosphides of phosphorus-containing alloys*. In: 2 Parts. Pt 2. Alma-Ata, Gylym, 18–22 [in Russian].

# MECHANIZED WELDING OF LAMINATED PVC FABRICS WITH HOT AIR

**M.G. Korab, M.V. Iurzhenko, A.V. Vashchuk** and **M.G. Menzheres**

E.O. Paton Electric Welding Institute of the NAS of Ukraine

11 Kazymyr Malevych Str., 03150, Kyiv, Ukraine. E-mail: korab_nikolay@ukf.net

Technical laminated fabrics, which are used for the manufacture of awnings and inflatable products for different purposes, are made with double-sided PVC coating. The most widespread practical method of manual and mechanical welding of laminated fabrics with PVC coating is hot air welding. In this work, the features of hot air welding of the overlap welds of laminated PVC fabric were investigated in the manufactured experimental set up. The geometric dimensions and shape of the produced experimental welds from laminated fabric Unisol 950 (specific weight of 950 g/m$^2$) were established. In the course of the work, the mechanical strength of the welds produced by experimental welding was investigated, as well as tear test of the welds was carried out. The range of welding speed was set, within which welded joints of the laminated fabric are formed with tight penetration. It is shown that a tight penetration along the entire plane of the welded joint is achieved by forming a bead of molten PVC, uniform as to its diameter, under the pressure roller in the welding process. The nature of running of thermal processes in the welding zone was evaluated by the geometric parameters of the melt bead. The optimal parameters of the process of producing the butt welds of laminated fabrics, joined by a tape on both sides, and visual criteria for sound joint formation were determined, and the principles of manual control of the hot air welding process in real time were developed. 4 Ref., 10 Figures.

*K e y w o r d s :  welded joints, laminated PVC fabric, hot air welding*

Laminated fabrics are a separate kind of thermoplastic composite materials (TCM) which are widely applied in different branches of the national economy: for manufacturing a wide range of consumer goods, as well as numerous products for engineering applications, such as awnings, architectural awnings, and inflatable products. They are produced by treatment of fiber base fabrics by different polymer compositions: melts, solutions, dispersions and pastes. Thus, laminated fabrics are textile sheets, the main characteristic of which is the pattern of thread weaving, i.e. a certain order of overlap of longitudinal (warp) threads with transverse (weft) threads. Such fabrics have high anisotropy of mechanical and electric characteristics that creates technological complexities during their welding. One of the main methods to join polymer laminated fabrics is hot air welding.

A large part of laminated fabrics are made using plasticized polyvinylchloride (PVC) as coating. Polyvinyl chloride is a transparent thermoplastic polymer, a product of polymerization of vinyl chloride (ethylene chloride). At present, PVC is the second most consumed polymer with the annual world production volume of more than 25 mln t. Pure polyvinylchloride is a rigid material, which becomes elastic only after heating up to the temperature of 70–75 °C. However, PVC elasticity can be achieved at room temperatures by adding special plasticizers, namely ethers of various alcohols and dicarbonyc acids. Salts of tin, barium, cadmium and calcium (3–5 mass fract.) are used as thermal stabilizers of plasticized PVC. Their main objective is material stabilization due to binding hydrogen chloride (HCl), which forms during thermal oxidative destruction of PVC at higher service temperatures [1].

Technical laminated fabrics, which are used to manufacture awning and inflatable products for different applications, which are made with two-sided PVC coating. Such fabrics have higher elasticity and high strength, their coating is airtight and resistant to the impact of sunlight, atmosphere and water. The majority of technical PVC fabrics are made by SOL-technology (from the English solution). By this technology, calendering of the fabric base by a solution of plasticized PVC in a light organic solvent is performed. In order to improve the adhesion of PVC coating with the sheet, two thin layers of polymer glue-adhesive are applied on the fabric simultaneously with calendering. Thus, the laminated PVC fabric has a five-layer structure (Figure 1). Products from the leading manufacturers are presented in the market, in particular fabrics for inflatable boats: Valmex, Plastel (Czechia), Heytex (Germany), Unisol Boat (South Korea), etc. [2]. Specialized laminated PVC fabrics are not yet produced in Ukraine.

M.G. Korab — https://orcid.org/0000–0001–8030–1468, M.V. Iurzhenko — http://orcid.org/0000–0002–5535–731X,
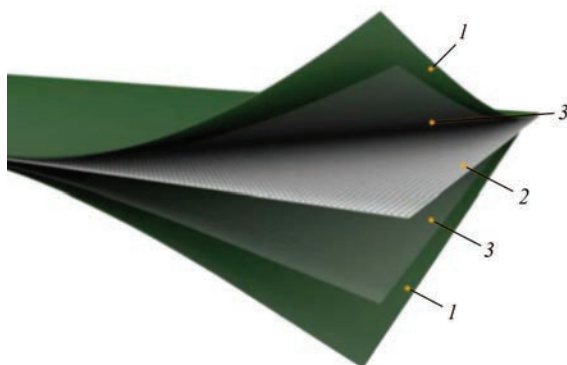A.V. Vashchuk — http://orcid.org/0000–0002–4524–4311

**Figure 1.** Scheme of design of laminated PVC fabric: *1* — outer and inner PVC layers; *2* — polyester woven base; *3* — layers of polymer adhesive



**Figure 2.** Scheme of overlap welding of fabrics with PVC coating using hot air: *1* — fabrics being welded; *2* — press-down roller; *3* — nozzle for overlap welding; *4* — hot air heater

Fabrics, laminated by plasticized thermoplastic PVC are suitable for welding by a heated tool (wedge) and hot air, as well as high-frequency welding [3]. High-frequency welding requires complex and costly equipment, which is designed for joining small rectilinear or local welds in one cycle. The heated wedge is applied as a rule, for joining thick polymer films and fabrics with thick polymer coating at manufacture of waterproofing compound and large tanks. Hot air welding is the method of welding laminated fabrics with PVC coating, which is the most widely accepted in practice. In this case, heating the parts to be welded is performed by a hot air jet of the temperature of 250–400 °C, and press-down rollers of various designs are used to form the welded joint. Hot air welding can be performed with addition of the filler material and without it, in the manual and mechanized mode. The method of hot air welding is versatile and flexible; it enables welding materials of a broad range of thicknesses, making welds of a complex configuration and located in different positions in space, and does not require complex equipment. The main element of any equipment for hot air welding is a special heater — a dryer fitted with the respective nozzles [4].

The schematic of the process of overlap welding of laminated fabrics in the manual and mechanized modes is shown in Figure 2. In overlap welding, the heater nozzle contacts the fabric surface directly. It leads to fracture and destruction of PVC coating of the fabric, and sticking of the molten polymer to the nozzle surface that does not allow producing sound joints for thin fabrics over the entire area of the overlap weld. Thus, it is rational to use semi-automatic machines for butt welding of fabric elements by a tape, in order to weld fabrics with a thin layer of PVC coating. In this case, there is no contact of the fabric surface with the heater nozzle, and the welding zone is heated exclusively by a hot air jet.

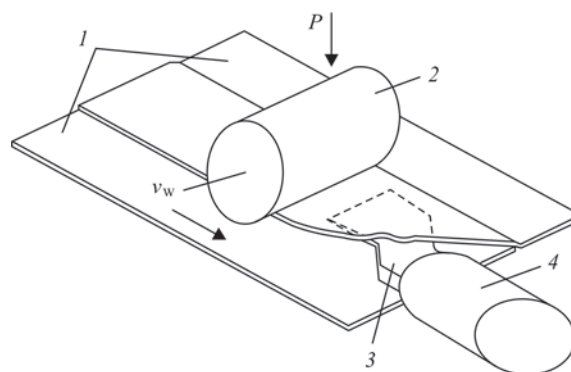Practical experience proves that in manufacture of awning and inflatable products the required quality is provided by application of butt welds of the laminated fabric, joined by a tape from both sides. Here, the outer tape of the weld provides the main strength of the joint, while the inner tape is additional and ensures normal formation and tightness of the joints. Therefore, the inner tape is not welded separately, but is covered by the glue and is used as the backing for joining the laminated fabric. At heat sealing of the outer tape, the adhesive layer is activated, so that the inner tape is bonded to the butt.

In this work, an experimental set-up was manufactured for hot air welding of butt welds of laminated PVC fabrics. In this unit a modified carriage with an electromechanical drive from Leister semi-automatic machine was used for movement of the dryer and press-down roller along the butt of the fabrics. The scheme of the technological process of welding laminated PVC fabrics by a tape using hot air is shown in Figure 3. The butt of the two parts from laminated fabric *1* was placed on a solid surface together with backing tape *3* from the same material or from PVC film, coated by a thin layer of polyurethane glue. Bonding was performed using tape *2*, cut out of the same laminated fabric, as the parts. The welded joint was formed, using a roller with rubber coating *4* that was pressed to the tape and the parts from laminated fabric with force *P* and was displaced along the welding line at speed $v_w$. It should be noted that the roller width is by 2–3 mm greater than the width of the tape for welding.
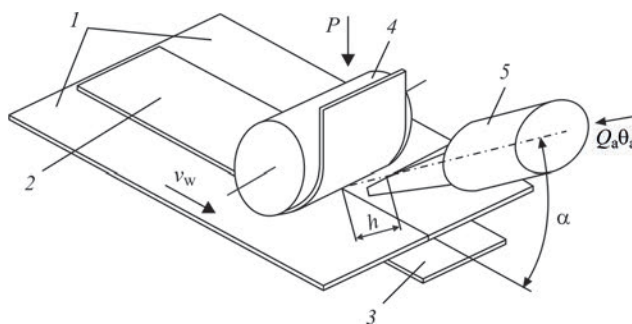


**Figure 3.** Scheme of butt welding of artificial leather with a tape using hot air: *1* — laminated fabrics being welded; *2* — connecting tape from laminated fabric; *3* — backing tape from laminated fabric; *4* — press-down roller; *5* — hot air heater with nozzle

Heating of the welding zone was performed by hot air that is supplied from the heater — electric heating dryer *5* through a flat nozzle, the width of which was equal to the width of the tape for welding. The main parameters of the heater are as follows: heated air temperature $\theta_a$ and air flow rate $Q_a$. The nature of heating of artificial leather in the welding zone was affected by the angle of positioning of heater nozzle $\alpha$ and distance from the nozzle to fabric *h*. The nozzle was located parallel to the joint plane, and the nozzle edge was parallel to the roller axis.

The width of the main tape from laminated PVC fabric for welding and backing tape was the same and equal to 38–40 mm. It should be noted that PVC fabrics with a lower specific weight can be also used as backing tape. During heat sealing the backing tape is heated up to the temperature of 70–80 °C. At heating, the adhesion ability of the interlayer of polyurethane glue increases significantly, and the tape sticking to the lower part of the welded joint takes place. It ensures the joint sealing and its additional strength.

In order to study the process of hot air welding of Unisol 950 laminated fabric of 0.8 mm thickness with specific weight of 950 g/m² straight experimental welds of 1.0–1.5 m length were produced. Welding was performed on a horizontal table with a longitudinal slot 40 mm wide and 0.8 mm deep for laying the backing tape. Leister Triak-S air heater with a flat nozzle 40 mm wide and press-down roller of 42 mm width and 30 mm diameter with heat-resistant rubber coating were installed on the carriage. Triak-S heater had a stable value of heated air flow of 230 l/min, air temperature was controlled by a regulator on the unit casing. Carriage movement speed was adjusted by its electric drive regulator. The load on the press-down roller was regulated by placing measured loads on the carriage.

It is determined that the optimum distance from the heater nozzle to the welding zone is equal to 7–8 mm. In this case, sufficient visibility of the heated fabric under the roller is ensured, and excess overheating of the fabric near the welded joint takes place. The load



**Figure 4.** Sound weld of Unisol 950 laminated fabric after testing for tearing off of connecting tape: *1* — torn off tape with exposed cord; *2* — weld; *3* — HAZ near the weld

on the press-down roller that ensured normal formation of the welded joint, was equal to 5–6 kg (1.25–1.5 kg/cm). Experimental welding of joints of Unisol 950 laminated fabric was also performed with different values of hot air temperature and welding speed.

In order to determine the experimental weld strength, testing for uniaxial tension of laminated fabric strips 50 mm wide, cut out of samples in the transverse direction with the weld located in the strip middle, was conducted. Testing showed that the strength of sound welds is equal to base metal strength and is 290–310 kg that corresponds to the declared strength of Unisol 950 laminated fabric in the transverse direction (weft direction). The laminated fabric strips that were tested by tension, failed mainly in the base material. The main defect that reduced the weld strength, were lacks-of-penetration. Joints with lacks-of-penetration failed in the weld during tensile testing at smaller load values.

The quality of welded joints of laminated fabric can be evaluated also without conducting complex mechanical testing by application of express-method of testing the welds for pulling off the connecting tape. The tape welded from the weld end face is torn off the butt on a short length using a knife and pliers, the weld edge is clamped in a vice, the tape is held in pliers with wide jaws and is torn off the weld on its entire length. In the case of a sound bonding of the tape and the base material the coatings are fused together, and when the tape is torn off the weld, its cord or the cord of the base laminated fabric are bared, and the layer of fused PVC remains on the opposite side.

At pull testing of the weld with complete penetration, tape tearing off with complete exposure of the cord usually occurs (Figure 4). A uniform layer of fused PVC with traces of cord threads remains on the welded joint. Adhesion of the tape cord to PVC layer is so strong that destruction of the cord is observed on the one side of the tape at pulling off. The lower backing tape functionally has an additional role in the welded joint. At tearing off from the base it usually separates from the weld along the adhesive layer without destruction of PVC coating of the laminated fabric.

The main factors influencing the heat processes in the zone of fabric welding, and, thus, the weld quality, are the heated air temperature and welding speed. With rising of the air temperature, the welding speed, and, hence, labour efficiency, increase, but, on the other hand, the probability of overheating of the welding zone becomes higher. At overheating, not just the thin layer of PVC on the fabric coating is melted, but also the entire coating, particularly in the HAZ near the weld. In welding a large amount of PVC melt is removed from under the connecting tape, it sticks to the roller and forms sharp protrusions at solidifi-
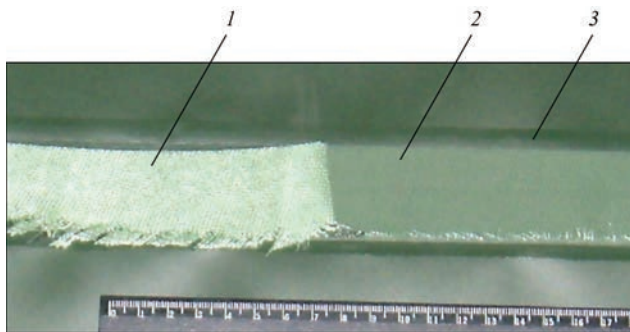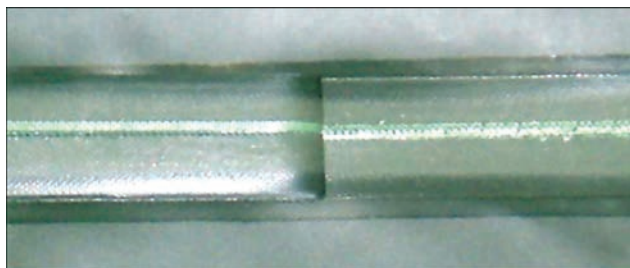
**Figure 5.** Weld of Unisol 950 laminated fabric made with insufficient heating of the welding zone

cation. In an overheated weld, all the layers of PVC coating on artificial leather are deformed and thinned. Such welds do not satisfy the requirements, either on strength and tightness or on appearance.

At lowering of the hot air temperature the probability of insufficient heating of the welding zone becomes higher. In this case, PVC coating of artificial leather usually melts only in the weld central part. At testing of such a weld for tape tearing off (Figure 5), the cord is bared only in a narrow band near the joint axis, while bands of total lack-of-penetration are observed along the weld edges.

The results of studying the experimental welds, made at different parameters of the mode, were used to determine the ratios of hot air temperature $\theta_a$ and welding speed $v_w$, at which normal welded joint formation is observed from the outside. At welding at hot air temperatures below 400 °C and low welding speeds, formation of regions of insufficient heating of the fabric and of local lacks-of-penetration is possible (Figure 6). Such regions cannot be detected visually, by examining the fabric weld from the outside. In service of a product with local lacks-of-penetration inside the welds, its sudden destruction can occur in extreme loading mode. In order to guarantee sound welds, modes with average values of air temperature on the level of 420–450 °C at heater outlet and corresponding values of welding speed should be selected. Separate factors, influencing formation of penetration in artificial leather joints, are nonuniform heating of the welding zone over the weld width and nonuniform pressure on artificial leather over press-down roller width. In this case, a longitudinal lack-of-penetration forms from one of the weld sides (Figure 7).

The axis of rotation of the press-down roller should be exactly parallel to welded joint plane. At deviation from parallelism, the roller pressure on one edge of the weld increases and the pressure on the opposite edge decreases. Consequently, removal of PVC melt from under the tape and formation of excess flash occur in the higher pressure zone. From the opposite edge of the weld, the pressure value turns out to be insufficient, molten PVC layers do not bond with each other and lack-of-penetration forms. At shifting of the hot air unit nozzle to the side, or deviation of nozzle axis from the axes of symmetry, an insufficiently heated
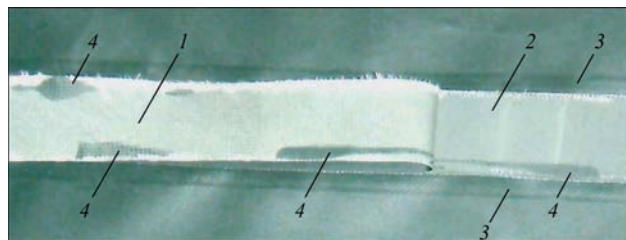


**Figure 6.** Weld of Unisol 950 laminated fabric with local lacks-of-penetration in the weld after testing for tearing off of the connecting strip: *1* — torn off tape with exposed cord; *2* — weld; *3* — HAZ near the weld; *4* — region of lack-of-penetration on the tape and on the weld

zone appears from one of the sides of the press-down roller and a lack-of-penetration also forms.

The absence of continuous and local lacks-of-penetration in the weld can be a criterion for evaluation of the quality of laminated fabric welded joint. A sound weld should have a 100 % penetration that is revealed as complete tearing off of the connecting tape cord from the weld PVC. Welds made at experimental welding in different modes, were tested for tape tearing off, and then the percentage of unwelded zones per a unit of weld area was determined. Analysis of investigation results showed that there exists a range of welding speeds of 0.07–0.12 m/s, in which welded joints of laminated fabric with complete penetration form, yielding 100 % value of penetration density P (Figure 8). Average values of heated air temperature of 420–450 °C at the outlet from heater nozzle correspond to these speeds.

It should be noted that during welding various process disturbances, shifting of parts from laminated fabric or of welding tools may arise that causes appearance of defective areas of the weld. Another problem also is ensuring normal formation of the joint at the start and end of the weld. That is why, the need arises for development of a special procedure for controlling the welding process and correction of its parameters in real time during welding. It was experimentally established that continuous tight penetration over the entire area of the welded joint is achieved at formation of a molten PVC bead of uniform diameter under the press-down roller in welding (Figure 9).
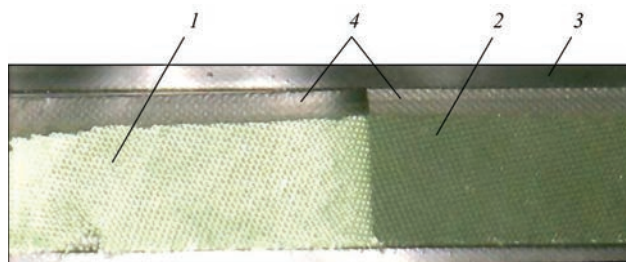


**Figure 7.** Weld of Unisol 950 laminated fabric with a lack-of-penetration near the weld edge after testing for tearing off of the connecting tape; *1* — torn off strip with exposed cord; *2* — weld; *3* — HAZ near the weld; *4* — zone of lack-of-penetration on the weld and on the tape
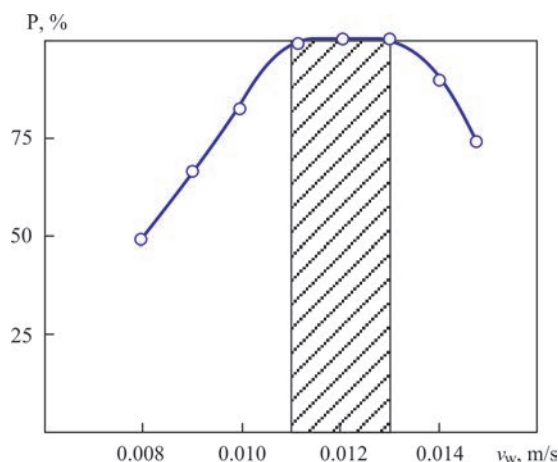
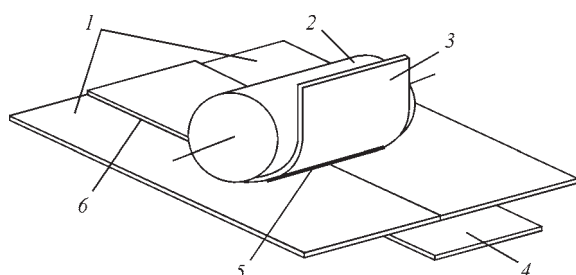**Figure 8.** Dependence of tightness of penetration of the laminated fabric welded joint on welding speed



**Figure 9.** Scheme of optimal process of hot air welding of laminated fabric: *1* — laminated fabrics being welded; *2* — press-down roller; *3* — connecting tape from laminated fabric; *4* — backing tape from laminated fabric; *5* — PVC melt that forms during welding; *6* — PVC flash from welded joint sides

Geometrical parameters of the melt bead are informative values, which make it easy to evaluate the nature of running of thermal processes in the welding zone and adjusting them, if required. At sufficient lighting of the space under the roller, it is possible to visually observe the parameters of the melt bead. Presence of the bead indicates that melting of the laminated fabric PVC coating occurred, bead diameter is proportional to the heating level and amount of molten PVC coating and bead absence in some weld zone is an indication of formation of a lack-of-penetration.

Adjustment of thermal processes in the welding zone can be achieved by changing the heated air temperature, welding speed or changing the heater nozzle orientation. Change of the heated air temperature is a rather sluggish process that lasts tens of seconds. Therefore, air temperature is set before welding and it remains unchanged furtheron. Figure 10 shows the schemes of typical violations that arise in hot air welding of laminated fabric.

In the absence or fragmentary appearance of a melt bead of a small diameter under the roller (Figure 10, *a*, *b*), the temperature in the welding zone is below the required one. Welding speed should be smoothly
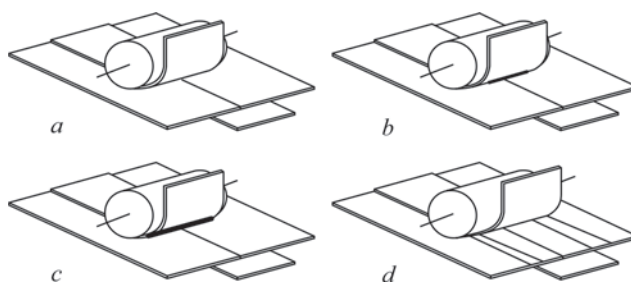


**Figure 10.** Scheme of possible violations of the optimal process of hot air welding of artificial leather (for description see the text)

decreased up to appearance of a uniform bead of the melt over the entire weld width.

At formation of a large diameter bead under the roller and pressing out of part of the melt from under the tape (Figure 10, *a*) the welding zone is overheated, and a too large amount of PVC melt forms. The welding speed should be smoothly lowered, while monitoring the dimensions of the melt bead without allowing it to disappear or lack-of-penetration to form.

Absence of the melt bead from one of the roller sides is indicative of nonuniformity of the welding zone heating by the weld width. In this case, it is necessary to move the heater by a screw mechanism so that the nozzle shifted towards the unheated region. During welding, shifting of the connecting tape from the weld axis to the side (Figure 10, *d*) can occur. It usually points to an incorrect orientation of the axis of roller rotation and its deviation in the horizontal or vertical planes, and the press-down roller position should be adjusted.

It is convenient to perform correction of the mode of heating the fabrics being welded by changing the welding speed, and by adjustment of the electric parameters of the welding unit drive.

An experimental set up was manufactured, in which a carriage with an electromechanical drive is used to move the air heater with the press-down roller along the butt of the fabrics, in order to perform butt welding of laminated fabrics, connected by a tape on both sides. An experimental study of the process of butt heat sealing of laminated PVC fabrics by an outer tape, using heated air, was performed. Optimum parameters of the welding process and visual criteria of sound formation of a laminated fabric joint were determined, and principles of manual real-time adjustment of the process of heat sealing by hot air were developed.

1. *Properties of polyvinylchloride. Polymer materials* [in Russian]. http://www.polymerbranch. com/catalogp/view
2. *Membrana — internet magazine of laminated tissues* [in Russian]. https://www.tentmarket.com.ua/
3. Zajtsev, K.I., Matsyuk, L.N., Bogdashevsky, A.V. et al. (1988) *Welding of polymer materials*: Refer. Book. Ed. by K.I. Zajtsev, L.N. Matsyuk. Moscow, Mashinostroenie [in Russian].
4. *Manual welding machine Leister triac S. LEISTER.* http://leister-club.ru/